EPSC2017

OPS1 abstracts

EPSC Abstracts
Vol. 11, EPSC2017-22, 2017
European Planetary Science Congress 2017

Nitrogen isotope ratio and its evolution on Titan

Vladimir A. Krasnopolsky
Moscow Institute of Physics and Technology, Moscow, Russia (vlad.krasn@verizon.net)

Please make sure that your pdf conversion results in a document with a page size of 237 x 180 mm!

Abstract

$^{14}N/^{15}N$ ratios in the Sun, Jupiter, comets, and the inner planets indicate that Earth, Venus, and Mars got their nitrogen as N_2 gas and NH_3 ice in proportion 3 : 1. An alternative explanation is that planetesimals were another reservoir of N with $^{14}N/^{15}N = 270$.
$^{14}N/^{15}N = 168$ in N_2 and 60 in HCN on Titan, and the great difference is explained by strong enrichment in ^{15}N by a factor of 8 in predissociation of N_2 at 80-100 nm (Liang et al. 2007) and no fractionation in other 12 processes that form N. The calculated $^{14}N/^{15}N = 57$ in nitriles, in perfect agreement with the observations.
Modeling of nitrogen isotope fractionation by formation of nitriles and sputtering through the history of Titan with the much greater solar EUV and wind in the earlier epochs supports ammonia similar to that in comets as a source of nitrogen on Titan.

1. $^{14}N/^{15}N$ in the Solar System

It was thought 20 years ago that $^{14}N/^{15}N \approx 270$ everywhere in the Solar System, and the smaller value of 170 in the martian atmosphere is caused by preferential escape of the light isotope. The greater ratio in Jupiter measured by the Galileo probe and in the Sun, as well as the recent observations in comets (Rousselot et al. 2014), change the problem (Table 1).

Table 1. $^{14}N/^{15}N$ in the Solar System

Solar wind, Jupiter	$^{14}N/^{15}N =$ 440
Earth, Venus, Mars (mantle), chondrites	270
Mars (atmosphere)	170
Comets (NH_3)	130

It is believed that the protosolar nebula had nitrogen as N_2 with $^{14}N/^{15}N = 440$ and ammonia ice with $^{14}N/^{15}N = 130$. Accretion of the Sun and Jupiter began before the accretion of the inner planets and captured most of N_2. Therefore the inner planets got N as a mixture of N_2 and NH_3 in proportion 3 : 1. An alternative explanation is that planetesimals were another reservoir of nitrogen with $^{14}N/^{15}N = 270$.

2. $^{14}N/^{15}N$ on Titan

Table 2. Observed $^{14}N/^{15}N$ in Titan's atmosphere

Species	Ratio	Instrument
N_2	167.6 ± 0.6	Huygens/GCMS
HCN	60-70	IRAM
	94 ± 13	SMA
	72 ± 9	SMA
	56 ± 8	Cassini/CIRS
	≈ 60	mean

Why are $^{14}N/^{15}N$ so different in N_2 and HCN on Titan? Isotopic shift in predissociation of N_2 at 80-100 nm puts the lines of $^{14}N^{15}N$ in windows between the N_2 lines. Therefore ^{15}N is enriched in predissociation by a factor of 8 (Liang et al. 2007). HCN is produced by

$N + CH_3 \rightarrow H_2CN + H$

$H_2CN + H \rightarrow HCN + H.$

N, $N(^2D)$, N^+, and N_2^+ are formed in dissociation, ionization, and dissociative ionization by the EUV photons, photoelectrons, magnetospheric electrons and protons, and cosmic rays (Table 3).

Table 3. Column production rates of N, N^*, and N^+

#	Reaction	Column Rate (cm^{-2} s^{-1})
1	$N_2 + h\nu$ (80-100 nm) → $N + N^*$	9.01+7
2	$N_2 + h\nu$ (λ<51 nm) → $N^+ + N^* + e$	5.49+7
3	N_2 + e (phot) → $N + N^* + e$	1.10+8
4	N_2 + cosmic rays → $N + N^*$	3.43+7
5	→ $N^+ + N^* + e$	1.03+7
6	N_2 + e (magn) → $N + N^* + e$	2.03+6
7	→ $N^+ + N^* + e + e$	4.11+5
8	N_2 + protons → $N + N^+$	1.23+7
9	→ $N^+ + N^* + e$	2.48+6
10	$N_2^+ + e \rightarrow N + N^*$	1.18+6
11	$N_2H^+ + e \rightarrow N + NH$	2.04+6
12	$N_2^+ + C_2H_4 \rightarrow HCN^+ + HCN + H_2$	5.59+5
13	→ $HCNH^+ + HCN + H$	5.59+5
14	Total	3.21+8

All these processes have been calculated in the photochemical model by Krasnopolsky (2009, 2014). N_2^+ mostly returns N_2 in

$N_2^+ + CH_4 \rightarrow N_2 + CH_3^+ + H$.

The model involves three reactions of N_2^+ that form either N or HCN. Predissociation with fractionation factor of 8 is responsible for 28% of total production of N, and the remaining 72% is expected without significant fractionation. Therefore

$$\frac{HC^{14}N}{HC^{15}N} = \frac{1}{\frac{0.28*8}{168} + \frac{0.72}{168}} = 57 ,$$

in excellent agreement with the observations.

3. Evolution of nitrogen on Titan

Table 4. Irreversible loss of N from Titan atmosphere

Process	Species	Loss of N
Condensation	HCN	107 g cm^{-2} Byr^{-1}
	HC_3N	46
	CH_3CN	6.0
	C_2N_2	1.9
Polymerization	C_XH_YN	231
Total		392

The C≡N triple bonds are strong and cannot be broken in Titan's atmosphere, and nitriles are irreversibly lost (Table 4). The N-H bonds are much weaker and comparable to the C-H bonds, and eleven species with N-H bonds return their nitrogen in the model. Total photochemical loss of N is 392 g cm^{-2} Byr^{-1} with fractionation factor of 168/60 = 2.8 (Table 2). Loss of nitrogen by sputtering, nonthermal and ion escape is ≈60 g cm^{-2} Byr^{-1} (Haye et al. 2007) with fractionation factor of 0.73 (Mandt et al. 2014).

The current abundance of N_2 in Titan's atmosphere is 1.1×10^4 g cm^{-2}, and its lifetime is 25 Byr. However, the young Sun was much brighter in the EUV and had stronger wind (by factors of 6 and 20, respectively, at 1 Byr, Fig. 1). We assume that the EUV is responsible for the deposition of nitriles and the solar wind for the escape. Reactions of the atmosphere to the variable EUV and solar wind are generally unknown, and we adopt two options with the linear and square root atmospheric responses. Mandt et al. (2014) argued that hydrodynamic escape occurred in the first Byr without isotope fractionation. Then numerical solutions of the balance equations result in initial $^{14}N/^{15}N$ = 108 and 125 for the linear and square root responses, respectively. Thus we conclude that the initial nitrogen isotope ratio on Titan was close to that of ammonia in comets. Ammonia on Titan is photochemically and thermally (in the interior) decomposes into N_2.

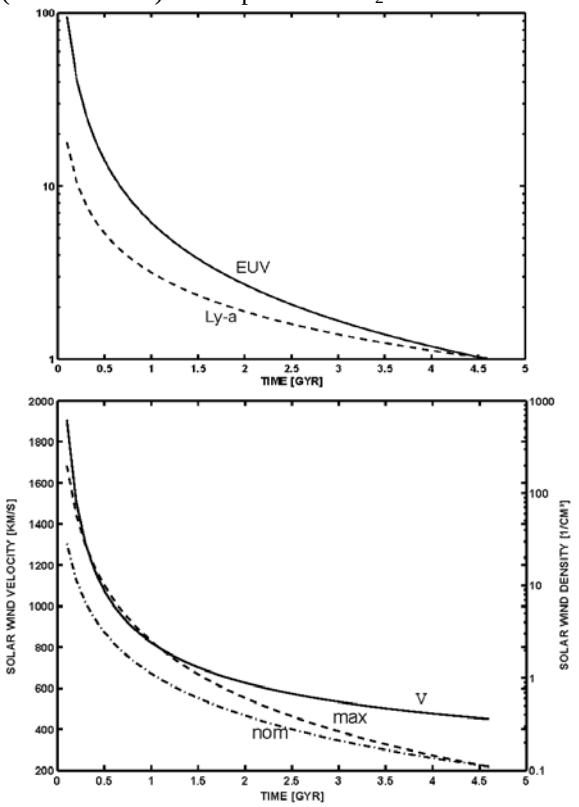

Fig. 1. Evolution of the solar EUV and wind (Penz et al. 2005).

Acknowledgement

This work was supported by Grant 16-12-10559 of the Russian Science Foundation.

References

[1] Haye, V., et al., JGR 112, A07309, 2007.
[2] Krasnopolsky, V.A., Icarus 201, 226-256, 2009.
[3] Krasnopolsky, V.A., Icarus 236, 83-91, 2014.
[4] Liang, M.C., et al., Astrophys. J. Lett. 664, L115-L118, 2007.
[5] Mandt, K.E., et al., Astrophys. J. Lett. 788, L24 (5pp), 2014.
[6] Penz, T., et al., Adv. Space Res. 36, 241-250, 2005.
[7] Rousselot, P., et al., Astrophys. J. Lett. 780, L17 (5pp), 2014.

EPSC Abstracts
Vol. 11, EPSC2017-28-1, 2017
European Planetary Science Congress 2017

An exceptionally high standing ridge on Enceladus

B. Giese (1), P. Helfenstein (2), E. Hauber (1), H. Hussmann (1) and R. Wagner (1)
(1) Institute of Planetary Research, DLR, Berlin, Germany
(2) Cornell Center for Astrophysics and Planetary Science, Ithaca, USA (bernd.giese@dlr.de)

Abstract

Cassini stereo-derived topography reveals an exceptionally high-standing saw-tooth-shaped ridge in Enceladus' Samarkand Sulcus. Over a length of 100 *km* and of a width of 10 *km*, it reaches elevations of up to 1750 *m*, which is the highest ridge observed on Enceladus so far. Flanking slopes reach 40°. The morphology of the ridge suggests that it formed first by rift flank-uplift caused by extension, but sinistral shear and compression later modified the shape. This modification has in particular emplaced small-scale fragments sticking out of the surface and creating a (previously enigmatic) pattern of black spots on the sun facing side of the ridge. Modelling of uplift related lithospheric flexure yields an effective elastic thickness (T_e) of 0.36 *km* (E=1GPa) at the time of formation, similar to results obtained in Harran Sulcus [1]. Considering the ridge as a load on the lithosphere at present-day, we obtain a lower limit on T_e of 1.5 *km*. Within an asteroid/comet based impact chronology the ridge is 3.6/0.7 Gy old.

1. Introduction

During Cassini's 228th orbit around Saturn the onboard camera imaged, once again, a prominent ridge in Enceladus' Samarkand Sulcus (Fig. 1). This happened because images taken during orbit 3 showed an enigmatic pattern of dark spots on the sun-facing side of the ridge. The new set of images is of higher resolution and, in addition, includes stereo coverage of the surface that provides new 3D information. With that we were able to study the morphology of the ridge in great detail, in particular to ascertain the nature of the dark spots. Moreover, the new observations shed more light on the complex geologic history of Enceladus. Previous papers [2], [3] have concluded that a combination of contraction, extension, and shearing has shaped the ridge, but without being specific. The new data allow narrowing down the formational scenario. Using a stereo-derived topographic model we could also infer information on the state of the lithosphere.

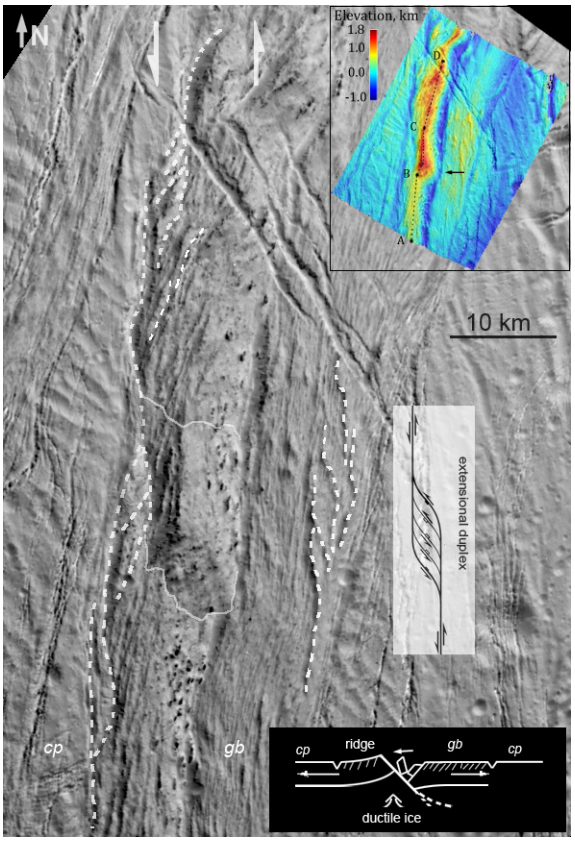

Figure 1: Cut out of Cassini frame N1829240977 (90 *m/pxl*) showing the ridge (centred at 0°, 23°E) and a sketch map of faults (dashed lines) and structural boundaries (thin full lines) identified on the basis of an anaglyph image (not given here). Solar azimuth is 30°. (Top inset) Color-coded Digital Elevation Model (*DEM*) derived from N1829240977 and N1829241569 (60 *m/pxl*) using methods of photogrammetry [1]. *DEM* horizontal resolution is 0.5-1 *km*, vertical accuracy is 30 *m*. (Bottom inset) Cartoon showing how the ridge initially formed. *cp* denotes "cratered plains", and *gb* denotes "grooved band".

2. Observations

(1) The ridge consists of a lower end (Fig. 1, *A*→*B*) and an upper end (*B*→*D*), which stands 600-700 *m* higher on average. There is a distinct boundary between them (Fig. 1, southern full line; Fig. 2, p1).

In addition, the upper end features a second structural boundary (Fig. 1, northern full line) which marks a change in elevation and slope across the ridge (Fig. 2, p5→p6). The highest point of the ridge is 1750 *m* above the surroundings. **(2)** On its eastern side, the ridge is bounded by a pronounced V-shaped trough (Fig. 1, *DEM*). The trough runs roughly straight from south to north and is equally pronounced all the way up. A clear exception is the transition zone between the two ends, where the trough has a narrowing (Fig. 1, black arrow). On its western side, the ridge is bounded by faults with sigmoidal to en echelon patterns (Fig. 1, dashed lines). Compared with the eastern trough, these faults are topographically less pronounced. **(3)** The cross section of the ridge is mostly saw tooth-shaped (Fig. 2, p5-p8) with p5 showing clear indication of flexure of the lithosphere. However, taking p5 as a starting point, there is a growing degree of deformation of the western flank associated with uplifting (p5→p7) and the formation of ramp-like features (p5→p2). Ramps appear to form in relation to the sigmoidal faults (note: p5 lacks a ramp as the bounding fault is shallow there). Ramps can also be observed at the lower end of the ridge (p9, p10). **(4)** While the west facing slope of the ridge is textured as the grooved band to the east (Fig. 1), the east facing slope is not but exhibits a pattern of dark spots. An anaglyph image reveals that most spots are not albedo features but associated with small-scale fragments sticking out of the surface and casting shadows. Consistent with that: image-brightness profiles across different spots show the same constant brightness value in the core of the shadow. **(5)** The grooved band east of the ridge exhibits a fault pattern which is consistent with an extensional duplex at sinistral shear motion (Fig. 1).

3. Discussion and Conclusions

With an elevation of 1750 *m* this ridge is higher than any other ridge observed on Enceladus so far. The ridge summit observed in Harran Sulcus is 1200 *m* (Fig. 2), and the prominent branching dorsa ridges on the trailing hemisphere of Enceladus [3] reach only 900 *m* (result from photoclinometry).

Our observations are consistent with the following formational scenario: The region occupied by the ridge today was initially part of the grooved band (see Fig. 1), which formed by extension. In a late stage of band formation (or soon thereafter), strain focused in the center of the band and created a deep fault and finally a trough. In contrast to the fine-scale faults of the grooved band, this fault has penetrated the lithosphere and thus allowed ductile ice at depth to rise isostatically to the surface. This has flexed the lithosphere and created the saw-tooth shape of the ridge. Subsequently, left lateral shear motion in concert with compression has modified the shape of the ridge, which includes the formation of exceptionally high terrain portions, narrowings, and small-scale fragments sticking out of the surface (dark spots).

Crater size frequency counts yield an age of 3.6/0.7 Gy (asteroid/comet based impact chronology).

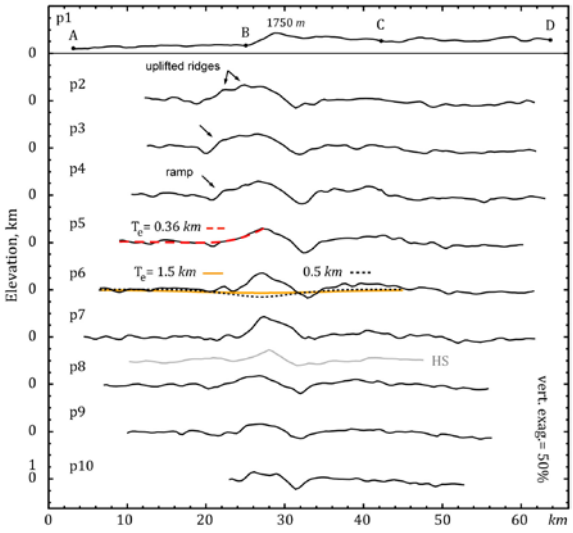

Figure 2: Profiles derived from the *DEM*. p1: along-ridge profile (comp. Fig. 1, top inset). p2-p10: across-ridge, about evenly spaced, profiles with p5 running through point *C* of p1, and p7 including the point of highest elevation. At that point the slope reaches 40°. The grey line is a mean profile across a morphologically similar ridge observed in Harran Sulcus [1]. p5, red dashed line: flexural model profile derived from a bottom loading model [1]. T_e denotes the effective elastic thickness of the lithosphere. p6, orange and dotted line: flexural model profiles derived from a top loading model. Downward flexure with amplitudes >200 *m* would clearly be visible in the data but is not observed (inspect p5, p6, p7). At the given load applied by the ridge this requires $T_e \geq 1.5$ *km*.

References

[1] Giese, B. et al.: Enceladus: An estimate of heat flux and lithospheric thickness from flexurally supported topography, GRL, Vol. 35, L24204, 2008.

[2] Spencer, F. et al.: Enceladus: An Active Cryovolcanic Satellite, in *Saturn from Cassini-Huygens*, Springer Netherlands, 683-724, 2009.

[3] Crow-Willard, E. N., and R. T. Pappalardo: Structural mapping of Enceladus and implications for formation of tectonized regions, JGR, Planets, 120, 928–950, 2015.

EPSC Abstracts
Vol. 11, EPSC2017-32, 2017
European Planetary Science Congress 2017

Orbitally and geographically caused seasonal asymmetry in Titan's tropospheric climate

T. Tokano
Institut für Geophysik und Meteorologie, Universität zu Köln, Germany (tokano@geo.uni-koeln.de)

Abstract

This work addresses the question as to how orbital parameter variations and geography cause a seasonal asymmetry in Titan's tropospheric climate. A series of time-slice experiments for the last 45 kyr is carried out with a Titan general circulation model with two different geography patterns. If the geography is assumed to be globally uniform or symmetric about the equator, the seasonal asymmetry in the climate nearly reverses within one precession cycle. If instead the observed asymmetric geography pattern is taken into account, it can partly overcompensate the seasonal asymmetry that orbital eccentricity would cause.

1. Introduction

Observations of Titan's landscape by Cassini provided the first hint that orbitally forced climate variations may exist on Titan as on other planets. The global distribution of hydrocarbon seas/lakes is highly skewed toward the north polar region, which was tentatively interpreted as possible evidence of a pole-to-pole migration of methane between the poles induced by Saturn's apsidal precession [1]. Previous simulations with general circulation models (GCMs) have shown that the present orbital configuration with perihelion in southern summer gives rise to a gradual accumulation of surface liquid methane deposits in the north polar region at the expense of the south polar region, possibly consistent with the hypothesis of Ref. 1 [4-6]. However, seasonal asymmetries in the climate can also arise from a hemispheric dichotomy of geography as on Earth or Mars [7]. Furthermore, the cause of the observed sea distribution is controversially discussed among Titan geologists [2, 3]. The present study aims at investigating to which extent orbital parameter variations change Titan's tropospheric climate and how this is affected by the geography, with emphasis on the seasonal asymmetry in the tropospheric climate.

2. Methods

An updated version of the Cologne Titan GCM with methane hydrology [8] is used to perform ten time-slice experiments for epochs covering the last 45 kyr. The ten simulations differ from each other only in the orbital parameters. In the first series of simulations the geography (topography, albedo, emissivity, thermal inertia and methane moisture availability) is intentionally kept symmetric about the equator or globally uniform. Thereafter, the simulations are repeated with a model version in which a more realistic geography pattern constrained by Cassini observations is implemented.

3. Results

The paper discusses seasonal and spatial variations in surface temperature, surface wind, mean meridional circulation, methane climate (humidity, precipitation), nitrogen condensation etc. in ten epochs. One focus of the study is the dependence of the magnitude and sign of the hemispheric asymmetry in the climate on orbital parameters and inhomogeneous geography. In all epochs the mean meridional circulation undergoes a semi-annual reversal, but the asymmetry between the summer circulation and the opposite winter circulation increases with increasing eccentricity. The north-south asymmetry in the surface temperature near solstice is also larger in epochs with the large eccentricity. Methane precipitation is highly sensitive to both orbital parameters and geography. In the absence of geography, the latitudinal distribution of annual precipitation nearly reverses within one precession cycle. However, an asymmetric geography pattern can partly overcompensate the seasonal asymmetry that orbital eccentricity would cause.

Acknowledgements

The work of the author was supported by DFG Grant TO269/4-1.

References

[1] Aharonson, O., et al.: An asymmetric distribution of lakes on Titan as a posible consequence of orbital forcing, Nat. Geosci., Vol. 2, pp. 851-854, 2009.

[2] Moore, J. M., Howard, A. D., and Morgan, A. M.: The landscape of Titan as witness to its climate evolution, J. Geophys. Res., Vol. 119, doi:10.1002/2014JE004608, 2014.

[3] MacKenzie, S. M., et al.: Evidence of Titan's climate history from evaporite distribution, Icarus, Vol. 243, pp. 191-207, 2014

[4] Schneider, T., et al.: Polar methane accumulation and rainstorms on Titan from simulations of the methane cycle, Nature, Vol. 481, pp. 58-61, 2012.

[5] Lora, J. M., et al.: Simulations of Titan's paleoclimate, Icarus, Vol. 243, 264-273, 2014.

[6] Newman, C. E., et al.: Simulating Titan's methane cycle with the TitanWRF general circulation model, Icarus, Vol. 267, pp. 106-134, 2016.

[7] Richardson, M. I., and Wilson, R. J.: A topographically forced asymmetry in the Martian circulation and climate, Nature, Vol. 416, pp. 298-301,2002.

[8] Tokano, T., et al.: Three-dimensional modeling of the tropospheric methane cycle on Titan, Icarus, Vol. 153, pp. 130-147, 2001.

EPSC Abstracts
Vol. 11, EPSC2017-36, 2017
European Planetary Science Congress 2017

Modulated features of Jupiter, Saturn, Pluto and enigmatic X-ray emission of Pluto

G. Kochemasov
IGEM of Russian Academy of Sciences, 35 Staromonetny, 119017 Moscow, RF (kochem.36@mail.ru)

"Orbits make structures". As all cosmic bodies in Universe rotate and move in several orbits with very different orbiting frequencies they are affected by modulated waves. They appear as predicted by the radio wave physics. The modulation is division and multiplication of the higher frequency by the lower one. As a result along with main frequencies appear two side frequencies with corresponding them tectonic granules. The wave born tectonic granules normally are evenly sized, shoulder-to-shoulder disposed in lines, crossing lines, grids and lattices. Examples are below (Fig. 1-3).

Very effective "leopard skin" structure of the saturnian atmosphere with regularly spaced storms about 400 km across (Fig. 1) can be calculated by the modulation of rapidly rotating atmosphere (1/0.45 days, 60000 km radius) by slowly orbiting Saturn around Sun (1/30 years). To modulated side frequencies correspond smaller granules (1/3421 x 7.5)3.14 x 60000 = 7.3 km and larger granules (1/3421 : 7.5)3.14 x 60000 = 413.5 km. The smaller granules are not yet observed (maybe they show themselves in kilometric radio emissions), but the larger granules are ubiquitous on he Saturn's surface as the "leopard skin" spots. Waiting for Juno detailed images we analyze the famous Voyager image with the Red Spot (Fig.2). This image reveals various wave forms and penetrating them weak and fine tissue made of granules ~200 to 400 km across. This size is explained by modulation by 1/12 y. fr. of 1/10 h. fr. giving modulated size ~191 km.

Pluto' rotation and orbiting with frequency 1/6.39 days around the barycenter of the Pluto-Charon system gives granule size 16.3 km (πR/228) according to the relation between orbiting frequencies and tectonic granules sizes (Kochemasov, 1986- 2016). These granules as polygons about 20 km across are visible especially on the brightest and highest sector of Sputnik Planum (Fig. 3-"lake" ~30 krn across peppered with fine granules ~0.25 km). Another widespread granule size is about 0.25 km (Fig. 3). It is calculated by modulation of fr. 1/6.39days by orbital fr. 1/248 years=1/90465 days to obtain side frequency 1/14157 and corresponding to it granule size 0.263 km.

The first detection of Pluto in X-rays has been made using NASA' Chandra X-ray Observatory. Chandra obtained data during four separate observations. During each observation Chandra detected low energy X-rays from the planet (Fig. 4). X-rays from Pluto are somewhat surprising result given that Pluto –a cold, ice-rocky world without a magnetic field - has no natural mechanism for emitting X-rays. However, it is known that comets can create X-rays by the interaction between their gases and the solar wind. The immediate mystery is that Chandra's readings on the brightness of the X-rays are much higher than expected from the solar wind interacting with Pluto's atmosphere. Some inadequate explanations were proposed. But modulation of orbiting frequencies of Pluto was not considered. In the solar system it is 1/248y., in Galaxy it is approx. 1/200000000y. Division of the first by the second gives 1/806452 y. To this fr. corresponds wave long ~10^{-8} M (proportion with 16.3 km corresponding to the rotation fr. 1/6.39 d. [], 2] or soft X-rays.

References

[1] Kochemasov G.G.. Wave modulation in planetology: a new way of planetary thinking // The seventh Moscow Solar System symposium, 10-14 October 2016, Space Research Institute (IKI), Moscow, Abstracts, 7MS3-PS-67, p. 283-284.
[2] Kochemasov G.G. Gamma-ray emission in the Universe – a possible explanation by the wave modulation // The eighth Huntsville gamma-ray burst symposium, 2016, Abstract #4107.

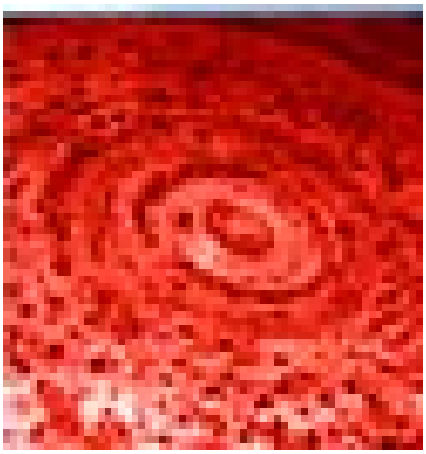

1

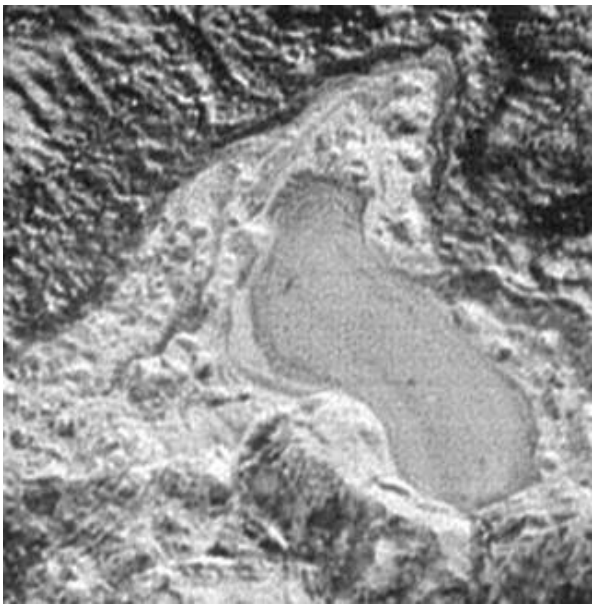

3

2

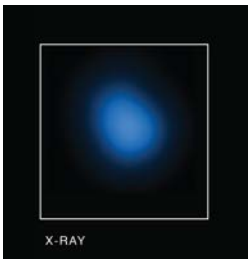

4

Fig. 1. Saturn, PIA08333-“Leopard skin spots”. **Fig. 2.** Jupiter_from_Voyager_1. Fine granulation of “Red spot”, “Pearl”, Plain area SW of “Red spot”. **Fig. 3,** Pluto, “Lake” ~ 30 km across covered by fine granules. **Fig. 4.** Pluto_Main-Chandra1, X-ray

EPSC Abstracts
Vol. 11, EPSC2017-39-3, 2017
European Planetary Science Congress 2017

The spectral nature of various Titan surface units: implications on the composition

A. Solomonidou[1,2,*], A. Coustenis[2], R.M.C. Lopes[1], M. Malaska[1], S. Rodriguez[3], P. Drossart[2], C. Elachi[1], M. Janssen[1], M. Hirtzig[4], B. Schmitt[5], S. Philippe[5], S. Wall[1], K. Lawrence[1], N. Altobelli[10], J. Radebaugh[11], K. Stephan[7], R.H. Brown[8], A. Le Gall[9], E.V. Villanueva[1], A.A. Bloom[1], O. Witasse[12], C. Matsoukas[6], A. Schoenfeld[13]

[1]Jet Propulsion Laboratory, California Institute of Technology, California, USA. [2]LESIA - Observatoire de Paris, PSL Research University, CNRS, UPMC Univ. Paris 06, Univ. Paris-Diderot, 92190 Meudon, France. [3]Laboratoire AIM, Université Paris Diderot, Paris 7/CNRS/CEA-Saclay, DSM/IRFU/SAp, Gif sur Yvette, France. [4]Fondation "La main à la pâte", Montrouge, France. [5]Institut de Planétologie et d'Astrophysique de Grenoble, Grenoble, France, [6]KTH-Royal Institute of Technology, Stockholm, Sweden. [7]Institute of Planetary Research, DLR, Berlin, Germany. [8]Lunar and Planetary Laboratory, University of Arizona, Tucson, United States. [9]Laboratoire Atmosphères, Milieux, Observations Spatiales (LATMOS-UVSQ), Paris, France. [10] European Space Agency (ESA), European Space Astronomy Centre (ESAC), Villanueva de la Canada, Madrid, Spain.[11]Department of Geological Sciences, Brigham Young University, Utah, USA. [12]European Space Agency (ESA), European Space Research and Technology Centre (ESTEC), Noordwijk, Netherlands.[13]Department of Earth, Planetary, and Space Sciences, University of Calilfornia, Los Angeles, California, USA

Abstract

We investigate both the surface and the atmospheric contributions on Titan from Visual and Infrared Mapping Spectrometer (VIMS) spectro-imaging of near-infrared data by use of a radiative transfer code [1-3]. We focus here on the major geological and albedo major units identified in [4-7]: mountains, plains, labyrinths, maculae, impact craters, dune fields, alluvial fans, and possible cryovolcanic and/or evaporite features. We find that, for some of the regions classified as the same geomorphological unit in SAR, there are significant differences in spectral responses (albedo) from VIMS, depending on location. Conversely, some regions classified from SAR as different geomorphological units show very similar spectral responses in VIMS. The surface albedo differences and similarities among the various units constrain the implications for the geological processes that govern Titan's surface (i.e. aeolian, fluvial, sedimentary, lacustrine etc). Hence, we are able to report on the differences and similarities among the various regions, monitor their temporal evolution, and provide implications for their chemical composition, which lead us to constrain specific processes of origin.

1. Context/Data

In order to unveil Titan's surface nature, it is important to determine the surface composition of different units, along with their morphological expressions. Matching the surface units with specified mixtures of materials can shed light on the interconnection between the interior, surface, and atmosphere. The Cassini VIMS obtained spectro-imaging data of Titan's surface from flybys performed during the last thirteen years, in the 0.8-5.2μm range. The data from the seven narrow methane spectral "windows" centered at 0.93, 1.08, 1.27, 1.59, 2.03, 2.69-2.79 and 5 μm provide some information on the lower atmosphere and the surface parameters. Atmospheric scattering and absorption need to be clearly evaluated before we can extract the surface properties. Here we focus on areas that are in the mid-latitudes and are of geological interest. The geomorphological units and albedo features we analyze are:
i. the undifferentiated plains [5;6],
ii. hummocky/mountainous terrains [4;6],
iii. labyrinth terrains [6],
iv. variable plains [5;6], v. streak-like plains [6],
vi. dunes [4;5],
vii. candidate evaporites [8],
viii. the Huygens Landing site [6],
ix. candidate cryovolcanic sites [3;4],
x. alluvial fans [7], xi. maculae [10],
and xii. impact craters [9]. For most of the geomorphological units and albedo features, we also provide results on the temporal evolution of these surface units for a significant period of time between 2004-2013 [3;11].

2. Methods

Our radiative transfer (RT) method is a 1-D multi-stream RT code based on the open-source solver SHDOMPP [1]. As inputs, we used most of the Huygens Atmospheric Structure Instrument (HASI) and the Descent Imager/Spectral Radiometer (DISR) measurements, as well as new methane absorption coefficients. These are important to evaluate the atmospheric contribution and constrain the real surface alterations by comparing the spectra of these

regions. Figure 1 shows the spectral variations of the extracted surface albedos from RT of the regions of interest with the 'ground truth' albedo derived at the Huygens landing site (HLS). We then test the surface albedos against a spectral database of Titan candidate ice and organic constituents and provide some constraints on the possible major material present in every geomorphological unit. We use a new updated material library based on Bernard et al. (2006), Coll et al. (2006) and the GhoSST database (http://ghosst.osug.fr).

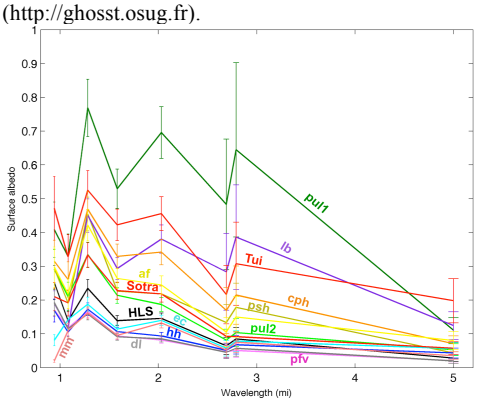

Fig. 1. Weighted averages in the methane windows of the surface albedos of the various geomorphological units: *i)* Undifferentiated plains 1 (pul 1) (green), *ii)* Undifferentiated plains 2 (pul 2) (light green), *iii)* Labyrinth (lb) (violet), *iv)* Streak-like plains (psh) (dark yellow), *v)* Variable plains (pfv) (fuchsia), *vi)* Hummocky (hh) (blue), *vii)* Dunes (dl) (grey), *viii)* Evaporite candidates (ec) (light-blue), *ix)* Tui Regio –cryovolcanic (cc Tui) (red), *x)*,Sotra Patera –cryovolcanic (cc Sotra) (red), *xi)* impact craters (cph) (orange), *xii)* alluvial fans *(af)* (yellow), *xiii)* maculae (mm) (peach), and *xiv)* the Huygens landing site (HLS). For clarity purposes, we have connected the points with straight lines that do not represent real results but help see the spectral behavior as a whole for each unit.

3. Results

From the results of the analysis, we confirm that for the majority of terrains there is a good correlation between the classifications from SAR and VIMS data. Within VIMS data, we have identified 3 main types of albedo response (high, medium, low). The Huygens landing site and the candidate evaporite regions appear to be compositionally similar to one type of plains unit (variable plains), suggesting similar formation mechanisms. By matching the extracted albedos with reflectance spectra of candidate materials for Titan's surface, we find that all regions fall into one of three main types of major candidate constituent: water ice, tholin-like material, or an unknown, very dark material.

From the analysis of the temporal variation Tui Regio (cryovolcanic candidate), which has been initially reported to change in surface albedo from 2005 to 2009 by becoming darker [5], has returned to its initial (2005) brightness in 2015. Furthermore, Hotei Regio, which remained unchanged during 2005 to 2009, retained the same brightness up to 2015. In a previous study [5], we have shown that Sotra Patera (strongest cryovolcanic candidate) became brighter within a year from 2005 to 2006 by a factor of 2, especially at short wavelengths. We therefore show that temporal variations of surface albedo (in chemical composition and/or morphology) exist for some areas on Titan's surface, but that they differ from one region to the other. This could be due to diverse, past and/or ongoing formation processes (endogenic and/or exogenic, possibly cryovolcanic). The surface albedo variations together with the presence of volcanic-like morphological features suggests that the cryovolcanic candidate features are possibly connected to the satellite's deep interior, which could have important implications for the satellite's astrobiological potential. This idea has been recently augmented by the construction of recent interior structure models of Titan and corresponding calculations of the spatial pattern of maximum tidal stresses [14]. However, an explanation attributed to exogenic processes is also possible [15]. Currently, we are working on deriving information on the full chemical compositions of the aforementioned regions from the extracted surface albedos. This will shed light on the potential formation processes.

Acknowledgements

This research was supported by the Cassini Data Analysis and Participating Scientists Program (CDAPS) grant #NH16ZDA001N to RL. This work was conducted at JPL/Caltech under contract with NASA.

References

[1]Hirtzig et al.: Icarus, 226, 470-486, 2013. [2]Solomonidou et al.: JGR 119, 1729-1747, 2014. [3]Solomonidou et al.: Icarus, 270, 85-99, 2016. [4]Lopes et al.: Icarus, 205, 540-558, 2010. [5]Lopes et al.: Icarus, 270, 162-182, 2016. [6]Malaska et al.: Icarus, Icarus, 270, 130-161, 2016. [7]Radebaugh et al.: Geological Society London Special Publications, 2016. [8]Barnes et al.: Planetary Science, 2, 1-22, 2013.[9] Neish et al.: GRL, 42, 3746–3754, 2015. [10]Hayne et al.: AGU, #P13A-0166, 2006. [11] olomonidou et al. in prep. [12]Bernard et al.: Icarus, 185, 301–307, 2006. [13]Coll et al.: Adv. Space Res., 27, 289-298, 2001. [14]Sohl et al.: JGR, 119, 1013-1036, 2014. [15]Moore & Pappalardo, Icarus, 212, 790-806, 2011.

EPSC Abstracts
Vol. 11, EPSC2017-52, 2017
European Planetary Science Congress 2017

How Planet Nine could change the fate of the Solar system

Dimitri Veras
Department of Physics, University of Warwick, Coventry CV4 7AL, UK
(d.veras@warwick.ac.uk)
Based on MNRAS (2016), 463, 2958-2971

Abstract

The potential existence of a distant planet ('Planet Nine') in the Solar system has prompted a re-think about the evolution of planetary systems. As the Sun transitions from a main-sequence star into a white dwarf, Jupiter, Saturn, Uranus and Neptune are currently assumed to survive in expanded but otherwise unchanged orbits. However, a sufficiently distant and sufficiently massive extra planet would alter this quiescent end scenario through the combined effects of Solar giant branch mass-loss and Galactic tides. Here I estimate bounds (see also [1]) for the mass and orbit of a distant extra planet that would incite future instability in systems with a Sun-like star and giant planets with masses and orbits equivalent to those of Jupiter, Saturn, Uranus and Neptune. I find that this boundary is diffuse and strongly dependent on each of the distant planet's orbital parameters. Nevertheless, I claim that instability occurs more often than not when the planet is as massive as Jupiter and harbours a semimajor axis exceeding about 300 au, or has a mass of a super-Earth and a semimajor axis exceeding about 3000 au. These results hold for orbital pericentres ranging from 100 to at least 400 au. This instability scenario might represent a common occurrence, as potentially evidenced by the ubiquity of metal pollution in white dwarf atmospheres throughout the Galaxy.

1. Introduction

The Sun will leave the main sequence in about 6.5 Gyr, and undergo drastic changes (Fig. 1). Its radius will increase by a factor of about 230, it will lose almost half of its current mass, and its luminosity will reach a peak value which is about 4000 times its current value. The Sun will become so large that its radius will extend just beyond where the Earth currently sits. These major changes will occur in two phases. The red giant branch phase will last about 800 Myr. In this timespan, the Sun will gradually lose about a quarter of its mass. The second phase, when the Sun becomes an asymptotic giant branch star, is quicker: lasting just 5 Myr. Another quarter of the Sun's mass will be lost during this period. During both phases, the radius of the Sun will extend out to nearly the Earth's distance.

Although the consequences for the inner Solar system will be profound, the outer solar system will escape relatively unscathed (see Fig. 1).

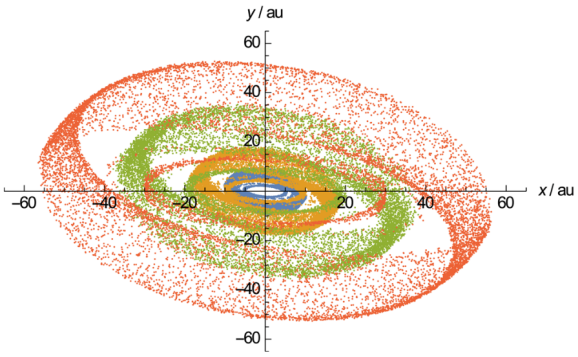

Figure 1: Time evolution of Jupiter, Saturn, Uranus and Neptune as the Sun leaves the main sequence, without the presence of Planet Nine. The semimajor axes approximately double and the eccentricities remain unchanged.

2. Addition of Planet Nine

However, Planet Nine could alter this scenario. If the planet is distant enough, then Galactic tides could perturb the planet inward. If the planet is massive enough, then Planet Nine could scatter off of the four known giant planets.

Figure 2 demonstrates a scenario where Planet Nine is both massive enough and distant enough to change the fate of the Solar system and generate large-scale instability.

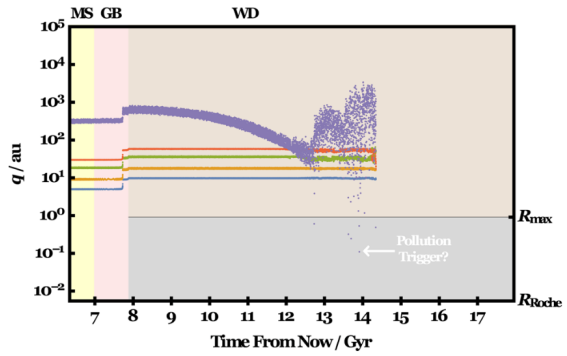

Figure 2: Tidally induced instability: here Planet Nine (with mass of ≈ 109 M⊕) has a large enough initial semimajor axis (≈ 2030 au) for Galactic tides to have a noticeable effect during the white dwarf phase. The tides create an initial increase in the already high value of the initial eccentricity (≈ 0.85), triggering ejection of Neptune as Planet Nine's pericentre approaches the location of the other four planets. Eventually Planet Nine sweeps through any remaining debris in the inner system, which may pollute the eventual white dwarf once inside its disruption radius R_{Roche}.

I performed an ensemble of simulations in order to determine the critical masses and distances that Planet Nine must harbour in order to create instability in the Solar system. The results are in Figure 3.

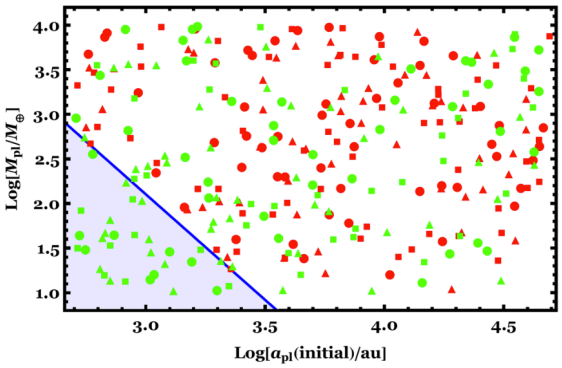

Figure 3: The outcomes from all simulations. Stable simulations are indicated in green symbols, and unstable ones are in red. The different shapes refer to different Solar models. The blue triangle indicates where all simulations remained stable.

3. Conclusions

I demonstrated that a distant planet with an orbital pericentre under 400 au could pose a serious danger to the stability of Solar system analogues during a Sun-like star's giant branch and white dwarf phases. This statement holds true for a distant planet which is at least as massive as Jupiter and harbours a semimajor axis beyond about 300 au, or for a super-Earth when its semimajor axis exceeds about 3000 au. The driver for the instability is a combination of Galactic tides and stellar mass-loss, which together or separately may induce close encounters amongst the five planets, with the distant planet always representing the trigger.

The consequences for other planetary systems are profound. If more distant, trans-Neptunian-like planets are also common, then the ingredients may exist to regularly generate instability and a frequently changing dynamical environment during white dwarf phases of evolution.

Acknowledgements

I have received funding from the European Research Council under the European Union's Seventh Framework Programme (FP/2007-2013)/ERC Grant Agreement no. 320964 (WDTracer).

References

[1] Veras, D.: The fates of Solar system analogues with one additional distant planet, MNRAS, Vol. 463, 2958-2971, 2016.

EPSC Abstracts
Vol. 11, EPSC2017-53, 2017
European Planetary Science Congress 2017

Can Oort clouds pollute their parent stars after they become white dwarfs?

Dimitri Veras (1), Andrew Shannon (2), Boris T. Gänsicke (1)
(1) Department of Physics, University of Warwick, Coventry CV4 7AL, UK
(2) Institute of Astronomy, University of Cambridge, Cambridge CB3 0HA, UK
(d.veras@warwick.ac.uk)
Based on MNRAS (2014), 445, 4175-4185

Abstract

Comets impact the Sun frequently. In fact, coronographs like those which are part of Solar and Heliospheric Observatory (SOHO)/Large Angle and Spectrometric Coronagraph Experiment (LASCO) reveal that a comet grazes the Sun every few days, with a total of about 2400 grazers from 1996 to 2008 [1].

This frequency underscores an outstanding question in the quest to understand planetary systems: what types of small bodies — pebbles, asteroids, comets or moons — are the primary polluter of white dwarfs?

We determine how often remnant exo-Oort clouds, freshly excited from post-main-sequence stellar mass loss, dynamically inject comets inside the white dwarf's Roche radius (also see [2]). We improve upon previous studies by considering a representative range of single white dwarf masses (0.52–1.00 M⊙) and incorporating different cloud architectures, giant branch stellar mass loss, stellar flybys, Galactic tides and a realistic escape ellipsoid in self-consistent numerical simulations that integrate beyond 8 Gyr ages of white dwarf cooling. We find that ~10^{-5} of the material in an exo-Oort cloud is typically amassed onto the white dwarf, and that hydrogen deposits accumulate even as the cloud dissipates. This accumulation may account for the relatively large amount of trace hydrogen, 10^{22} -10^{25} g, that is determined frequently among white dwarfs with cooling ages ≥1 Gyr. Our results also reaffirm the notion that exo-Oort cloud comets are not the primary agents of the metal budgets observed in polluted white dwarf atmospheres.

1. Simulation Details

In order to self-consistently model mass loss, Galactic tidal perturbations and multiple stellar flybys in an *N*-body integrator, we have heavily modified the integrator suite MERCURY (Chambers 1999). The modifications include the following.

(i) We incorporate stellar mass loss into the code by splicing in-between Bulirsch–Stoer time steps, which although is perhaps not necessary for test particle systems like ours here, significantly increases the accuracy for multiple massive objects.

(ii) When the star is not losing mass, the standard non-conservative Bulirsch–Stoer integrator is still used because the perturbation on a comet due to a flyby may be arbitrarily large. When perturbations are large, symplectic integrators may become inaccurate.

(iii) Stellar flybys are modelled as perturbative accelerations to all of the comets and the parent star. A new flyby is introduced when a probability threshold is reached after an individual time step.

(iv) We incorporate into the code a prescription for Galactic tides and assume our modelled systems reside in the solar neighbourhood, specifically at 8 kpc from the Galactic Centre. We include both horizontal and vertical tides, and contributions from an exponential disc, a Hernquist bulge and a cored isothermal halo.

(v) Because pollution likely arises from disrupted bodies forming discs or rings around the star, we

replace the actual white dwarf radius with the white dwarf Roche radius. This change may significantly affect results relating to close encounters with the star.

(vi) We explicitly incorporate the Hill escape ellipsoid into MERCURY for every system sampled to flag ejection, thereby allowing us to quantify escape in preferential directions. This ellipsoid is dependent on both the stellar mass and the Galactic tidal prescription used.

2. Figures

Figures 1-3 illustrate the results of our simulations.

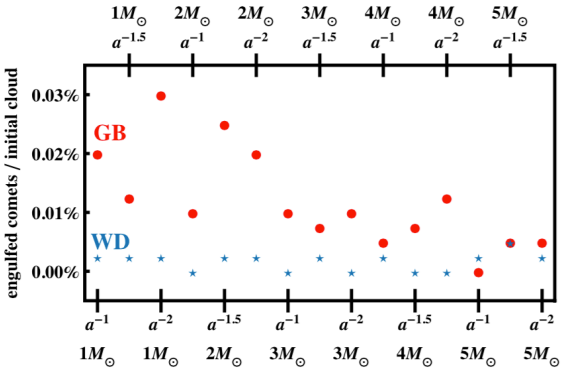

Figure 1: The fraction of comets in exo-Oort clouds which enter the Roche radius of the star when it is a giant branch star (GB; red filled dots) or a white dwarf (WD; blue stars). The results are binned according to the main-sequence stellar mass (and the mass-losing phase). Hence, comets are expect to hit the white dwarf at a rate of about one per 10,000 yr.

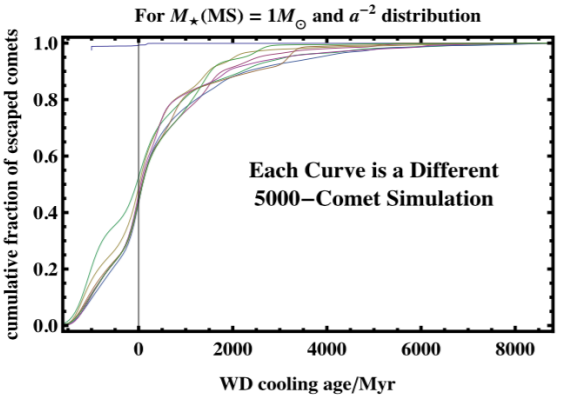

Figure 2: Cloud dissipation: the cumulative distributions of escaped exo-Oort cloud comets as a function of time.

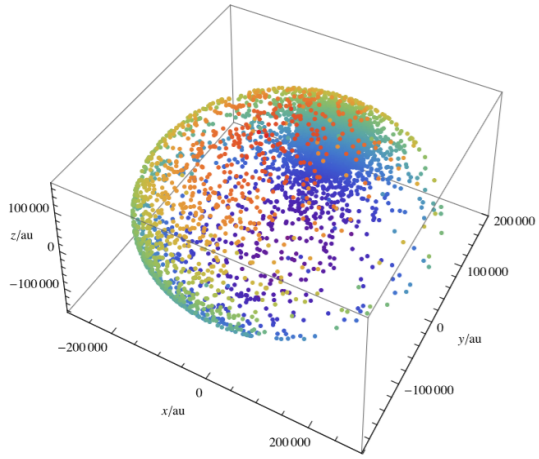

Figure 3: Patchy escape due to an intrusive stellar flyby: the Cartesian (x,y,z) locations where comets escape the Hill ellipsoid for a single 5000-comet 10 Gyr simulation with a stellar progenitor mass of 1 Solar mass.

Acknowledgements

DV and BTG have received funding from the European Research Council under the European Union's Seventh Framework Programme (FP/ 2007-2013)/ERC Grant Agreement no. 320964 (WDTracer). AS has received funding from the European Research Council under the European Union's Seventh Framework Programme (FP/ 2007-2013)/ERC Grant Agreement no. 279973 (DEBRIS).

References

[1] Lamy, P., Faury, G., Llebaria, A., Knight, M.M., A'Hearn, M.F., Battams, K.: Sunskirting comets discovered with the LASCO coronagraphs over the decade 1996-2008, Icarus, Vol. 226, 1350-1398, 2013.

[2] Veras, D., Shannon, A., Gänsicke, B.T.: Hydrogen delivery onto white dwarfs from remnant exo-Oort cloud comets, MNRAS, Vol. 445, 4175-4185, 2014.

EPSC Abstracts
Vol. 11, EPSC2017-73, 2017
European Planetary Science Congress 2017

Titan's Global Geology from Cassini: implications for the geologic history

R. M. C. Lopes[1*], M. J. Malaska[1], A. Solomonidou[1,2],, A. Schoenfeld[1,3] , S.P.D. Birch[4], A.G. Hayes[4], M. A. Janssen[1], A. Le Gall[5], T. Verlander[6], D.A. Williams[7], J. Radebaugh[8], R.L. Kirk[9], E.P. Turtle[10], A. Coustenis[2] and the Cassini RADAR Team

[1]Jet Propulsion Laboratory, California Institute of Technology, Pasadena, California 91109, USA. [2]LESIA - Observatoire de Paris, CNRS, UPMC Univ. Paris 06, Univ. Paris-Diderot, 92190 Meudon, France, [3]Department of Earth, Planetary, and Space Sciences, University of California, Los Angeles, California 90095, USA, [4]Astronomy Department, Cornell University, Ithaca, NY 14853, USA, [5]Laboratoire Atmosphères, Milieux, Observations Spatiales (LATMOS-UVSQ), Paris, France, [6]Northeastern State University, Broken Arrow, OK, USA, [7]School of Earth and Space Exploration, Arizona State University, Tempe, AZ 85281, USA, [8]Department of Geological Sciences, Brigham Young University, Provo, Utah 84602, USA, [9]US Geological Survey, Branch of Astrogeology, Flagstaff, AZ 86001, USA, [10]Johns Hopkins University Applied Physics Laboratory, Laurel, MD 20723, USA.

Abstract

We investigate the geologic history of Titan through mapping and analyzing the distribution of observed geomorphologic features using a combination of Cassini data collected by RADAR, VIMS (Visual and Infrared Mapping Spectrometer), and ISS (Imaging Science Subsystem). Determining the spatial and superposition relations between geomorphologic units on Titan leads to an understanding of the likely time evolution of the landscape and gives insight into the process interactions that drove its geologic history. We have used all available datasets to extend the mapping initially done by Lopes et al. (2010) and Birch et al. (2017) to a global map at 1:800,000 scale in all areas covered by the RADAR Synthetic Aperture Radar (SAR). We show how we are extending the map to regions not covered by SAR, to produce a 1:1,500,000 scale map compatible with USGS standards. We use the map to infer the stratigraphic relations among Titan's different terrain types, which in turn allows us to establish the sequence of geologic processes that have shaped the satellite's surface.

1. Introduction

The Cassini spacecraft has been orbiting Saturn since July 2004. Cassini made 127 close encounters with Titan during these last 13 years, gathering an unprecedented data set collected by 12 instruments. Of particular relevance to geologic studies are the datasets collected by the RADAR, the Visual and Infrared Mapping Spectrometer (VIMS), and the Imaging Science Subsystem (ISS) instruments. The Synthetic Aperture Radar (SAR) mode on the RADAR can to penetrate clouds and organic haze layers to provide high resolution (~350 m spatial resolution at best) views of the surface geology. We used SAR data as the base for mapping, but the RADAR's other modes (altimetry, scatterometry, radiometry) also provide valuable supplementary data for interpreting the geology.

Titan has an icy crust, but water ice signatures are not easily detected due to atmospheric scattering and absorption, hampering observations of complex organic molecules on the surface. The extended, dense, and hazy N_2-CH_4 dominated atmosphere shields the surface from direct optical observations, except at certain frequencies where the methane absorption is weak. These "atmospheric windows" are exploited by VIMS. In particular, VIMS spectro-imaging near-infrared data, after the removal of atmospheric contributions, is capable of providing valuable compositional constraints (Solomonidou et al. 2016; this meeting). Cassini's ISS is equipped with a 0.938 μm narrow band pass filter and infrared polarizing filters that also take advantage of a window in the methane's absorption spectrum. Base maps obtained by ISS were used to obtain overall correlations with the terrain units mapped from SAR. Data from ISS, VIMS, and radiometry were used to extend the mapping in areas not covered by SAR during the mission, using correlations between SAR and these data sets.

2. Methods and Results

Continuing the initial work described in Lopes et al. (2010) and the detailed mapping of the Afekan region by Malaska et al. (2016) and of the polar regions by Birch et al. (2017), we have established the major geomorphologic unit classes on Titan. These broad classes are: hummocky/mountainous terrains, labyrinth terrains, dunes, plains, craters, and

lakes. We have also mapped individual features such as craters, channels nd their deposits, and candidate cryovolcanic features. We have found that the hummocky/mountainous terrains are the oldest units on the surface and appear radiometrically cold, indicating icy materials [7]. The labyrinth terrains consist of highly incised dissected plateaux with medium radar backscatter and appear radiometrically warm, indicating organic materials. Dunes are the youngest units and appear radiometrically warm, indicating organic sediments (Janssen et al. 2016). The plains are younger than both the mountainous/hummocky and the labyrinth unit classes. Undifferentiated Plains form the most widespread unit on Titan and are interpreted as aeolian deposits that also appear radiometrically warm (Lopes et al. 2016). Dunes and lakes are the youngest unit classes on Titan; it is likely that the processes forming them are still active. Characterization and comparison of the properties of the unit classes and the individual features with data from radiometry, ISS, and VIMS provide information on their composition and possible provenance. VIMS analysis shows that compositional variations can also exist within the same class of unit (Lopes et al. 2016; Solomonidou et al. 2016). For example, undifferentiated plains located closer to the equatorial dunes appear to be contaminated by dune materials. The correlations among the data sets not only aid in the interpretation of their origin, but also allow us to infer global distributions within regions not covered by SAR. This is particularly important as SAR data did not provide complete coverage of Titan during the Cassini mission.

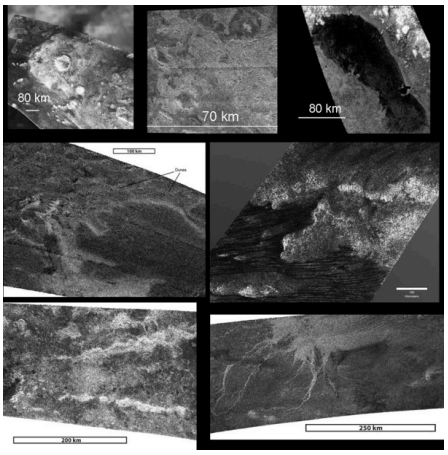

Figure 1. Examples of geologic features on Titan: Top row from left: Sinlap crater with its well-defined ejecta blanket. Middle: Craterform structure (suspected impact crater) in the Xanadu region. Right: Ontario Lacus near Titan's south pole. Middle row, left: Bright (high radar backscatter) deposit Winia Fluctus abutting against darker undifferentiated plains, dunes indicated overlaying part of deposit. Middle row, right: Dunes abutting against hummocky and mountainous terrain. Bottom left: mountains (radar bright) in the equatorial region. Right: Elivagar Flumina, interpreted as a large fluvial deposit, showing braided radar-bright channels. Deposits overlay radar-dark undifferentiated plains.

Acknowledgements

This research was supported by the Cassini Data Analysis and Participating Scientists Program (CDAPS) grants #NZ15-CDAPS15_20062 and #NH16ZDA001N to RL. This work was conducted at JPL/Caltech under contract with NASA. Copyright 2015, California Institute of Technology. Government sponsorship is acknowledged.

References

Birch, S., et al., Icarus, 282, 214-236, 2017
Janssen, M., et al., Icarus 270, 443-459, 2016
Lopes, R.M.C., et al., Icarus, 205, 540-588, 2010
Lopes, R.M.C., et al., Icarus, 270, 162-182, 2016
Malaska, M., et al., Icarus, 270, 130-161, 2016
Porco, C., et al., Space Science Rev., 115, 363-497, 2004
Solomonidou, A., et al., Icarus, 270, 85-99, 2016
Solomonidou, A., et al., this meeting.

EPSC Abstracts
Vol. 11, EPSC2017-84-4, 2017
European Planetary Science Congress 2017

On use of electrodynamic tethers for Saturn missions I

Jesús Peláez, **Juan R. Sanmartín** and Elena Fantino
Universidad Politécnica de Madrid (**juanr.sanmartin@upm.es**)

Abstract

Exploring the moons of *Saturn*, particularly *Enceladus*, is an important goal of planetary science, the more so for search of life outside the Earth. Whereas use of *Electrodynamic Tethers* is readily possible for Jupiter [1], the case for the 3 other Outer Giant Planets, Saturn, Uranus and Neptune, presents issues, basically because their magnetic self-field B is grossly weaker, surface values being about 5% of the Jovian value; the efficiency of spacecraft capture (S/C-to-tether mass ratio) goes down as B^2 for low enough field. On the other hand, a possible gain by a factor of 2 in the efficiency arises from the low B value itself and the ensuing weak Lorentz drag, requiring no tether spin, as opposite the Jovian case, to keep it from bowing.

From the orbital point of view, capture is an essential issue for a tether mission to Saturn, because there will be only one opportunity for success. Once the tethered spacecraft is captured by the gravity of Saturn, a space tether could carry a spacecraft through the *neighborhoods* resorting to neither propellant nor power supply [2]. The basic scenario for the capture is described in [3] for the case of Jupiter; such analysis must be adapted to Saturn, but such adjustment is not trivial.

In the present work we consider ways to further increase the efficiency. First, moving from standard tether use of aluminium to beryllium, in case it could be made ductile enough, increasing the ratio between electrical conductivity and density by a factor of 1.8, an important parameter for efficiency. Additionally, ensuring that the length-averaged current in the tether is close to its short-circuit, upper-bound value, by choosing it long and thin enough; this raises no issues as in the Jovian case [1], again because of the very low Saturn field B.

Secondly, by introducing a gravity assist from some Saturn's moon. Table 1 shows some facts of the main moons. Titan, orbiting Saturn at $19.88R_S$ with mass $2.366 \cdot 10^{-4} M_S$, as against moon Ganymede, orbiting Jupiter at $15.0R_J$ with mass $0.79 \cdot 10^{-4} M_J$, is the more promising.

Table 1: Main moons of Saturn

Moon	Mass	Orb. radius	Eccent.
Tethys	$1.086 \cdot 10^{-7} M_S$	$4.888 R_S$	0.0001
Dione	$1.926 \cdot 10^{-6} M_S$	$6.225 R_S$	0.0022
Rhea	$4.056 \cdot 10^{-6} M_S$	$8.694 R_S$	0.0002
Titan	$2.366 \cdot 10^{-4} M_S$	$19.88 R_S$	0.0288
Iapetus	$3.175 \cdot 10^{-6} M_S$	$58.73 R_S$	0.0293

Assuming a Hohmann transfer to Saturn, the goal is to turn the initial hyperbolic trajectory —relative to Saturn— into an elliptical one with negative keplerian energy. Such depletion of energy is performed by the electrodynamic drag provided by the tether with the help of some flyby around Titan. We use some of the ideas described in [4] for

the Giant Jupiter adapting them to the Saturn planet.

This simple model must be tested considering impact trajectories from Earth to Saturn using the *circular restricted three body problem*. The CRTBP permits to obtain with more precisión the arrival velocity to the sphere of influence of Saturn, one of the main parameter of the analysis.

The main figures of the Saturn Orbit Insertion (SOI) of the Cassini S/C are: $\Delta V = 626.8$ m/s, duration 5780.5 s, fuel consumed 841.5 kg and average thrust during the maneuver 443.1 Nw. In the case considered in this work, the gravity-assist maneuver aims to facilitate and to guarantee the capture and is quite different from the gravity-assist maneuvers around Titan performed in the Cassini mission.

References

[1] Juan R Sanmartín, Mario Charro, Henry B Garrett, Gonzalo Sánchez-Arriaga, and Antonio Sánchez-Torres. Analysis of tether-mission concept for multiple flybys of moon europa. *Journal of Propulsion and Power*, 33:338—342, 2017.

[2] Juan R. Sanmartin and Enrico C. Lorenzini. Exploration of outer planets using tethers for power and propulsion. *Journal of Propulsion and Power*, 21(3):573–576, 2005.

[3] Juan R. Sanmartin, Mario Charro, Enrico C. Lorenzini, Henry Garrett, Claudio Bombardelli, and Cristina Bramanti. Electrodynamic tether at jupiter – I: Capture operation and constraints. *IEEE Transactions on Plasma Science*, 36(5):2450–2458, 2008.

[4] Alfred E. Lynam and James M. Longuski. Interplanetary trajectories for multiple satellite-aided capture at jupiter. *Journal of Guidance, Control, and Dynamics*, 34(5):1485–1494, 2011.

EPSC Abstracts
Vol. 11, EPSC2017-85-1, 2017
European Planetary Science Congress 2017

On use of electrodynamic tethers for Saturn missions II

Juan R. Sanmartín (1), Jesús Peláez (1), Henry B. Garrett (2) and Ignacio Carrera (1)
(1) Universidad Politécnica de Madrid, (2) JPL/California Institute of Technology,
(juanr.sanmartin@upm.es)

Abstract

Recent NASA news on chemicals favouring life being detected in geyser plumes ejected from moon *Enceladus* has brought back interest for exploration of the moons of *Saturn*. The case for using *electrodynamic tethers* for Saturn missions presents, however, a basic issue in its quite weak magnetic self-field $\mathbf{B}$ as compared with Jupiter, where tether use does appear readily possible [1, 2]. The planetary-surface B value for Saturn is about 5% of the corresponding Jovian value, while tether efficiency of spacecraft capture (S/C-to-tether mass ratio) goes down as B^2 for low enough field. This is compounded for Saturn by its comparatively low mean-density and fast rotation among the four *Giant Outer* planets, resulting in a relatively short *reach* of Lorentz-drag on a tether, as indicated by the low ratio of radius at the stationary circular orbit, a_s, to the planet radius R, ambient values B_s and plasma density N_s characterizing the capture operation.

In this work we show that, nonetheless, tether drag (a thermodynamic effect [3], like its capability to generate power), can effect capture of a spacecraft incoming from a *Hohmann Earth* transfer, with S/C-to-tether mass ratio about 3, as already found possible for Jupiter too [2]. The capture *perijove* radius would be about R_S, just hundreds of kilometres above the planet, and the tether-tape chosen long enough to ensure that its length-averaged current is close to the short-circuit, upper-bound value; this raises no issues as in the Jovian case [2], —where current is well below the corresponding short-circuit value— because of the very low Saturn field B itself. In this respect, a rough Chamberlain model [4] of the ambient plasma density is developed from measurements carried out at the Cassini mission.

Further, there is a gain in capture efficiency by a factor just about 2, arising again from the low B itself and the ensuing weak Lorentz drag, requiring no tether spin to keep it from bowing, as opposite the Jovian case. Finally, a similar increase in efficiency involves moving the capture orbit from pro-grade to retrograde, which eliminates drag-reach considerations, the positive effect on capture being sensible for a low prograde-reach case such as the Saturn one.

References

[1] Juan R. Sanmartin, Mario Charro, Enrico C. Lorenzini, Henry Garrett, Claudio Bombardelli, and Cristina Bramanti. Electrodynamic tether at jupiter – I: Capture operation and constraints. *IEEE Transactions on Plasma Science*, 36(5):2450–2458, 2008.

[2] Juan R Sanmartín, Mario Charro, Henry B Garrett, Gonzalo Sánchez-Arriaga, and Antonio Sánchez-Torres. Analysis of tether-mission concept for multiple flybys of moon europa. *Journal of Propulsion and Power*, 33:338—342, 2017.

[3] Juan R. Sanmartín. A review of macroscopic motion in thermodynamic equilibrium. https://arxiv.org/abs/1703.02884, 2017.

[4] Joseph W Chamberlain. Planetary coronae and atmospheric evaporation. *Planetary and Space Science*, 11(8):901–960, 1963.

EPSC Abstracts
Vol. 11, EPSC2017-88, 2017
European Planetary Science Congress 2017

Constraining the composition and geological history of the main types of terrains found in the equatorial belt of Titan

J. F. Brossier (1), S. Rodriguez (2), T. Cornet (2), L. Maltagliati (3), A. Lucas (2), S. Le Mouélic (4), A. Solomonidou (3,5), A. Coustenis (3), M. Hirtzig (3,6), R. Jaumann (1), K. Stephan (1), and R. H. Brown (7).
(1) Institute of Planetary Research, German Aerospace Center (DLR), Berlin, Germany (Jeremy.Brossier@dlr.de), (2) Laboratoire Astrophysique, Instrumentation et Modélisation (AIM), Université Paris-Diderot, CEA-Saclay, Gif-sur-Yvette, France, (3) Laboratoire d'études spatiales et d'instrumentation en astrophysique (LESIA), Paris-Meudon, France, (4) Laboratoire de Planétologie et Géodynamique, Université of Nantes, France, (5) Jet Propulsion Laboratory, California Institute of Technology, Pasadena, CA, USA, (6) Fondation "La main à la pâte", Montrouge 75006, France, (7) Lunar and Planetary Laboratory, Univ. Arizona, Tucson, USA.

1. Introduction

Over these twelve past years, near-IR imaging data from the Visual and Infrared Mapping Spectrometer (VIMS) onboard Cassini [1] gave significant hints on the spectroscopic and geological diversity of the terrains on Titan's surface. The composition of those terrains still remains unconfirmed yet. Nonetheless, by applying a newly updated radiative transfer model [2,3], we provide excellent constraints on the composition and structure for the main IR-units present in the equatorial regions (±40°N/S) [4]. Indeed, by combining this method of correction with a spectral mixing model for water ice and tholins, we determine the main chemical species present within IR-units and relate them to the observed geomorphology. We therefore propose a scenario that could lead to the current distribution of the IR-units.

2. Methods and Data

To unveil the surface, it is imperative to remove the atmospheric effects (gases absorption and haze scattering) in the VIMS data. A radiative transfer model [2,3] is therefore used to evaluate those effects and retrieve the surface albedo in our considered IR-units, meaning the equatorial IR-bright, -brown and -blue terrains [5,6]. Those terrains were described as being compositionally and structurally distinct [4]. For comparison purposes, we use a spectral mixing model for water ice and tholins to produce a vast spectral library of linear mixtures, by varying the grain sizes and mixing fraction of both components. Water ice and tholins are thought to be abundant on Titan's surface, regarding studies from and prior Cassini-Huygens mission. We first calculate synthetic albedos based on the formalism developed by Hapke [7], and then compare them with those of IR-units. Thus by coupling both radiative transfer and spectral mixing models, we retrieve all the possible water ice and tholins mixtures in our terrains. Additionally, SAR swaths derived from the RADAR instrument are used for geomorphological identification and mapping purposes. Indeed, they provide details about the surface properties of the terrains of interest, and hence contribute in our geological interpretation.

3. IR-units' Composition

The spectral mixing model provides new relevant informations about the content and grain sizes of both water ice and tholins of IR-units. Here, we assume that tholins synthetized in the laboratories by Khare [8] are similar to the aerosols photochemically produced in Titan's atmosphere. Considering our results, IR-bright terrains appear to be strongly dominated by tholins of a few tens of microns in diameter. Those small grained tholins must result from the atmospheric fallout. Haze particles are produced in the atmosphere and fall down with a size reaching up to ten microns near the surface [9]. IR-brown terrains, for their part, are predominantly made of larger grained tholins, with possible traces of water ice. Finally, IR-blue terrains are also made of large grained tholins but present a slight enrichment in water ice relative to the other considered terrains.

4. Geological Interpretation

IR-bright might be mainly covered by haze particles that form organic sediment coating the icebed. IR-blue terrains surrounding impact craters are thought to result from the deposition of excavated icebed material after the impact [10]. Whereas those found in IR-bright terrains may correspond to icebed outcrops in strongly degraded SAR-bright terrains, such as mountains and craters flanks (i.e. rough terrains). After being eroded by methane rainfalls and winds,

debris (icebed and organic materials) are transported via channels flowing across the plains to the margins and ending into IR-blue terrains, as suggested in previous studies [11-13]. This deposition could lead to the formation of outwash plains with icy blocks and pebbles, like those seen at the Huygens landing site [14]. As most icy debris are washed out in IR-blue terrains, the neighboring IR-brown terrains, corresponding to dunes in SAR swaths [4,15], should be mainly made of organic sand. Indeed, in IR-brown dunes areas, tholins grains are large enough to form dunes by saltation [16]. Thus, this distribution is very similar to that of a transition from mountains to stony and sandy deserts in Earth (Fig. 1). IR-blue terrains would be referred to terrestrial stony deserts, where icy blocks and pebbles are laying after erosion and deposition processes from the IR-bright terrains. Conversely, IR-brown dunes areas would be the sandy deserts that are mainly covered by longitudinal dunes in the case of Titan.

5. Conclusion

Our spectral mixing model helps in better constraining the compositional and structural relations between the IR-units present in the Titan's equatorial belt. Since large grained tholins are present in both IR-brown dunes areas and IR-blue terrains, this could explain their dark albedo relative to the IR-bright terrains. Indeed, the latter terrains are only made of small grained tholins, although their size can change with subsequent processes such as compaction and sintering [17]. Plus, variations between the IR-brown and -blue terrains must be associated with the water ice content, which is higher in IR-blue terrains. Finally, we propose a series of events that could lead to the current distribution of IR-units seen through imaging data from Cassini's instruments.

References

[1] Brown, R. H. et al. (2005) *SSR*. [2] Hirtzig, M. et al., (2013) *Icarus*, 226. [3] Maltagliati, L. et al. (2015) *EPSC*. [4] Brossier, J. F. et al. (2017) *LPSC*. [5] Barnes, J. W. et al. (2007a) *Icarus*, 186. [6] Soderblom, L. A. et al. (2007) *PSS*, 55. [7] Hapke, B. (2012) *Cambridge Uni. Press*. [8] Khare, B. N. et al. (1984) *Icarus*, 60. [9] Tomasko, M. G. et al. (2008) *PSS*, 56. [10] Le Mouélic, S. et al. (2008) *JGR*, 113. [11] Rodriguez, S. et al. (2006) *PSS*, 54. [12] Barnes, J. W. et al. (2007b) *JGR*, 112. [13] Jaumann, R. et al. (2008) *Icarus*, 197. [14] Tomasko, M. G. et al. (2005) *Nature*, 438. [15] Rodriguez, S. et al. (2014) *Icarus*, 230. [16] Lorenz, R. D. (2014) *Icarus*, 230. [17] Barnes J. W. et al. (2015) *PS*, 4.

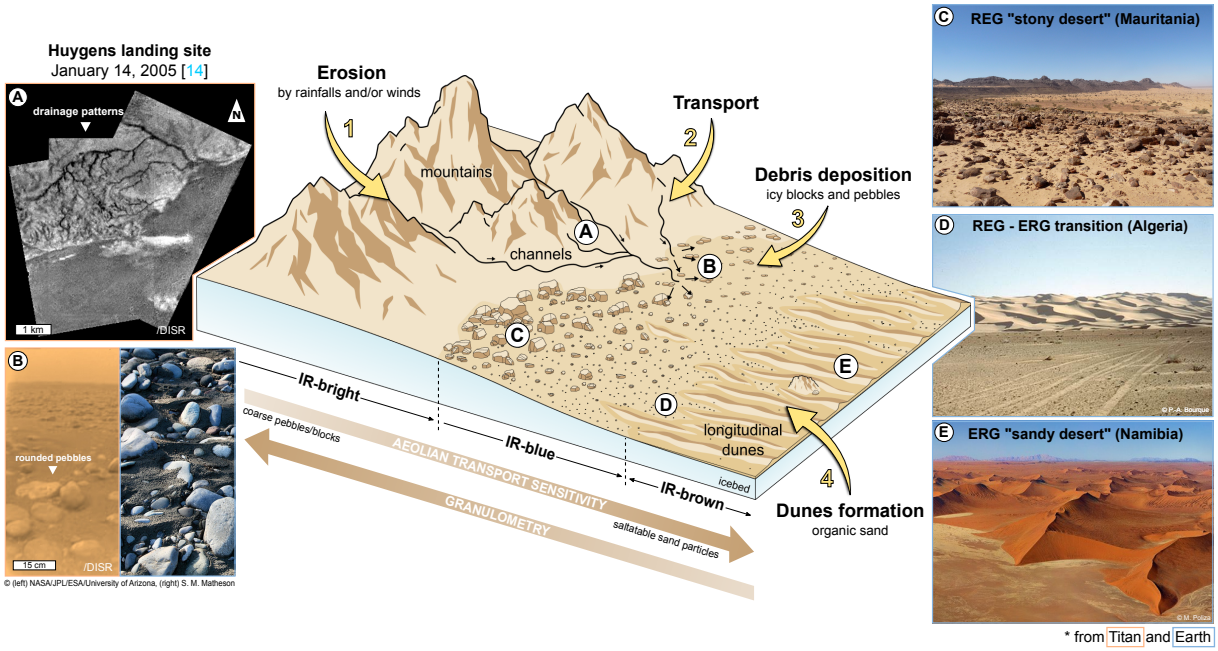

▲ **Figure 1** – Cartoon model illustrating a typical transition from the mountainous terrains to the dunes areas in Titan's equatorial regions, displaying similar landscapes than those observed in terrestrial deserts.

EPSC Abstracts
Vol. 11, EPSC2017-114-1, 2017
European Planetary Science Congress 2017

The seasonal evolution of organic chemistry in Titan's stratosphere from CASSINI/CIRS

A. Coustenis[1], D. E. Jennings[2], R. K. Achterberg[2,3], P. Lavvas[4], G. Bampasidis[5], V. Cottini[2,3], C. A. Nixon[2], F. M. Flasar[2]

[1]LESIA, Observatoire de Paris, PSL-Research Univ., CNRS, Univ. Paris 6, Sorbonne Univ., Univ. Paris-Diderot, Sorbonne Paris-Cité, 5, 92195 Meudon Cedex, France; [2]NASA Goddard Space Flight Center, Greenbelt, MD 20771, USA; [3]Department of Astronomy, University of Maryland, College Park, MD 20742, USA; [4]GSMA, Université Reims Champagne-Ardenne, France.; [5]Faculty of Physics, National and Kapodistrian University of Athens, Panepistimioupolis, 15783 Zographos, Athens, Greece.

Abstract
In the past 5-6 years, we observe the onset and enhancement at Titan's south pole of several trace species such as HC3N and C6H6 previously observed only at high northern latitudes. This is due to the transition of Titan's seasons from northern winter in 2002 to (late) northern spring in 2012 and the advent of winter in the south pole, during which time species with longer chemical lifetimes remain in the north for a little longer undergoing slow photochemical destruction, while those with shorter lifetimes disappear, reappearing in the south. We will present an analysis of nadir spectra acquired by Cassini/CIRS at high resolution in the past years (Coustenis et al. 2016 and references therein) and new searches for more complex molecules in the compositionally enhanced polar regions.

1. Context/Data
Previously, trace gaseous species were found to be enhanced in Titan's North pole, but with the change in seasons and notably since 2012, a dramatic change is found close to the south pole, with a strong decrease in temperature and higher concentrations of gases and condensates. Meanwhile, gases transported north during the previous season remained concentrated around the north pole, undergoing slow photochemical destruction. Following the northern winter, species with longer chemical lifetimes should remain in the north for a little longer while those with shorter lifetimes disappear, reappearing in the south.

2. Analysis
We will present an analysis of spectra acquired by Cassini/CIRS at high resolution from 2010 onwards, in nadir mode [1]. We use a radiative transfer code adapted to Titan's atmosphere (ARTT, [1]) and we extract the temperature profile from the 7.7 micron methane band that we use then in the rest of the spectrum to solve for the abundances of trace gases and their isotopes in the FP3 and FP4 CIRS spectra.

3. Results
We find that as the Southern hemisphere moved into winter after 2010, strong temperature variations are observed essentially in the south pole. Small temperature differences were found for the mid and high northern latitudes. Differences in the 10-15 K range drop in temperature are found for the 50°S (left, full lines). Spectacular T drop by as much as 40 K in 70°S from 2010 to 2014. See [1] for more details. So that it is notable that we see more than 25° decrease in 2 years (2012-2014) near the South pole while at the North it took 3 years to gain 10 K since 2013.

Subsidence gases that accumulate in the absence of ultraviolet sunlight, increased quickly since 2012 and some of them may be responsible also for the haze decrease in the north and its appearance in the south at the same time [2]. For some of the most abundant and longest-lived hydrocarbons the evolution in the past years at a given latitude is not significant until mid-2013 [1]. But in more recent dates, these molecules show a dramatic trend for increase in the south. The 70°S and mid-latitudes show different behavior indicative of different dynamical processes in and out of the polar vortex region. While the 70°N data show generally no change with a trend rather to a small decrease for most species within 2014 the 70°S results indicate a strong enhancement in trace stratospheric gases after 2012. This is a strong indication of the rapid and sudden buildup of the gaseous inventory in the southern stratosphere during 2013-2014, as expected as the pole moves deeper into winter shadow. The limb spectra also show variations in time with altitude, with in particular, in early 2016, a zone depleted in molecular gas and aerosol in the entire northern hemisphere between 400 and 500 km, suggesting a complex unknown dynamical effect [3].

Subsidence gases that accumulate in the absence of ultraviolet sunlight, increased quickly since 2012 and some of them may be responsible also for the haze decrease in the north and its appearance in the south at the same time [4]. For some of the most abundant and longest-lived hydrocarbons the evolution in the past years at a given latitude is not significant until mid-2013 [1,2]. But in more recent dates, these molecules show a dramatic trend for increase in the south. The 70°S and mid-latitudes show different behavior indicative of different dynamical processes in and out of the polar vortex region.

Due to the rapid increase of trace gases in the South and the advantage of large spectral averages now available from CIRS measurements, we are in the process of searching for complex molecules predicted by photochemical models (by P. Lavvas) to exist in Titan's stratosphere (such as butane, acetonitrile, acrylonitrile, proprionitrile, etc) and not yet observed at all or with Cassini. We will describe the results and infer the possible highest degree of organic chemistry available on Titan.

4. Conclusion and future work

Following the northern winter, species with longer chemical lifetimes linger in the north while those with shorter lifetimes disappear, and reappear in the south. The northern composition decrease sets in only about 3 years after the South enhancement has began its dramatic increase

Where we have data, we search for signatures of weak gases in large spectral averages around the poles stratospheres and determine abundances and link to the upper atmosphere and better definition of chemical paths

We plan to search for condensate signatures of these weak gases to match with available data. We stress the need for reliable and complete spectroscopic data to analyse the observations both for gas and solids

This work helps set strong constraints on photochemistry and circulation models

The lack of observations of Titan's atmosphere near the poles begs for return to Titan with dedicated mission, after the upcoming end of the fabulous Cassini-Huygens mission in Sept. 2017 !!!!

References

[1] Coustenis, et al., Icarus 207, 461, 2010 ; Icarus, 270, 409, 2016 ; [2] Jennings et al., ApJ 804, L34, 5, 2015; [3] Vinatier et al. Icarus 250, 95, 2015.[4] Bampasidis et al., Astroph. J., 760, 144, 2012

EPSC Abstracts
Vol. 11, EPSC2017-138, 2017
European Planetary Science Congress 2017

Time-dependent solution for reorientation of rotating tidally deformed visco-elastic bodies

H. Hu , W. van der Wal and L.L.A.Vermeersen
Delft University of Technology, Delft, Netherlands (h.hu-1@tudelft.nl)

Abstract

A new semi-analytical method is established to calculate the time-dependent solution for reorientation of co-rotating tidally deformed bodies. Compared with the widely used fluid limit solution by [*Matsuyama and Nimmo* (2007)], a more accurate time-dependent reorientation path can be obtained. We will use this method to constrain the interior viscosities of Pluto based on recent discoveries from the New Horizons mission.

1. Introduction

Many icy satellites or planets contain features which suggest a (past) reorientation of the body, such as the tiger stripes on Enceladus and the heart-shaped Sputnik Planum on Pluto. Most of these icy bodies are tidally locked and this creates a large tidal bulge which is about three times as large as its centrifugal (equatorial) bulge. To study the reorientation of such rotating tidally deformed body is complicated and most previous studies apply the so-called fluid limit method. The fluid limit approach ignores the viscous response of the body and assumes that it immediately reaches its fluid limit when simulating the reorientation due to a changing load. As a result, this method can only simulate cases when the change in the load is much slower than the dominant viscous modes of the body. For other kinds of load, for instance a Heaviside load due to an impact which creates an instant relocation of mass, it does not give us a prediction of how the reorientation is accomplished (e.g. How fast? Along which path?). Here, we seek a dynamic solution which can provide this answer.

2. Method

2.1 Moment of Inertia

The change in the inertia tensor for a centrifugally and tidally deformed body is given by

$$\begin{aligned}\Delta I_{ij}(t) = &\frac{k^T(t)a^5}{3G} * [\omega_i(t)\omega_j(t) - \frac{1}{3}\omega^2(t)] \\ &+\frac{k^T(t)a^5}{3G} * [\bar{\omega}_i(t)\bar{\omega}_j(t) - \frac{1}{3}\bar{\omega}^2(t)] \\ &+\delta(t) + k^L(t)] * C_{ij}(t)\end{aligned} \quad (1)$$

where $\boldsymbol{\omega}$ and $\bar{\boldsymbol{\omega}}$ are vectors of rotation and tidal potential, the magnitude of $\bar{\boldsymbol{\omega}}$ is usually $\sqrt{3}$ times $\boldsymbol{\omega}$ for most icy moons. This equation can be solved analytically by linear change assumptions or calculated numerically with a finite-element package.

2.2 Liouville equation

With the information of the deformation, the reorientation is obtained by combining the perturbation of rotational and tidal axes. Both can be obtained from a general linearized Liouville equation

$$m_1(t) = \frac{\Delta I_{13}(t)}{C-A} + \frac{C\Delta\ \dot{I}_{23}\ (t)}{\Omega(C-A)(C-B)} \quad (2a)$$

$$m_2(t) = \frac{\Delta I_{23}(t)}{C-B} - \frac{C\Delta\ \dot{I}_{13}\ (t)}{\Omega(C-A)(C-B)} \quad (2b)$$

Here m_1 and m_2 are the perturbation in the plane perpendicular to the rotational and tidal axes.

2.3 An iterative procedure

An iterative algorithm which is shown in [*Hu al.* (2017)] is applied in each time step:

Algorithm

1. Assume that the step i, from time t_i to t_{i+1}, starts with the direction of the rotational axis given by $\boldsymbol{\omega_r^i} = \Omega_r^i(\omega_1^i, \omega_2^i, \omega_3^i)^T$ and the direction of the tidal axis by $\boldsymbol{\omega_t^i} = \Omega_t^i(\omega_4^i, \omega_5^i, \omega_6^i)^T$ in which $(\omega_1^i, \omega_2^i, \omega_3^i)^T$ and $(\omega_4^i, \omega_5^i, \omega_6^i)^T$ are unit column

vectors which satisfy $\omega_1^i\omega_4^i + \omega_2^i\omega_5^i + \omega_3^i\omega_6^i = 0$. For the first iteration, we assume that the rotation and tidal axes in this step do not change: $\boldsymbol{\omega_r^{i+1}} = \boldsymbol{\omega_r^i}$ and $\boldsymbol{\omega_t^{i+1}} = \boldsymbol{\omega_t^i}$.

2. Apply both the centrifugal and tidal potential to the model and solve the equation 1. Obtain the total change in the inertia tensor and its derivative as $\Delta\mathbf{I}$ and $\Delta\dot{\mathbf{I}}$. The coordinate transformation matrix from the body-fixed to the bulge-fixed coordinate system is given by

$$\mathbf{U} = [\boldsymbol{\omega_t^{i+1}}, \boldsymbol{\omega_r^{i+1}} \times \boldsymbol{\omega_t^{i+1}}, \boldsymbol{\omega_r^{i+1}}] \tag{3}$$

The local values of the inertia tensor for the centrifugal part are obtained by $\Delta\mathbf{I}_1 = \mathbf{U}^T\Delta\mathbf{I}\,\mathbf{U}$ and $\Delta\dot{\mathbf{I}}_1 = \mathbf{U}^T\Delta\dot{\mathbf{I}}\,\mathbf{U}$. The corresponding inertia tensors for calculating tidal perturbation are $\Delta\mathbf{I}_2 = -\mathbf{S}^T\Delta\mathbf{I}_1\,\mathbf{S}$ and $\Delta\dot{\mathbf{I}}_2 = -\mathbf{S}^T\Delta\dot{\mathbf{I}}_1\,\mathbf{S}$. $\mathbf{S}$ is the transformation matrix between frames where the Z-axis is the rotational axis and the tidal axis.

3. Apply equation 2 to $\Delta\mathbf{I}_1$ and $\Delta\dot{\mathbf{I}}_1$ and obtain the perturbation for the rotational axis as $\Omega_1(m_1, m_2, m_3)$. Apply equation 2 to $\Delta\mathbf{I}_2$ and $\Delta\dot{\mathbf{I}}_2$ and obtain the perturbation for the tidal axis as $\Omega_2(m_1', m_2', m_3')$. Then we have the perturbed Z- and X-axis as $\mathbf{Z}' = \Omega_1(m_1, m_2, 1 + m_3)^T$ and $\mathbf{X}' = \Omega_2(1 + m_3', m_2', -m_1')^T$. We normalize these vectors as $\mathbf{Z}' = \Omega_r^{i+1}\bar{\mathbf{Z}}'$ and $\mathbf{X}' = \Omega_t^{i+1}\bar{\mathbf{X}}'$. The local coordinate transformation matrix from the bulge-fixed frame at time t_i to the new frame at time t_{i+1} is obtained as $\mathbf{V} = [\bar{\mathbf{X}}', \bar{\mathbf{Z}}' \times \bar{\mathbf{X}}', \bar{\mathbf{X}}' \times (\bar{\mathbf{Z}}' \times \bar{\mathbf{X}}')]$. The updated direction of the rotational and tidal axes in the original body-fixed coordinates are obtained as

$$\boldsymbol{\omega_r^{i+1}} = \Omega_r^{i+1}\mathbf{U}\mathbf{V}[0, 0, 1]^T \tag{4a}$$
$$\boldsymbol{\omega_t^{i+1}} = \Omega_t^{i+1}\mathbf{U}\mathbf{V}[1, 0, 0]^T \tag{4b}$$

4. Substitute $\boldsymbol{\omega_r^{i+1}}$ and $\boldsymbol{\omega_t^{i+1}}$ in step 2 until the results converge.

3. Results

We use a Triton model which contains a 10 km lithosphere for demonstration. For a Heaviside load, the fluid limit solution can only provide the end position of a reorientation. We want to demonstrate the reorientation due to accumulated ice caps at the polar area. In the following figure, a point mass is attached to the surface at 15 degree colatitude and longitude. The coloured dots represent the position where

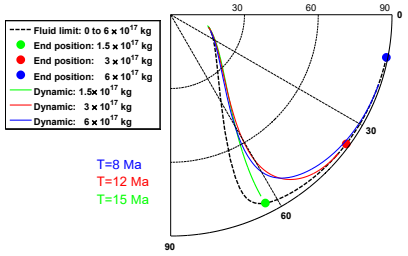

Figure 1: A view of the body in the direction of the rotational axis where the 0 degree longitude line is the direction of the tidal force. The reorientation of each Heaviside type mass anomaly is calculated with time T million years.

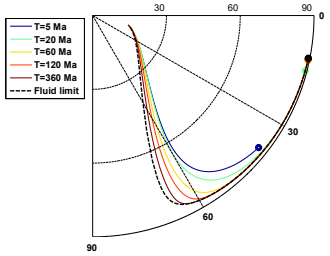

Figure 2: A mass anomaly which increase from 0 to $6 \times 10^{17} kg$ linearly in T million years.

the point mass would end as calculated by the fluid limit solution [*Matsuyama and Nimmo* (2007)]. The coloured lines are the dynamic solutions obtained by our method which suggest a different path. Given a reorientation end position and the history of the loading, we can use our method to constrain the interior viscosities of the model and give a more accurate reorientation path.

Acknowledgements

This research has been financially supported by the GO program of The Netherlands Organization for Scientific Research (NWO), project number: ALW-GO-12/11.

[*Hu al.* (2017)] Hu, H., W. van der Wal and B. Vermeersen, A numerical method for reorientation of rotating tidally deformed visco-elastic bodies, *Journal of Geophysical Research: Planets*, 2016JE005114.

[*Matsuyama and Nimmo* (2007)] Matsuyama, I., and F. Nimmo (2007), Rotational stability of tidally deformed planetary bodies, *Journal of Geophysical Research: Planets*, *112*(E11).

EPSC Abstracts
Vol. 11, EPSC2017-139, 2017
European Planetary Science Congress 2017

N_2 in Pluto's Northern Lowlands

L. A. Young (1), J. A. Stansberry (2), S. Protopapa (3), B. Schmitt (4) A. M. Earle (5), P. M. Schenck (6) A. D. Howard (7), and the New Horizons science team
(1) Southwest Research Institute, Colorado, USA (layoung@boulder.swri.edu), (2) Space Telescope Science Institute, Maryland, USA, (3) University of Maryland, Maryland, USA, (4) Université Grenoble Alpes, France, (5) MIT, Massachusetts, USA, (6) Lunar and Planetary Institute, Texas, USA, (7) University of Virginia, Virginia, USA.

Abstract

On Pluto, N_2-rich ice is seen at 35° to ~60° N latitude, with incursions up to 75° N [1]. The Northern incursions are mostly in smaller, flat-bottomed lowlands south of 70°. Both shadowing by canyon walls and the higher frost point at higher pressures favor N_2 accumulation in depressions. However, neither effect is sufficient to significantly redistribute N_2 ice over a single Pluto year, suggesting that the N_2 in the northern valleys is laid down over multiple Pluto seasons.

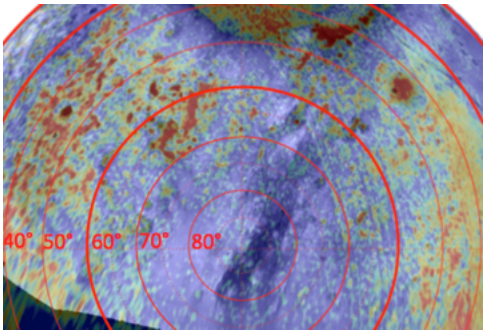

Figure 1. Shading denotes elevation (dark is deep, with the deepest canyons being ~2.5 km below the mean radius of Pluto). Color denotes N_2 band strength (red for more N_2 ice or larger grain size, blue for lack of detectable N_2). 180° longitude is up.

1. Introduction

Pre-encounter simulations of Pluto's seasons suggested that once sublimation of Northern N_2 begins post-perihelion (Northern summer), it should leave the Northern hemisphere bare on a timescale of only ~1 or 2 years [2], accompanied by a severe drop in the pressure. New Horizons found N_2 in northern mid latitudes, with scattered N_2 in the far north (Fig 1). The N_2 north of ~60° is confined to local depressions, with less N_2 in the far North, or in shallower or larger depressions (note the lack of N_2 in the low, wide feature straddling the North Pole). Thus we investigate N_2 stability vs. latitude, altitude, and shadowing by valley walls.

2. Method

The temperature of the N_2 ice on Pluto's surface will be at the "frost point," which depends on the globally averaged energy balance of the N_2 ice; the surface pressure then follows from vapor-pressure equilibrium [3]. The N_2 ice on depression floors will have higher surface pressures, higher surface temperature, and higher thermal emission. Absorbed insolation depends on season, latitude, albedo, and shadowing from canyon walls, so depression floors have potentially less insolation [4]. Local imbalances between emission and insolation are compensated by latent heat of sublimation, so higher frost points and lower insolation both lead to decreased sublimation (or increased deposition) *e.g.* on valley floors. Locally the net sublimation rate (R, cm/s) is found from:

$$(1-A)S(\lambda,\lambda_s,\alpha) - \sigma\varepsilon T(h)^4 = RL/\rho \quad (1)$$

A is the bolometric Bond albedo; as the observed reflectance varies little between lowlands and uplands, we adopted A = 0.8 [5]. S is the absorbed solar flux, which depends on the latitude, λ, the sub-solar latitude, λ_s, and the angle of the horizon, α. σ is the Stefan-Boltzmann constant, and ε is the emissivity, which we take to be unity. T is the temperature of the N_2 ice, which depends on the height h above the mean radius. L is the latent heat (2.5 x 10^9 erg/g), and ρ is the density of the N_2 ice (1.0 g/cm^3). An N_2-covered area can be a site of either condensation or sublimation. A bare area can be a condensation site if T is below the frost point and $R < 0$.

We use the N_2 pressure at h=0 as measured by New Horizons in 2015 [6] and extrapolated to the surface from ground-based stellar occultations 1988-2015 [7], then calculated $T(h=0)$ by vapor-pressure equilibrium. The wet adiabat (-0.1 K/km) defines the pressure and temperature of the N_2 ice on the valley floor, and the resulting difference in the thermal emission relative to ice at the frost point and h = 0 km. The resulting sublimation mass flux will deposit roughly 0.8 cm more N_2 at –2 km vs. 0 km altitude over the interval 1985-2015. Shadowing affects deposition rates by decreasing the solar insolation, especially for small depressions or near valley walls, adding ~3 to 4 cm more N_2 for a 15° vs 0° horizon over the same time span, depending on latitude. Shadowing also extends the duration of the "arctic night," during which a location receives no sunlight over a Pluto rotation, typically by ~30 years, yielding an additional tens of cm of N_2 ice per Pluto year in lowlands vs. highlands.

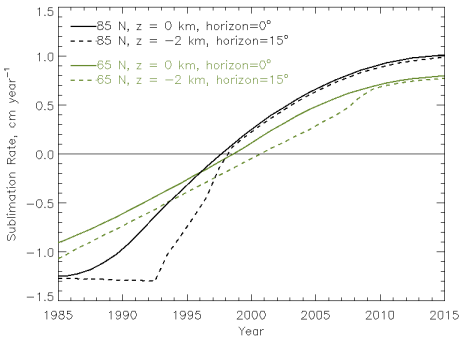

Figure 2: Sublimation Rate for N_2 at 65 N (green) and 85 N (black), on the uplands (solid) or in a depression (dashed). The small offset is due to a higher frost point at lower altitudes. The larger, variable offset is due to shadowing.

While N_2 favors lowlands, it is not a dramatic enough difference to operate over a single Pluto season. Roughly 1 m of N_2 condenses in the northern terrains over the arctic night. But many of the lowland N_2 floors are flat and visually smooth, with evidence of the same deep pitting seen in Sputnik Planitia, suggesting deeper deposits, perhaps built up over many seasons. Only a total of ~7-12 cm of N_2 has sublimed from the highlands this season. This could leave behind a CH_4 crust (~0.5 to 2 mm thick) sufficient to mask the underlying N_2. Alternatively, high thermal inertia may have kept the northern uplands too warm for condensation for most of the previous century. Thus, Pluto's northern N_2 may be perennially dichotomous, as suggested for Triton [8].

Acknowledgements

This work was supported by NASA ROSES NNX15AH35G and the New Horizons project.

References

[1] Protopapa, S, and 21 coauthors: Pluto's global surface composition through pixel-by-pixel Hapke modeling of New Horizons Ralph/LEISA data, Icarus, Vol. 287, pp. 218-228, 2017. Schmitt et al. 2017. Physical state and distribution of materials at the surface of Pluto from New Horizons LEISA spectrometer. Icarus 287, 229-260.

[2] Hansen, C. J. and D. A. Paige 1996. Seasonal nitrogen cycles on Pluto. Icarus 120, 247-265. Young, L. A. 2013. Pluto's seasons: New predictions for New Horizons. The Astrophysical Journal 766, L22. Olkin, C. B., and 23 colleagues 2015. Evidence that Pluto's atmosphere does not collapse from occultations including the 2013 May 04 event. Icarus 246, 220-225. Hansen, C. J., D. A. Paige, and L. A. Young 2015. Pluto's climate modeled with new observational constraints. Icarus 246, 183-191.

[3] Spencer, J. R., J. A. Stansberry, L. M. Trafton, E. F. Young, R. P. Binzel, and S. K. Croft 1997. Volatile Transport, Seasonal Cycles, and Atmospheric Dynamics on Pluto. Pluto and Charon 435.

[4] Trafton, L. M. and J. A. Stansberry 2015. On the departure from isothermality of Pluto's volatile Ice due to local insolation and topography. AAS/Division for Planetary Sciences Meeting Abstracts 47, 210.02.

[5] Buratti, B. J., and 16 colleagues 2017. Global albedos of Pluto and Charon from LORRI New Horizons observations. Icarus 287, 207-217.

[6] Hinson, D. P., and 15 colleagues 2017. Radio occultation measurements of Pluto's neutral atmosphere with New Horizons. Icarus 290, 96-111.

[7] Elliot, J. L., and 28 colleagues 2003. The recent expansion of Pluto's atmosphere. Nature 424, 165-168. Sicardy, B., and 67 colleagues 2016. Pluto's Atmosphere from the 2015 June 29 Ground-based stellar occultation at the time of the New Horizons flyby. The Astrophysical Journal 819, L38

[8] Moore, J. M. and J. R. Spencer 1990. Koyaanismuuyaw - The hypothesis of a perennially dichotomous Triton. Geophysical Research Letters 17, 1757-1760.

EPSC Abstracts
Vol. 11, EPSC2017-153, 2017
European Planetary Science Congress 2017

The Enceladus plume, particle impact ionization and Langmuir Probes: How dusty is the plasma in the plume?

F. Crary, L. Andersson and S. Hsu, University of Colorado, Boulder, Colorado, USA. (frank.crary@lasp.colorado.edu)

Abstract

Very large differences between ion and electron densities have been reported in the Enceladus plume. This difference is attributed to a high density of charge dust particles. This interpretation is sensitive to the analysis of Cassini Langmuir Probe data and, specifically, to how the current from the charged dust particles are included. We present a reanalysis of these data incorporating both the current from the charged dust particles themselves (as was done in past work) and the current due to the impact-generated plasma.

1. Introduction

All During many Enceladus flybys, the Cassini spacecraft's Langmuir Probe has measured ions and electrons in the Enceladus plume. Previous analysis of these data [1] have suggested that, in the core of the plume, the free electron density is much lower than the ion density, sometimes by over two orders of magnitude. The difference is attributed to charged dust particles within the plume. Particles smaller than a few nanometers in size have been directly measured by the Cassini Plasma Spectrometer, while those larger than a few hundred nanometers have been measured by the spacecraft's Cosmic Dust Analyzer. But the majority of the dust charge is on otherwise unmeasured particles in the few to few-hundred nanometer size range. Dust densities of over 50 particles per cubic centimeter have been reported.

2. Currents from charged dust

Given these dust densities, analysis of Langmuir Probe data must account for the currents produced by the dust particles, as well as the commonly-modeled currents from ions, electrons, secondary electrons, etc. Past work [1] has treated the current from charge on the dust particles, $I_d = q_d\ n_d\ u\ A$. However, dust impacts are also known to produce an ionized ejecta cloud. Depending on the size of the impacting particles, the charge from impact ionization may exceed the charge from the dust particles themselves. Based on laboratory measurements of impacts on typical spacecraft materials [2], and at the 7 to 18 km/s velocities of the Cassini encounters, this transition is at 20 to 90 nm.

3. Langmuir Probe Analysis

Here, we present a reanalysis of Cassini Langmuir probe data, including the current from impact ionization as well as that from the charge on the impacting particles. We also report the resulting correlated uncertainty and non-uniqueness of fits to the data.

References

[1] Morooka M. W., et al.: Dusty plasma in the vicinity of Enceladus, Journal of Geophysical Research, Vol. 116, 10.1029/2011JA017038, 2011

[2] Collette, A., Grün, E, Malaspina, D., and Sternovsky, Z.: Micrometeoroid impact charge yield for common spacecraft materials, Journal of Geophysical Research, 10.1002/2014JA020042, 2014.

EPSC Abstracts
Vol. 11, EPSC2017-172-2, 2017
European Planetary Science Congress 2017

Saturn's stratospheric equatorial oscillation and wave activity through the Cassini epoch

S. Guerlet (1), T. Fouchet (2), A. Spiga (1), B. Hesman (3), N. Gorius (4), L. Fletcher (5) and F.M. Flasar (4)
(1) LMD, Sorbonne Universités, UPMC Univ Paris 06, CNRS, Paris, France (2) LESIA, Obs. de Paris, Meudon, France (3) STScI, Baltimore, MD, USA (4) NASA/GSFC, Greenbelt, MD, USA (5) University of Leicester, UK.
(sandrine.guerlet@lmd.jussieu.fr)

Abstract

Thermal infrared spectra acquired by Cassini/CIRS in limb viewing geometry in 2015 are used to derive 2-D latitude-pressure temperature and thermal wind maps in Saturn's stratosphere. These maps are compared to previous observations from 2005 and 2010 to study the evolution of the vertical structure of Saturn's equatorial oscillation between 20 hPa and 0.01 hPa. CIRS nadir spectra are also used to map stratospheric temperatures with longitude. Twelve datasets are selected at different epochs (2005–2015) in the tropical region (20N–20S) : planetary thermal waves are observed in each dataset, suggesting that they are ubiquitous in Saturn's equatorial stratosphere.

1. Introduction

Like the Earth and Jupiter, Saturn's stratosphere harbors a periodic equatorial oscillation of its zonal wind and temperature vertical profiles [1, 5]. By analogy with the Earth Quasi-Biennal Oscillation, these oscillations are thought to be driven by interactions between upward-propagating waves and the mean zonal flow, leading to a vertical oscillation of the zonal wind profile and a descent of wind extrema through the stratosphere. The period of Saturn's Quasi-Periodic Oscillation (QPO) is estimated to 14.7 years, making its observational study a challenging task.

Zonal wind speeds have never been directly measured in Saturn's stratosphere, so that the study of the QPO is done indirectly, through the measurement of associated temperature anomalies that develop in thermal wind balance. Due to the sharp vertical oscillation of the temperature profile on relatively small vertical scales (two temperature and zonal wind extrema are separated by ∼two scale heights), these temperature anomalies have been best resolved using Cassini radio-occultation soundings [6] or thermal infrared spectroscopic measurements in limb-viewing geometry by Cassini/CIRS [3]. These two studies monitored the descent of the temperature anomalies between 2005/2006 and 2009/2010 with a great vertical extent and resolution but a poor temporal coverage.

In parallel, nadir observations by Cassini/CIRS can provide unique longitudinal coverage of the temperature, which is highly valuable to study planetary wave patterns. Currently, our knowledge of equatorial waves activity is limited to the observation of a Rossby-gravity wave of wavenumber 9 in 2005 and 2006 [4]. Here we continue to monitor the descent of Saturn's QPO with the analysis of Cassini/CIRS limb measurements acquired in 2015. We complete this study by analysing CIRS nadir data acquired between 2005 and 2015 to monitor the activity of equatorial, planetary thermal waves.

2. Cassini/CIRS observations

In 2015, spectra of Saturn's thermal infrared radiation were recorded in limb viewing geometry at 17 latitudes between 77N and 77S by the Composite Infrared Spectrometer (CIRS) onboard Cassini. At each latitude, the 10-detector arrays of focal planes FP3 and FP4 are set perpendicular to the limb of the planet and simultaneously record spectra acquired at 10 different tangent altitudes in the range 590–1450 cm^{-1}. We employ the radiative transfer model coupled to the inversion algorithm described in [2] to retrieve vertical temperature profiles from the ν_4 methane band (1200–1370 cm^{-1}, probing the middle stratosphere from 0.01 to 5 hPa) and the H_2 and He collision-induced continuum (590–660 cm^{-1}, probing the lower stratosphere from 1 to 30 hPa). By combining these temperature profiles we obtain the pressure-latitude temperature map shown in Fig. 1 between 20N and 20S.

We have also selected CIRS nadir spectra acquired between 20N and 20S with 360° longitudinal coverage in 2005/2006, 2009/2010 and 2015, *ie.* three epochs for which we have previously retrieved temperature

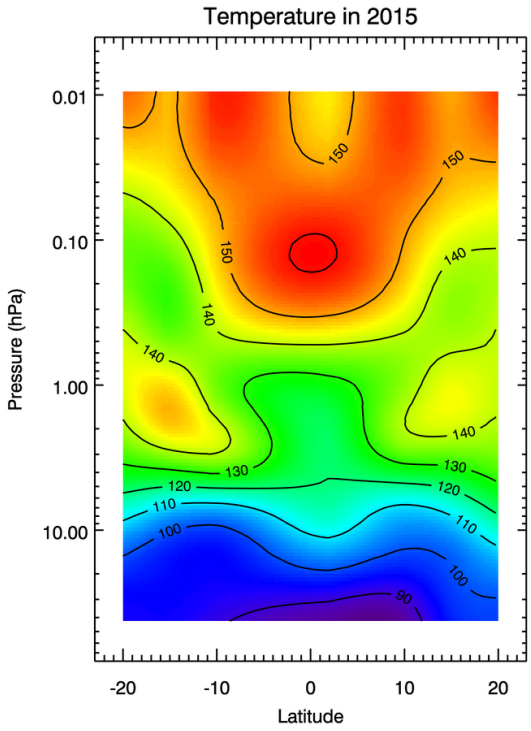

Figure 1: Temperature map (in Kelvin) obtained from Cassini/CIRS limb data acquired in 2015.

profiles from limb datasets. Individual nadir spectra were co-added in 4°-wide latitude bins and 10°-wide longitude bins with a step of 5° in longitude. We employ the same algorithm to retrieve vertical temperature profiles. In nadir geometry, the H_2 and He continuum emission probes upper tropospheric temperatures (80–250 hPa) while the methane emission band probes mid-stratospheric temperatures (0.5–5 hPa).

3. Results

3.1. The evolution of Saturn's QPO

Between 2010 and 2015, Saturn's tropical stratosphere have warmed and cooled in a complex way. Local temperature minima and maxima seen in 2010 have become local maxima and minima in 2015, with changes up to 20K. These extreme changes reflect a change in circulation associated to the descent of the wind extrema. Using the modified thermal wind equation integrated along cylinders, we derive a map of the thermal zonal wind relative to the 20-hPa level that can be compared to previous maps obtained from 2005 and 2010 CIRS limb observations. In 2015, the temperature meridional gradients translate into a local equatorial thermal wind minimum at 0.56-hPa of -100 m/s (relative to the 20-hPa level), surrounded by two local wind extrema, at 5.3 hPa and 0.2 hPa. The descent rate of the oscillation pattern is found faster in the upper stratosphere than in the lower stratosphere, varying between 0.4 and 0.2 scale height per (Earth) year, consistent with a greater wave flux momentum absorbed in the upper stratosphere. This descent rate remains consistent with the previously derived 14.7-yrs period for Saturn's QPO [5].

3.2. Planetary waves

Twelve planetary thermal waves are reported at latitudes 15°N, 15°S or the equator, with wavenumbers between 1 and 9 and amplitudes in the range 2-4K. In two cases we were able to identify them as Rossby waves. This study shows that planetary waves are likely ubiquitous in Saturn's tropical regions and provide constraints to future numerical models.

Acknowledgements

SG, TF and AS are supported by the CNES. We thank the Cassini/CIRS team for their work in the design and calibration of these observations. Farewell to the Cassini spacecraft!

References

[1] Fouchet, T., et al.: An equatorial oscillation in Saturn's middle atmosphere, *Nature*, Vol. *453*, p. 200–202, 2008.

[2] Guerlet, S. et al.: Vertical and meridional distribution of ethane, acetylene and propane in Saturn's stratosphere from CIRS/Cassini limb observations, *Icarus*, Vol. *203*, p. 214–232, 2009.

[3] Guerlet, S. et al.: Evolution of the equatorial oscillation in Saturn's stratosphere between 2005 and 2010 from Cassini/CIRS limb data analysis, *Geophys. Res. Let.*, Vol. *38*, L09201, 2011.

[4] Liming, L., P. J. et al.: Strong jet and a new thermal wave in Saturn's equatorial stratosphere, *Geophys. Res. Let.*, Vol. *35*, L23208, 2008.

[5] Orton, G. S. et al.: Semi-annual oscillations in Saturn's low-latitude stratospheric temperatures, *Nature*, Vol. *453*, p. 196–199, 2008.

[6] Schinder, P. J. et al.: Saturn's equatorial oscillation: Evidence of descending thermal structure from Cassini radio occultations, *Geophys. Res. Let.*, Vol. *38*, L08205, 2011.

EPSC Abstracts
Vol. 11, EPSC2017-201, 2017
European Planetary Science Congress 2017

Retrieval of H_2O abundance in Titan's stratosphere from CIRS and Herschel disc-averaged observations

S. Bauduin (1), P. G. J. Irwin (1), V. Cottini (2), E. Lellouch (3), R. Moreno (3), C. A. Nixon (2) and N. A. Teanby (4)
(1) Atmospheric, Oceanic and Planetary Physics, University of Oxford, Parks Road, Oxford OX1 3PU, UK (2) Planetary Systems Laboratory, NASA Goddard Space Flight Center, Greenbelt, MD 20771, USA (3) LESIA-Observatoire de Paris, CNRS, Université Paris-Diderot, 5 Place Jules Janssen, 92195 Meudon, France (4) School of Earth Sciences, Univerity of Bristol, Wills Memorial Building, Queen's Road, Bristol BS8 1RJ, UK (sophie.bauduin@physics.ox.ac.uk)

Abstract

Since its first measurement 20 years ago by the Infrared Space Observatory (ISO), the water (H_2O) mole fraction in Titan's stratosphere remains uncertain, due to large differences between the determinations from available measurements. This has notably prevented current models from fully constraining the oxygen flux flowing into Titan's atmosphere. In this work, we aim to understand the differences between the H_2O mole fractions estimated from Herschel and Cassini/CIRS observations. This is done by (re)analysing disc-averaged observations from both instruments using an identical retrieval scheme. Previous differences in modelling/retrieval methods, along with differing viewing geometries between the two datasets are in this way mainly avoided. The whole methodology will be presented and the comparison between the two sets of H_2O mole fractions will be discussed.

1. Introduction and objectives

The discovery of carbon dioxide (CO_2) in Titan's atmosphere by Voyager [6] more than 30 years ago demonstrated the presence of oxygen compounds in its atmosphere. The CO_2 retrieved abundance also suggested the presence of stratospheric H_2O as the required source of oxygen, in the form of hydroxyl (OH) radicals. This presence was confirmed 15 years later with observations from the Infrared Space Observatory (ISO) [2], and is the result of external sources of oxygen, which can take different forms and are difficult to disentangle (e.g., [3]). ISO observations were modeled using an uniform H_2O mixing ratio of 0.4 ppb. This first detection was then followed by measurements from the Herschel Space Telescope [5], taken by the Photodetector Array Camera and Spectrometer (PACS) and the Heterodyne Instrument for the Far-Infrared (HIFI), and by the Composite Infrared Spectrometer (CIRS) onboard the NASA Cassini spacecraft [1]. These observations revealed that the H_2O mole fraction increases with the altitude, which is consistent with a high altitude source and a low-level sink (condensation and photolysis). However, the H_2O mole fraction in Titan's stratosphere remains uncertain. More especially, in the low stratosphere, Herschel and CIRS H_2O measurements differ by around a factor of 4. From Herschel observations, [5] retrieved a H_2O vertical profile and estimated the mole fraction at around 0.03 ppb in the low stratosphere, whereas [1] retrieved H_2O mole fractions of 0.13 ppb from Cassini/CIRS measurements. This discrepancy has limited the ability of current models to constrain the flux of oxygen into Titan's atmosphere [3]. Understanding the difference between the H_2O mole fractions measured from Herschel and CIRS is therefore crucial to better constrain the existing photochemical models, and more largely to improve the knowledge of the source and chemistry of oxygen in Titan's atmosphere.

In this work, we analyse recent disc-averaged observations (2013-2015) of the CIRS/Cassini instrument and retrieve new H_2O mole fractions. The use of disc-averaged observations allows an easier comparison with Herschel measurements, which share the same viewing geometry. Besides a difference in observation geometry, the previous studies have also applied distinct retrieval methods and used different a priori information and radiative transfer modelling codes to retrieve H_2O. This work aims at (re)analyzing the CIRS and Herschel datasets with the same retrieval scheme. This is essential to distinguish the potential contribution of modelling/retrieval differences to the discrepancies in the retrieved H_2O abundances from other possible sources.

2. Observations and method

In this work, we analyse four sets of CIRS disc-averaged observations, recorded in the far-infrared range (FP1, 5-695 cm^{-1}) at a spectral resolution of 0.5 cm^{-1} between February 2013 and July 2015. These sets include around 800 spectra each and span sub-spacecraft latitudes from 40.6°S to 47°N. The disk-averaged observations of Herschel recorded by the PACS and HIFI instruments, which were previously examined, are reanalysed (Tables 1 and 2 in [5]). These were mostly recorded in 2010. PACS measurements include the 66.4 µm, 75.4 µm and 108.1 µm lines, whereas HIFI measured the 557 GHz and 1097 GHz lines.

To retrieve H_2O mole fraction, a similar method is applied to both datasets. This includes 3 steps: 1) the retrieval of temperature profile from methane (CH_4) emission lines (Figure 1), 2) the fitting of the spectral continuum by retrieving aerosols profiles and absorption cross-sections, and 3) the retrieval of the H_2O mole fraction (Figure 1). The whole retrieval scheme is performed using the NEMESIS software [4].

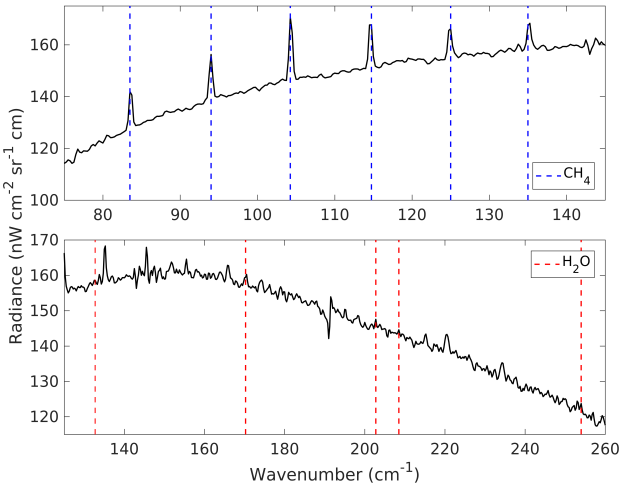

Figure 1: Averaged CIRS spectrum (black) calculated for the set recorded on 21/02/2013. Blue dashed lines are CH_4 emission lines used for the temperature retrieval. Red dashed lines correspond to H_2O lines used for the H_2O mole fraction retrieval.

3. Discussion

In this presentation, we will describe the whole retrieval methodology. A complete error analysis, examining the propagation of different uncertainty sources to the retrieved H_2O mole fraction, has been performed and will be discussed. Thanks to the sub-spacecraft latitudinal spanning of CIRS observations, the possibility of H_2O latitudinal variations will be assessed. Retrievals performed on CIRS and Herschel measurements will be finally compared, and the understanding of potential differences between the two datasets will be particularly targeted.

Acknowledgements

S. Bauduin is supported by the Wiener-Anspach foundation (Belgium).

References

[1] Cottini, V., et al.: Water vapor in Titan's stratosphere from Cassini CIRS far-infrared spectra, Icarus, 220, 855-862, 2012.

[2] Coustenis, A. et al.: Evidence for water vapor in Titan's atmosphere from ISO/SWS data, Astronomy and Astrophysics, 336, L85-L89, 1998.

[3] Dobrijevic, M., et al.: Coupling of oxygen, nitrogen, and hydrocarbon species in the photochemistry of Titan's atmosphere, Icarus, 228, 324-346, 2014.

[4] Irwin, P.G.J., et al.: The NEMESIS planetary atmosphere radiative transfer and retrieval tool, Journal of Quantitative Spectroscopy and Radiative Transfer, 109, 1136-1150, 2008.

[5] Moreno, R., et al.: The abundance, vertical distribution and origin of H_2O in Titan's atmosphere: Herschel observations and photochemical modelling, Icarus, 221, 753-767, 2012.

[6] Samuelson, R.E., et al.: CO_2 on Titan, Journal of Geophysical Research, 88, 8709-8715, 1983.

EPSC Abstracts
Vol. 11, EPSC2017-222, 2017
European Planetary Science Congress 2017

Titan's ionosphere: a survey of solar EUV influences

O. Shebanits (1,2), E. Vigren (1), J.-E. Wahlund (1), M.K.G. Holmberg (3,4), M. Morooka (1), N.J.T. Edberg (1), K.E. Mandt (5,6), J.H. Waite Jr (6)

(1) Swedish Institute of Space Physics, Uppsala, Sweden.

(2) Department of Physics and Astronomy, Uppsala University, Uppsala, Sweden.

(3) Université de Toulouse, UPS-OMP, IRAP, Toulouse, France

(4) CNRS, IRAP, Toulouse, France

(5) Department of Physics and Astronomy, University of Texas at San Antonio, San Antonio, Texas, USA.

(6) Space Science and Engineering Division, Southwest Research Institute, San Antonio, Texas, USA.

Corresponding author: Oleg Shebanits (oleg.shebanits@irfu.se)

Abstract

We present a study of the effects of solar EUV on positive ions and heavy negative charge carriers in Titan's ionosphere, including 78 flybys below 1400 km altitude between TA (Oct 2004) and T120 (June 2016). Statistically significant variations with respect to the solar EUV flux are seen in the RPWS/LP-measured ion charge densities (normalized by the solar zenith angle). From solar minimum to maximum: dayside – a factor ~2 increase, nightside – a factor ~3-4 *decrease*. The overall EUV trends suggest that the idealized Chapman theory does not apply below at least 1200 km in Titan's ionosphere. Nightside charge densities also vary along Titan's orbit, being higher in the sunward magnetosphere of Saturn compared to the magnetotail.

1. Introduction

Titan is the largest moon of Saturn, hosting a fully developed atmosphere extending to almost a whole radius above its surface [1]–[3], [4 and references therein]. Dayside atmosphere is ionized mainly by the solar EUV with ionization peak at ~1100 km altitude [5]–[8]. Nightside at altitudes below 1200 km is mainly ionized by the energetic particle flux from the Kronian magnetosphere [9]–[11]. *In-situ* observations of deep ionosphere (880 – 1000 km altitudes) have revealed negatively charged ions/dust particles (~5 nm) [12] with charge densities ≳ free electrons [7], [13], [14]. With accumulation of data by the Cassini s/c spanning over one solar cycle, the influence of the latter on Titan's ionosphere is under scientific scrutiny: solar maximum enhancement of the electron [15] and the lighter (<100 amu) positive ion number densities [16] have been shown. In this study we extend the picture with the ion population, adding the heavier positive ions and the negative ions/dust grains from the *in situ* measurements by the Radio and Plasma Wave Science (RPWS) Langmuir probe (LP) on board the Cassini s/c.

2. Results and conclusions

The solar EUV flux has a strong impact on the ion and dust grain charge densities: a factor ~2 correlation on the dayside and a factor ~3-4 anti-correlation on the nightside (from min. to max. flux, see Figure 1). During the maximum solar activity the altitudes of the peak charge densities decrease for the positive ions and increases for the negative ions/dust grains, reflecting changes of chemical production. We conclude that a higher solar EUV flux changes the photochemistry of the upper atmosphere (leading to the observation of less ions on the nightside than at a lower EUV flux) and may then have implications for

the aerosol production below the altitudes reachable by the Cassini s/c.

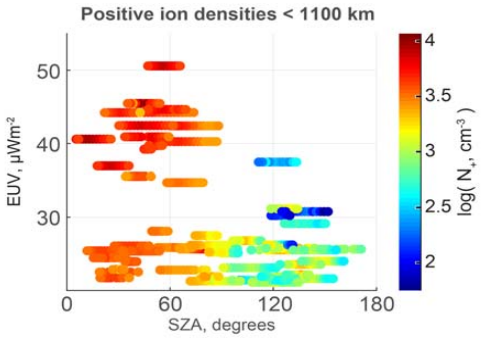

Figure 1. The positive ion number density (color-coded, log scale), plotted in EUV flux (<80 nm, integrated) vs solar zenith angle (SZA), showing the difference in the EUV dependencies on the dayside (SZA<70) and the nightside (SZA>110).

The nightside ion charge densities at ~1000 km altitude is shown to vary along the Titan's orbit, being higher in the sunward magnetosphere than in the magnetotail, consistent with enhanced particle flux intensity from the magnetotail towards sunward magnetosphere, detected by the ENA instrument [17]. The altitude of these variations is in agreement with the peak ionization by the magnetospheric particle precipitation [4], [11].

Acknowledgements

The authors acknowledge funding and RPWS/LP instrument support by the Swedish National Space Board, and the Cassini project support by NASA.

OS acknowledges funding from SNSB, Dnr 130/11:2. EV acknowledges funding by the Swedish National Space Board under contract Dnr 166/14. MKGH acknowledges the funding from CNRS. NJTE acknowledges funding by the SNSB under contract Dnr 135/13 and by VR under contract 621-2013- 4191. KEM acknowledges support from NASA grant NNX13AQ99G.

The authors thank the teams of the TIMED/SEE and SORCE/SOLSTICE instruments for providing the solar irradiance data, available at http://lasp.colorado.edu/lisird/see/level3/3_ssi_ts.html and http://lasp.colorado.edu/lisird/sorce/sorce_ssi/ts.html, respectively.

References

[1] H. B. Niemann, S. K. Atreya, S. J. Bauer, G. R. Carignan, J. E. Demick, R. L. Frost, D. Gautier, J. A. Haberman, D. N. Harpold, D. M. Hunten, G. Israel, J. I. Lunine, W. T. Kasprzak, T. C. Owen, M. Paulkovich, F. Raulin, E. Raaen, and S. H. Way, "The abundances of constituents of Titan's atmosphere from the GCMS instrument on the Huygens probe," *Nature*, vol. 438, no. 7069, pp. 779–784, Dec. 2005.

[2] J.-E. Wahlund, "Cassini Measurements of Cold Plasma in the Ionosphere of Titan," *Science (80-.).*, vol. 308, no. 5724, pp. 986–989, May 2005.

[3] N. J. T. Edberg, J.-E. Wahlund, K. Ågren, M. W. Morooka, R. Modolo, C. Bertucci, and M. K. Dougherty, "Electron density and temperature measurements in the cold plasma environment of Titan: Implications for atmospheric escape," *Geophys. Res. Lett.*, vol. 37, no. 20, p. n/a-n/a, Oct. 2010.

[4] M. Galand, A. J. Coates, T. E. Cravens, and J.-E. Wahlund, "Titan's ionosphere," in *Titan*, I. Muller-Wodarg, C. A. Griffith, E. Lellouch, and T. E. Cravens, Eds. Cambridge: Cambridge University Press, 2014, pp. 376–418.

[5] K. Ågren, J. E. Wahlund, P. Garnier, R. Modolo, J. Cui, M. Galand, and I. Müller-Wodarg, "On the ionospheric structure of Titan," *Planet. Space Sci.*, vol. 57, no. 14–15, pp. 1821–1827, Dec. 2009.

[6] T. E. Cravens, I. P. Robertson, J. H. Waite, R. V. Yelle, W. T. Kasprzak, C. N. Keller, S. A. Ledvina, H. B. Niemann, J. G. Luhmann, R. L. McNutt, W.-H. Ip, V. De La Haye, I. Mueller-Wodarg, J.-E. Wahlund, V. G. Anicich, and V. Vuitton, "Composition of Titan's ionosphere," *Geophys. Res. Lett.*, vol. 33, no. 7, p. L07105, 2006.

[7] O. Shebanits, J.-E. Wahlund, K. Mandt, K. Ågren, N. J. T. Edberg, and J. H. Waite, "Negative ion densities in the ionosphere of Titan–Cassini RPWS/LP results," *Planet. Space Sci.*, vol. 84, pp. 153–162, Aug. 2013.

[8] E. Vigren, M. Galand, O. Shebanits, J.-E. Wahlund, W. D. Geppert, P. Lavvas, V. Vuitton, and R. V Yelle, "Increasing positive ion number densities below the peak of ion-electron pair production in Titan's ionosphere," *Astrophys. J.*, vol. 786, no. 1, p. 69, May 2014.

[9] K. Ågren, J.-E. Wahlund, R. Modolo, D. Lummerzheim, M. Galand, I. Müller-Wodarg, P. Canu, W. S. Kurth, T. E. Cravens, R. V. Yelle, J. H. Waite, A. J. Coates, G. R. Lewis, D. T. Young, C. Bertucci, and M. K. Dougherty, "On magnetospheric electron impact ionisation and dynamics in Titan's ram-side and polar ionosphere–a Cassini case study," *Ann. Geophys.*, vol. 25, no. 11, pp. 2359–2369, 2007.

[10] T. E. Cravens, I. P. Robertson, J. H. Waite Jr., R. V. Yelle, V. Vuitton, A. J. Coates, J.-E. Wahlund, K. Ågren, M. S. Richard, V. De La Haye, A. Wellbrock, and F. M. Neubauer, "Model-data comparisons for Titan's nightside ionosphere," *Icarus*, vol. 199, no. 1, pp. 174–188, Jan. 2009.

[11] T. E. Cravens, I. P. Robertson, S. A. Ledvina, D. Mitchell, S. M. Krimigis, and J. H. Waite, "Energetic ion precipitation at Titan," *Geophys. Res. Lett.*, vol. 35, no. 3, p. L03103, Feb. 2008.

[12] A. J. Coates, F. J. Crary, G. R. Lewis, D. T. Young, J. H. Waite, and E. C. Sittler, "Discovery of heavy negative ions in Titan's ionosphere," *Geophys. Res. Lett.*, vol. 34, no. 22, p. L22103, Nov. 2007.

[13] O. Shebanits, J.-E. Wahlund, N. J. T. Edberg, F. J. Crary, A. Wellbrock, D. J. Andrews, E. Vigren, R. T. Desai, A. J. Coates, K. E. Mandt, and J. H. Waite, "Ion and aerosol precursor densities in Titan's ionosphere: A multi-instrument case study," *J. Geophys. Res. Sp. Phys.*, vol. 121, no. 10, p. 10,075-10,090, Oct. 2016.

[14] K. Ågren, N. J. T. Edberg, and J.-E. Wahlund, "Detection of negative ions in the deep ionosphere of Titan during the Cassini T70 flyby," *Geophys. Res. Lett.*, vol. 39, no. 10, p. n/a-n/a, May 2012.

[15] N. J. T. Edberg, D. J. Andrews, O. Shebanits, K. Ågren, J.-E. Wahlund, H. J. Opgenoorth, T. E. Cravens, and Z. Girazian, "Solar cycle modulation of Titan's ionosphere," *J. Geophys. Res. Sp. Phys.*, vol. 118, no. 8, pp. 5255–5264, Aug. 2013.

[16] H. Madanian, T. E. Cravens, M. S. Richard, J. H. Waite, N. J. T. Edberg, J. H. Westlake, and J.-E. Wahlund, "Solar cycle variations in ion composition in the dayside ionosphere of Titan," *J. Geophys. Res. Sp. Phys.*, pp. 1–9, 2016.

[17] D. G. Mitchell, S. M. Krimigis, C. Paranicas, P. C. Brandt, J. F. Carbary, E. C. Roelof, W. S. Kurth, D. A. Gurnett, J. T. Clarke, J. D. Nichols, J.-C. Gérard, D. C. Grodent, M. K. Dougherty, and W. R. Pryor, "Recurrent energization of plasma in the midnight-to-dawn quadrant of Saturn's magnetosphere, and its relationship to auroral UV and radio emissions," *Planet. Space Sci.*, vol. 57, no. 14–15, pp. 1732–1742, Dec. 2009.

EPSC Abstracts
Vol. 11, EPSC2017-226, 2017
European Planetary Science Congress 2017

Spatial distribution of Neptune's stratospheric temperature obtained with ALMA cycle-0 continuum observation

T. Iino (1), T. Yamada(2) and Y. Tanaka (3)
(1) Tokyo University of Agriculture and Technology, Japan (iino@nagoya-u.jp) (2) Tokyo Institute of Technology, (3) Kagoshima University, Japan

Abstract

Neptune's stratospheric temperature map has shown the presence of relatively warm south polar region whereas the origin and driving mechanism is veiled in mystery. Since the observed pressure region varies with respect to the observation wavelength, multi-wavelengh observation of the continuum emission is useful for the derivation of three-dimensional atmospheric structure. A high spatial resolution observation of 17.6 and 18.7 μm wavelength performed with Very Large Telescope (VLT) in 2006 reported that 100 mbar pressure region on Neptune's south pole is $\sim$10 K warmer than 40 - 60S region (Orton et al. 2007). To obtain the three dimensional structure of warm south south polar region, we analysed the archival data of ALMA (2011.0.00747.S) observed in 2012 as a flux calibration. Deeper stratosphere as 1000 - 500 mbar pressure region than the previous mid-IR observation was observed. The obtained temperature variation with modeled result was within $\pm$ 5K, smaller than that of measured at 100 mbar region. This result represent the relatively flat temperature variation at just above the tropopause, and the previously detected temperature perturbation may be resulted in stratospheric physical and chemical events.

1. Observation and analysis

Neptune's stratospheric atmospheric structure is characterized by warm region on southern mid-latitude region and south pole. In particular, excess of atmospheric temperature measured at south polar warm region was $\sim$10 K in 100 mbar pressure region (Orton et al. 2007). To constrain the origin and the driving mechanism of the region, observational illustration of three-dimensional structure of the region is useful.

We analysed an archival data of ALMA (2011.0.00747.S) that contains Neptune observation as a flux calibration. Observation was performed in 28 August 2012, and spatial resolution was high as 0.35 $\times$ 0.25 arcsec. Center frequencies of each spectral windows were 643 to 648 GHz. A continuum emission map was produced with multi frequency synthesis method that achieves high S/N using all the spectral windows. Figure 1 shows a produced continuum emission map in false color.

From the radiative transfer analysis of Collision Induced Absorption, we estimated that the observed frequency has sensitivity peak at 1000 (disk center) to 500 (60 degree emission angle) mbar pressure regions (Iino et al. submitted). This range is deeper than previous mid-IR observation results of 100 mbar (Orton et al. 2007)

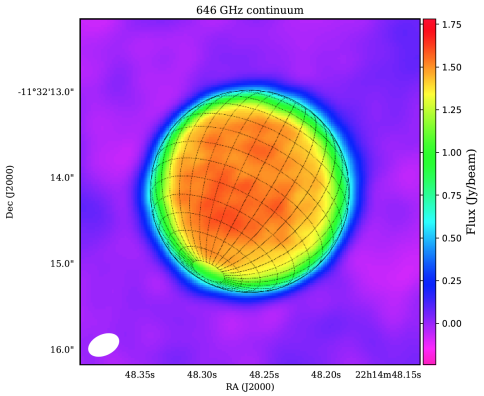

Figure 1: Neptune's 646 GHz continuum map obtained with ALMA in 2012.

2. Discussion

From the initial analysis, observed continuum intensity shows $\pm$5 K agreement with modeled intensity on the entire disk. No clear structure exceeds the random noise level was found on the data. The absence of hot spot may indicate that the hot spot is driven by the

stratospheric perturbation, not the upwelling of warm tropospheric air parcel. However, for the further observational constraint, higher spatial resolution is needed because the beam dilution effect cause decreasing of hot spot intensity. ALMA's high capability possibly achieve the observational needs.

Acknowledgements

This paper makes use of the following ALMA data: ADS/JAO.ALMA#2011.0.00747.S. ALMA is a partnership of ESO (representing its member states), NSF (USA) and NINS (Japan), together with NRC (Canada), NSC and ASIAA (Taiwan), and KASI (Republic of Korea), in cooperation with the Republic of Chile. The Joint ALMA Observatory is operated by ESO, AUI/NRAO and NAOJ. The analysis was supported by Mitaro Namiki of TUAT and Kunihiko Tanaka of Keio University. This work was supported by The Telecommunications Advancement Foundation of Japan, Japan Society for the Promotion of Science, East Asia ALMA Regional Center and ISEE international joint research program.

References

[1] Orton, G. S., Encrenaz, T., Leyrat, C., Puetter, R., Friedson, A. J.: Evidence for methane escape and strong seasonal and dynamical perturbations of Neptune's atmospheric temperatures. Astronomy and Astrophysics, 473(1), L5–L8. 2007

[2] Iino, T., Yamada, T. and Tanaka Y.: A simulation study on terahertz continuum-wave observations of Neptune's atmosphere focusing on future ALMA observation, Submitted to Journal of Remote Sensing Society of Japan, in revision

EPSC Abstracts
Vol. 11, EPSC2017-230, 2017
European Planetary Science Congress 2017

Saturn's Magnetospheric Plasma Flow Encountered by Titan

I. Sillanpää

Finnish Meteorological Institute, Helsinki, Finland
(ilkka.sillanpaa@fmi.fi, twitter: @samooja)

Abstract

Titan has been a major target of the ending Cassini mission to Saturn. 126 flybys have sampled, measured and observed a variety of Titan's features and processes from the surface features to atmospheric composition and upper atmospheric processes. Titan's interaction with the magneto-spheric plasma flow it is mostly embedded in is highly dependent on the characteristics of the ambient plasma. The density, velocity and even the composition of the plasma flow can have great variance from flyby to flyby. The plasma properties have not yet been analyzed for all Titan flybys. Our purpose is the present the plasma flow conditions for all over 70 flybys of which we have Cassini Plasma Spectrometer (CAPS) measurements.

1. Introduction

The plasma flow in the outer parts of Saturn's magnetosphere is very variable in density (up to two orders of magnitude), velocity (in both speed and direction), and composition (the oxygen or water ion content can very from none existent to dominating the plasma pressure and possibly even the number density). This has been demonstrated in previous studies, e.g. [1].

Westlake et al. and Bell et al. [2, 3] have simulated the drastic effects of changing plasma flow conditions to the temperature of Titan's upper atmosphere and the density variations there.

There have been previous studies of the magnetic environment [4] and the ambient electron fluxes [5] but the main plasma parameters such as ion density, total pressure, plasma velocity and composition have not been collected to statistically analyze the environment Titan is embedded in.

FINNISH METEOROLOGICAL INSTITUTE

Sillanpää et al. [6] showed the importance of even a small oxygen ion contribution to the overall interaction between Titan's atmosphere and the ambient plasma. Our plan is collect and analyze the statistics of the plasma conditions encounter by Titan.

2. Analyzing plasma flow conditions

Cassini has been orbiting Saturn since 2004 and has had a total of 126 flybys of Titan. The Cassini mission will end in September 2017 when it will be directed to Saturn atmosphere. Cassini Plasma Spectrometer and its IMS instrument have provided important ion measurement from the flybys. There developed a short circuit in CAPS in the summer of 2011, after which no further Titan flyby measurements were obtained by CAPS. However, there are the results of over 70 flybys that will be analyzed in the planned study.

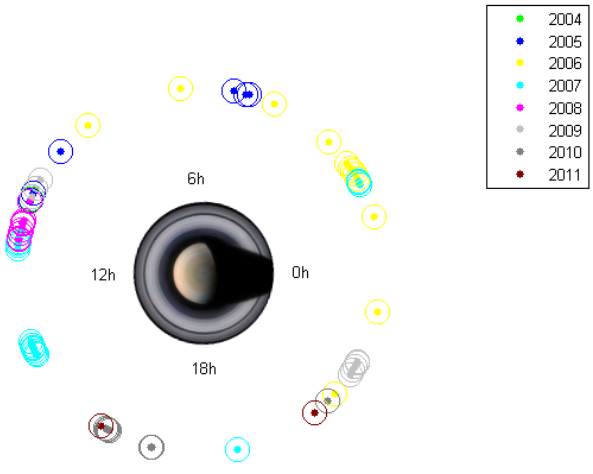

Figure 1: The relative locations of Cassini's Titan flybys, which have CAPS measurements available. Titan's orbit is about 20 Saturn radii from Saturn.

The importance of providing the plasma conditions for each flyby has been demonstrated by the numerous case studies that have been made with limited number plasma conditions around Titan analyzed. Such a data set combined with the numerical simulations of Titan's interaction (such as [7,8]) we believe that an accurate estimate of the total plasma outflow from Titan over Cassini's mission can be obtained.

References

[1] Thomsen, M.F., Reisenfeld, D.B., Delapp, D.M., Tokar, R.L., Young, D.T., Crary, F.J., Sittler, E.C., McGraw, M.A., and Williams, J.D., Survey of ion plasma parameters in Saturn's magnetosphere, J. Geophys. Res., 115, A10220, doi:10.1029/2010JA015267, 2010

[2] Westlake, J., Bell, J.M., Waite, J.H., Johnson, R.E., Luhmann, J.G., Mandt, K.E., Magee B.A., and Rymer, A.M.: Titan's thermospheric response to various plasma environments, J. Geophys. Res., 116(A3), doi:10.1029/ 2010JA016251, 2011.

[3] Bell, J., Westlake, J., and Waite, J.H.: Simulating the time-dependent response of Titan's upper atmosphere to periods of magnetospheric forcing, Geophysical Res. Lett., 38(6), doi:10.1029/2010GL046420, 2011.

[4] Simon, S., Wennmacher, A., Neubauer, F.M., Bertucci, C.L., Kriegel, H., Saur, J., Russell, C.T., and Dougherty, M.K.: Titan's highly dynamic magnetic environment: A systematic survey of Cassini magnetometer observations from flybys TA – T62, Plan. Space Sci., 58(10), doi:10.1016/j.pss.2010.04.021, 2010.

[5] Rymer, A.M., Smith, H.T., Wellbrock, A., Coates, A.J., and Young, D.T., Discrete classification and electron energy spectra of Titan's varied magnetospheric environment, Geophys. Res. Lett., 36, L15109, doi:10.1029/2009GL039427, 2009.

[6] Sillanpää, I., Young, D.T., Crary, F., Thomsen, M., Reisenfeld, D., Wahlund, J-E., Bertucci, C., Kallio, E., Jarvinen, R., and Janhunen, P., Cassini Plasma Spectrometer and Hybrid Model Study on Titan's Interaction: Effect of Oxygen Ions, J. Geophys. Res., 116, doi:10.1029/2011JA016443, 2011.

[7] Sillanpää, I., and Johnson, R.E., The Role of Ion-Neutral Collisions in Titan's Magnetospheric Interaction, Planetary and Space Science 108, doi:10.1016/ j.pss.2015.01.007, 2015.

[8] Sillanpää, I., Kallio, E., Janhunen, P., Schmidt, W., Harri, A.-M., Mäkinen, T., Mursula, K., Vilppola, J., and Tanskanen, P., Hybrid Simulation Study of Ion Escape at Titan for Different Orbital Positions, Advances in Space Research 38, p. 799 – 805, 2006.

EPSC Abstracts
Vol. 11, EPSC2017-242-1, 2017
European Planetary Science Congress 2017

Tidal deformation of Enceladus: variable ice shell thickness

M. Běhounková (1), O. Souček (1), O. Čadek (1), J. Hron (1), G. Tobie (2) and G. Choblet (2)
(1) Charles University, Prague, Czech Republic, (2) Laboratoire de Planétologie et Géodynamique, UMR-CNRS 6112, Université de Nantes, France (behounek@karel.troja.mff.cuni.cz)

Abstract

Recent models of Enceladus's interior structure hint at large thickness variations of the ice shell. Here, we investigate the impact of such variations on tidally-induced deformation and stress by means of numerical simulations. We also address a possible scaling of deformation and stress for traditionally used models assuming constant ice shell thickness.

1. Introduction

Joint analysis of Enceladus's low-degree gravity field [1], libration [2] and topography [3] have shown that the Enceladus's ice shell is thin (average thickness $18-26$km) with possibly large thickness variations. Čadek et al. [4] predict the ice shell thickness increasing from few kilometers beneath the south pole to more than 30km in the equatorial area. Such a large thickness variations are expected to influence the response of the ice shell to the tidal forcing. Studies of tidal deformation reflecting non-spherical shape of bodies are nevertheless rather rare [5]. Traditionally used tools and models investigating the tidally induced deformation and stress are usually based on a spectral approach and require spherical bodies with radially dependent material properties. Incorporation of variation of the shell thickness in these models is difficult. For deformation in bodies with an irregular non-spherical shape, an usual choice is to employ a finite element method. Following Souček et al. [6], we have therefore developed a three-dimensional finite element method using FEniCs package [7] which allows to assess the influence of the ice shell thickness variations on the viscoelastic tidal deformation.

2. Model and method

In order to evaluate stress and deformation due to tides, we take into account following equations for a pre-stressed viscoelastic (Maxwell) body:

$$\nabla \cdot \sigma = -\rho \nabla V$$

$$\sigma = \frac{2G(1+\nu)}{3(1-2\nu)} (\nabla \cdot \mathbf{u}) \mathbf{I} + G \left[\nabla \mathbf{u} + (\nabla \mathbf{u})^\tau - \frac{2}{3} (\nabla \cdot \mathbf{u}) \mathbf{I} \right] - G \int_0^t \frac{\sigma^\delta(t')}{\eta} \mathrm{d}t',$$

where V is the tidal potential, $\mathbf{u}$ is the displacement, σ is the incremental Cauchy stress tensor and σ^δ is its deviatoric part. ρ is the ice density, G, ν and η denotes the shear modulus, the Poisson ratio and the viscosity, respectively. The corresponding boundary conditions read

$$\sigma \cdot \mathbf{n} + u_\mathrm{r} \rho g \mathbf{n} = \mathbf{0} \quad \text{at surface}$$
$$\sigma \cdot \mathbf{n} - u_\mathrm{r} (\rho_\mathrm{w} - \rho) g \mathbf{n} = -\rho_\mathrm{w} V \mathbf{n} \quad \text{at bottom,}$$

$\mathbf{n}$ is the normal to the boundary, u_r the radial displacement, $\mathbf{g}$ the gravitational acceleration and ρ_w is the water density.

The tidal (loading) potential for a body on an eccentric synchronous orbit is described by the following expression [8]

$$V = r^2 \omega^2 e \left(-\frac{3}{2} P_{20}(\cos\vartheta) \cos\omega t + \frac{1}{4} P_{22}(\cos\vartheta) \left(3\cos\omega t \cos 2\varphi + 4 \sin\omega t \sin 2\varphi\right) \right),$$

where t is the time, ω is the angular velocity and e is the eccentricity; P_{jm} are the associated Legendre functions for degree j and order m.

The numerical solution of the governing equations is obtained using FEniCS package (http://fenicsproject.org) [7].

3. Stress and deformation

An example depicting the effect of the ice shell thickness on the tidal deformation and the stress is shown in Fig. 1. Compared to model with the uniform ice shell thickness (25km, model U), the stress is enhanced 6 times in the model with the realistic ice shell thinning (model C) whereas the radial displacement increases only by less than 50%. We also found that the enhancement is degree and order dependent: the potential Love number increases from $k_{2m} = 0.014$ for model U to $k_{20} = 0.017$ and $k_{22} = 0.021$ for model C. The deformation and the additional potential for order $m = 2$ is therefore more enhanced than the order $m = 0$ due to the shell geometry. In the case of model C, the deformation corresponding to the higher degrees ($j = 3-4$) is non-zero with amplitude less than 1% compared to deformation at degree $j = 2$.

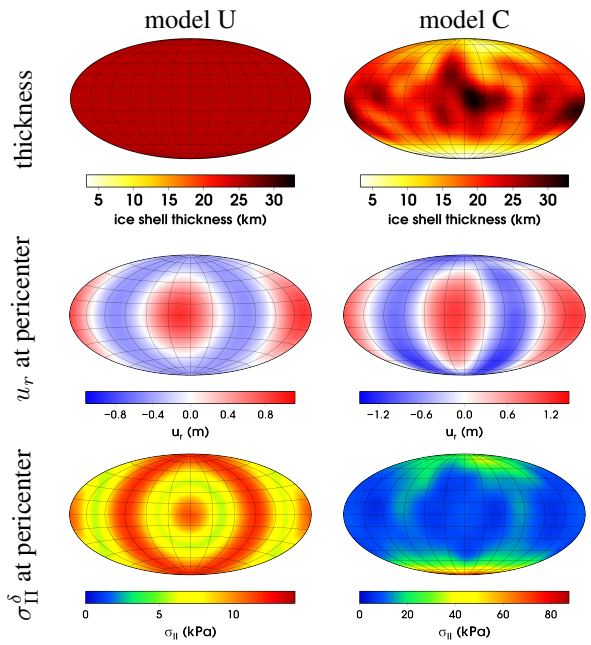

Figure 1: Comparison of displacement and stress at pericenter, models U (uniform thickness, 25km) and model C (based on Čadek et al. [4]), viscosity 10^{14}Pas.

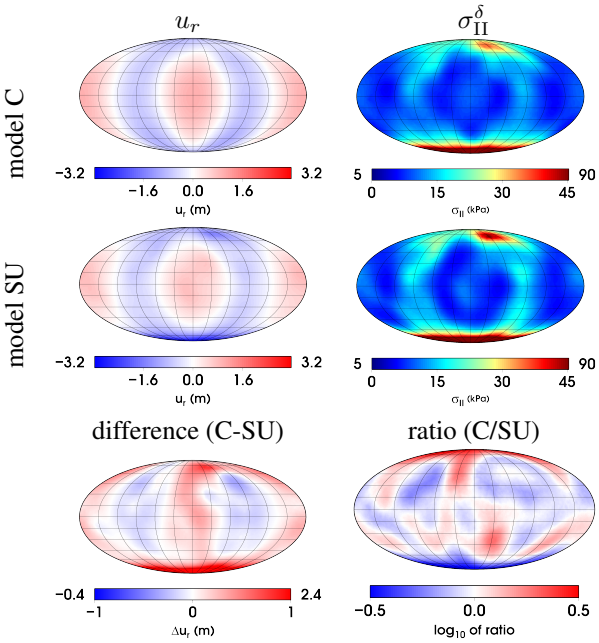

Figure 2: Evaluation of the proposed scaling for displacement and stress, model C and model SU (scaled variables based on model U), elastic body.

4. Scaling

In the case of elastic model, we have addressed the accuracy of the scaling proposed by Turcotte et al. [9]. We have therefore scaled the displacement and stress obtained for the model with the uniform ice shell thickness (model U) by the local ice shell thickness D, i.e. we assume that both radial displacement and stress scales with the factor $25\mathrm{km}/D$. The proposed scaling overestimates both the displacement and the stress magnitude in the southern polar region by the factor ~ 3 (see Fig. 2). Our results therefore suggest necessity to employ fully 3D approach for quantitative assessment of the effects of the thickness variations. The failure of the scaling is probably mainly due to long-wavelength character of the loading which is in breach of the assumptions required for the scaling.

5. Summary and Conclusions

The variable ice shell thickness influences both the magnitude and the pattern of stress and deformation. In the case of the realistic ice shell thickness, the deformation enhancement is degree and order dependent. However, we did not find an appropriate scaling.

Acknowledgements

This research received funding from the Czech Science Foundation (project No. 15-14263Y) and was also supported by the IT4Innovations Centre of Excellence project (CZ.1.05/1.1.00/02.0070).

References

[1] Iess, L., et al. (2014), Science, 344, 78–80.

[2] Thomas, P. C. et al. (2016), Icarus, 264, 37–47.

[3] Nimmo, F. et al. (2011), J. Geophys. Res., 116, E11001.

[4] Čadek, O. et al. (2016), Geophys. Res. Let. 46, 5653–5660.

[5] Geruo, A. et al. (2014), J. Geophys. Res.-Planets 119, 659–678.

[6] Souček, O. et al. (2016), Geophys. Res. Let. 43, 7417–7423.

[7] Alnaes, M. S et al. (2015), The FEniCS project version 1.5, Arch. Numer. Software, 3(100).

[8] Kaula, W. M. (1964) Reviews of Geophysics 2, pp. 661–685.

[9] Turcotte, D.L. et al. (1981), J. Geophys. Res. 86, 3951–3959.

EPSC Abstracts
Vol. 11, EPSC2017-244-1, 2017
European Planetary Science Congress 2017

Evolution of Saturn's mid-sized icy moons

M. Neveu (1,2), A. R. Rhoden (2)
(1) NASA HQ / USRA, Washington, DC, USA, (2) Arizona State University, Tempe, AZ, USA (marc.f.neveu@nasa.gov)

Abstract

We aim to reproduce the orbits (semi-major axes a and eccentricities e) and interiors (core radii, oceans) of the mid-sized moons of Saturn (Mimas, Enceladus, Tethys, Dione, and Rhea) as constrained by *Cassini* data. We numerically model the coupled geophysical and orbital evolution, assuming the moons formed late from Saturn's rings [1]. This closely reproduces observations, but only if Enceladus is initially warmer than its accretional heat budget. Notably, our models reconcile the moons' dynamical youth and geological diversity. We discuss next steps for these models.

1. Observational Constraints

Each moon's orbit changes due to tidal dissipation inside this moon and Saturn, and interaction with the rings and with other moons, which we model as in [1]. Beyond the zone of ring-moon interaction [1], a chiefly increases due to tides raised on Saturn: $\frac{da}{dt} \propto \frac{k_2}{Q}\, a^{-5.5}$, with k_2 and Q Saturn's surface degree-2 tidal potential Love number and bulk tidal quality factor, constrained by astrometry [2]. A constant Q yields moon ages (times at which $a <$ Saturn's Roche radius) much younger than the solar system's, but compatible with cratering from planetocentric impactors [3].

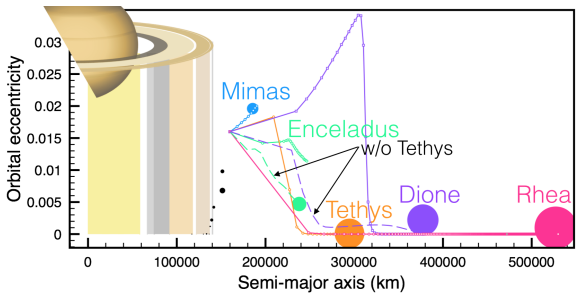

Figure 1: Orbital evolution of Saturn's mid-sized moons. Filled circles are present-day orbital a and e; curves are computed (a;e) over time, with overlapping dots showing positions every 10 million years.

Gravity and libration data suggest cores of density ≈2.4 g cm^{-3} for Enceladus [4], Dione [4], Rhea [5], and maybe even Mimas [6]. This implies high porosity over the already low density of hydrated rock (≈2.9 g cm^{-3}), likely filled with ice and/or liquid water. A density of 2.4 g cm^{-3} is obtained with 25 vol.% ice and 75 vol.% rock (assumed hydrated inside progenitor moons). This is consistent with rock seeds accreting in ice-rich rings between the Roche radii for rock and ice [1], while avoiding disruption because rock retains its cohesion (rock grains remain in contact) as long as the mixture contains ≤30-40% ice [7].

2. Model Scenarios & Results

We use the *IcyDwarf* code [8], upgraded to model all 5 moons simultaneously, with moon-moon and moon-ring interactions. We assume differentiated accretion [1] into a rocky core with 25 vol.% ice and an icy shell. Based on the a and e of Saturn's moonlets (black dots in Fig. 1), we assume that by the time the moons finish accreting, they have orbits with a≈160000 km and e≥0.01. We pick a starting e=0.016, 20 vol.% bulk porosity (which can compact over time), and uniform temperature T of 100 K, 30 K higher than current effective surface T to account for accretional heating. Starting masses and bulk densities (radii) are chosen to match today's values after compaction, if any. Moon masses and Saturn's Q are fixed. The time of formation of each moon is determined from k_2/Q; the ring mass (assumed to be 7×10^{19} kg today) is initially augmented by those of the moons, and decreases accordingly each time a moon forms.

Results show that the older and larger cores of Rhea and Dione (and to some extent Tethys) are radiogenically heated (Fig. 2). This decreases the ice viscosity, increases tidal dissipation, and thus decreases their eccentricity (Fig. 1). In contrast, younger Mimas stays cold and its e keeps increasing. Moon-moon resonances too can increase e, as shown for Tethys-Dione and Tethys-Enceladus in Fig. 1. Present-day orbits and interiors are matched (Fig. 2), assuming heating 2-3× over Andrade levels of dissipation [8], except that:

A. Radiogenic heating cannot warm Enceladus enough to damp its initial e to today's 0.0047. Damping requires a starting T=200 K (case shown in Fig. 1 & 2), i.e. heating by an impactor of radius 100 km at 810 m/s (planetocentric e=0.05), or 67 km at 1.7 km/s (e=0.1). Such energies are $>5\times$ higher than needed to make a South Polar Terrain (SPT)-sized crater [10]. Still, giant impacts, which likely conclude moon accretion [1] and may have left craters on all 5 moons (Herschel, possibly the SPT [9], Odysseus, Evander, and Tirawa/Mamaldi), would have heated Enceladus' ice the most, because Enceladus has the highest ratio of crater (SPT) size to mass of ice. Warmer interiors are also caused by higher initial e, which damp faster.

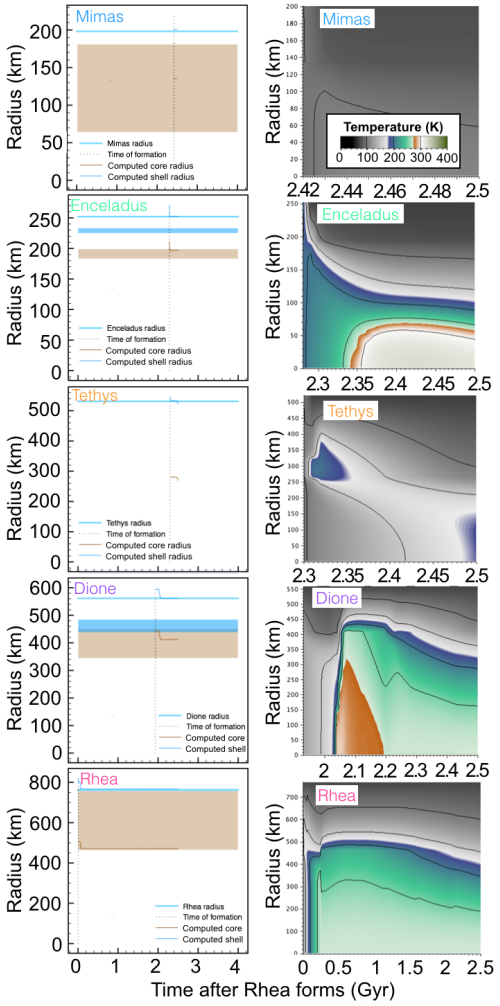

Figure 2: Left: Moon structures. Shaded are *Cassini* constraints on core (brown) and, if relevant, ocean outer radii (blue). Thick lines: moon radii. Thin lines: computed core and moon radii. Right: T over time.

B. The runs do not produce oceans on Enceladus and Dione, although they do produce liquid water in Enceladus' core today and in Dione's core in the past.

We have assumed a constant Q, and that k_2=1.5, the value for a homogeneous fluid, not 0.39 as observed [2], which yields spuriously young moons (Rhea is 2.5 Gyr old; Fig. 2). We will update runs with Q computed from models of Saturn's interior [11] that vary with frequency, i.e. a and, thus, time. We obtain similar Q to [2, 11] with a core of radius 16000 km and density 18 g cm^{-3}, and an envelope of density 0.32 g cm^{-3}, which also yield correct M and k_2 for Saturn.

References

[1] Charnoz, S. et al.: Accretion of Saturn's mid-sized moons during the viscous spreading of young massive rings: Solving the paradox of silicate-poor rings versus silicate-rich moons, Icarus, Vol. 216, pp. 535-550, 2011.

[2] Lainey, V. et al.: New constraints on Saturn's interior from Cassini astrometric data, Icarus, Vol. 281, pp. 286-296, 2017.

[3] Dones, L. et al.: Icy satellites of Saturn: Impact cratering and age determination. In Saturn from Cassini-Huygens (pp. 613-635). Springer Netherlands, 2009.

[4] Beuthe, M., Rivoldini, A., and Trinh, A.: Enceladus's and Dione's floating ice shells supported by minimum stress isostasy, GRL, Vol. 43, pp. 10088-10096, 2016.

[5] Tortora, P. et al.: Rhea gravity field and interior modeling from *Cassini* data analysis, Icarus, Vol. 264, pp. 264-273, 2016.

[6] Tajeddine, R. et al.: Constraints on Mimas' interior from Cassini ISS libration measurements, Science, Vol. 346, pp. 322-324, 2014.

[7] Bland, M. T. et al.: Composition and structure of the shallow subsurface of Ceres revealed by crater morphology, Nature Geoscience, Vol. 9, pp. 538-542, 2016.

[8] Neveu, M., Rhoden, A. R.: The Origin and Evolution of a Differentiated Mimas, Icarus, in revision.

[9] Tajeddine, R. et al.: True polar wander of Enceladus from topographic data, 48th Division for Planetary Sciences Meeting, 16–21 October, Pasadena, USA, 2016.

[10] Wilhelms, D. E., and Squyres, S. W.: The Martian hemispheric dichotomy may be due to a giant impact, Nature, Vol. 309, pp. 138-140, 1984.

[11] Remus, F., Mathis, S., Zahn, J. P., and Lainey, V.: The surface signature of the tidal dissipation of the core in a two-layer planet, A&A, Vol. 573, p. A23, 2015.

EPSC Abstracts
Vol. 11, EPSC2017-247, 2017
European Planetary Science Congress 2017

Search for evidence of Butane on Titan with new spectroscopic data

A. Jolly (1), Y. Benilan (1), L. Manceron (2)

(1) Laboratoire Interuniversitaire des Systèmes Atmosphériques (LISA), UMR 7583 du CNRS, Universités Paris Diderot et Paris-Est Créteil, Institut Pierre Simon Laplace (IPSL), Créteil, France.
(2) Synchrotron SOLEIL, L'orme des Merisiers, Saint-Aubin-BP 48, 91192 Gif-sur-Yvette Cedex and MONARIS, UMR 8233. Université Pierre et Maris Curie, 4, place Jussieu 75252, France.

1. Introduction

Detecting the presence of large chemical compounds is critical for understanding the photochemistry and dynamics of planetary atmospheres and in particular of Titan's organic rich atmosphere. On Titan, complex photochemical reactions lead to the formation of numerous heavier hydrocarbons, including several hydrocarbons with C_3 and C_4 frameworks.

The Composite InfraRed Spectrometer (CIRS) on-board Cassini has recorded spectra of Titan in the far and mid-infrared since 2004 with a spectral resolution up to 0.5 cm^{-1}. The Cassini mission is ending in September of 2017 and infrared observations from the ground at higher resolution are already planned. In recent years, it is in fact from remote facilities that new detections in Titan's stratosphere were obtained, including HNC (Moreno et al. 2011, using Herschel), C_2H_3CN and C_2H_5CN (Cordiner et al. 2014, 2015, using ALMA).

Yet, photochemical models for Titan, developed since the pioneering work of Yung et al. (1984) and now accounting for ion-neutral reactions (e.g. Yelle et al. 2016, Dobrijevic et al. 2016), indicate that still undetected hydrocarbons are expected to be present and observable in Titan's atmosphere. This is the case, in particular, of butane (C_4H_{10}) which is predicted to be as abundant as propane (C_3H_8), a molecule detected in Titan's atmosphere with CIRS through many vibrational bands (Nixon et al. 2009).

2. Butane

C_4H_{10} is a large molecule with two isomers, isobutane and n-butane, the latter presenting two conformers (trans and gauche). Each species has 36 vibrational modes and most of the bands are very congested. Because of this complexity, there is no plan to try a rotational analysis leading to a classical line list.

Until recently, only low resolution (0.1 cm^{-1}) and room temperature laboratory spectra of isobutane and n-butane were available in the literature. In this study we have recorded absorption cross sections of butane below 200 K to come as close as possible to the atmospheric conditions in Titan's stratosphere. Using the AILES high resolution spectrometer and the Globar light source (see Figure 1), we have recorded for the first time n-butane spectra at temperature as low as 150 K. We have observed very important variations with the temperature, in particular due to the varying relative abundance of the trans and gauche conformers. Most spectra were recorded at 0.1 cm^{-1} resolution due to the low luminosity of a Globar light source but one 12 hours' spectra could be recorded at 0.03 cm^{-1} showing very sharp features in particular for the bands centred at 733 and 966 cm^{-1}, as can be seen in figure 1.

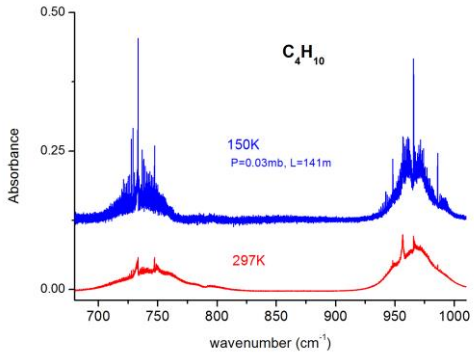

Figure 1: n-butane spectra at room and low temperature.

This means that butane can be searched in CIRS spectra of Titan with good chances due to the increase in the band contrast in low temperature conditions and with even better chances from the ground at higher resolution.

Similar measurements with the other conformer of butane, isobutane are planned. The goal is to study the detection possibilities of isobutane at low temperature as well.

References

1. Moreno et al., A&A 536, L12 (2011)
2. Cordiner et al., ApJ 795, L30 (2014);
3. Cordiner et al., ApJ 800, L14 (2015)
4. Yung et al., ApJ Suppl. Ser. 55, 465-506 (1984)
5. Yelle et al., Titan Aeronomy & Climate Workshop, Reims, June 27-29 (2016)
6. Dobrijevic et al., Icarus 268, 313-339 (2016)
7. Nixon et al., PSS 57, 1573-1585 (2009)

EPSC Abstracts
Vol. 11, EPSC2017-291, 2017
European Planetary Science Congress 2017

Laboratory studies of organics with Cosmorbitrap, a new HRMS analyser, in the framework of future missions to Titan and other organic worlds

L. Selliez (1, 2), C. Briois (1) and N. Carrasco (2) (laura.selliez@cnrs-orleans.fr)

(1) LPC2E, Orléans, FRANCE, (2) LATMOS, Guyancourt, France

Abstract

In space exploration, searching for organic molecules is strongly related to astrobiology. Their presence and complexity enlighten us about how abiotic processes can sustain prebiotic chemistry and the emergence of life. Mass spectrometry is among the best instrument to detect and to study organic matter and organic-rich environments. We will present a space mass analyzer called Cosmorbitrap, based on the Orbitrap™ technology. This new kind of instrumentation reaches the performances of existing space mass spectrometers and will answer to the challenges raised by the Cassini-Huygens space mission on Titan's organic world.

1. Introduction

The Cassini-Huygens mission has highlighted, among many discoveries, the chemistry occurring in Titan atmosphere detecting positive and negative ions at very high masses [1]. This surprising detection was allowed by the mass spectrometers on board the spacecraft and data collected have increased our knowledge about this moon. The resolution of these same instruments limits the identification of the molecules detected.

1.1 Orbitrap™ technology and Cosmorbitrap

A new generation of mass analyzer is extensively used in laboratory: the Orbitrap™ technology. Based on the use of the electric field, a Fast Fourier Transform (FFT) is applied in order to convert the signal recorded (oscillation frequencies of ions present inside the cell). The commercial instrument enables to reach a mass resolution of 10^6 at m/z=200 ([2], [3]). In collaboration with Alexander Makarov, the inventor of this technology, our consortium of five French CNRS laboratories (LPC2E, LATMOS, LISA, IPAG, CSNSM) is developing a space version of this new generation mass analyzer. This sub system comprises 4 main elements: the Orbitrap™ cell adapted for space, the high stability voltage pulsed power supply, the highly sensitive current pre-amplifier, and the digital electronics for control, data acquisition and FFT processing. This development is called Cosmorbitrap.

1.2 Laboratory prototype

In laboratory, to perform our tests we have coupled the Cosmorbitrap with a Nd-Yag laser at 266 nm (figure 1).

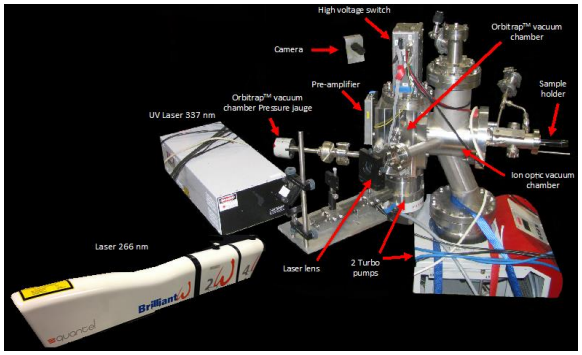

Figure 1: Laboratory prototype at LPC2E.

Results on metals have been reported in Briois et al, 2016 [4]. In this work, the goal is to present results obtained on organics, relevant in the framework of a future space exploration of an organic world like Titan environment.

2. Blind test: identification of unknown organic molecules

During a space mission, we do not know which molecules are going to be detected. For this reason,

and to test the capabilities of our instrument, we performed a blind test on unknown complex organic molecules. A JAXA team sent us two samples to be identified with the Cosmorbitrap. All tests were performed with the Cosmorbitrap. The mass accuracy was a very important parameter to detect the parent peak but also the mass gaps between fragments. Data treatment was done with Attributor, software dedicated to HRMS (developed at IPAG, France). We used different complementary information like the Mass Defect vs Exact Mass diagram (figure 2).

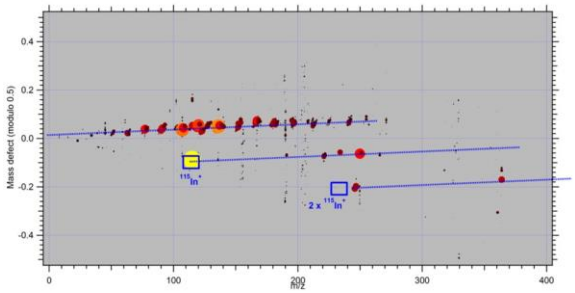

Figure 2: MDVM diagram of sample "A".

The inferred structures were confirmed using the fragmentation patterns compared with the NIST database. We identified the first molecule as HOBt, at m/z 136u and the second as BBOT with m/z 431u. The JAXA team confirmed our results, validating the ability of Cosmorbitrap to identify complex organic molecules.

3. Evolution of the mass resolving power with the background pressure

Pressure is a key parameter in mass spectrometry. A low vacuum pressure is indeed required in the chamber of the analyzer and it determines the performances of the instrument. However pressure depends of the object selected for a future space mission. When the background pressure is as high as in Titan's atmosphere, it is a challenge to deal with a reasonably small vacuum pumping system and a satisfying performance of the instrument to answer the scientific questions raised.

In the context of Titan environment, we characterized the decrease of the Cosmorbitrap optimal performances when increasing the pressure in the trap. We performed this test using 3 different organics. The lowest pressure recorded in the Orbitrap™ chamber is about 10^{-10} mbar. We increased this pressure until 5.10^{-7} mbar. Spectra were recorded at these two pressures and at several intermediate pressures. With these data, we were able to quantify the evolution of the mass resolving power for various organic molecules.

4. Summary and future work

In the context of exploring Titan environment with a future space mission, we have addressed two important questions using Cosmorbitrap. In a first project, we have shown that the instrument was able to identify the structure of complex organic molecules through a blind test jointly organized with JAXA. And in a second project we have characterized the evolution of the instrument performances when increasing the background pressure as it can be critical when exploring Titan's dense atmosphere. A repeatability study is in progress to finalize these projects.

Acknowledgements

We thank all people involved in the development of Cosmorbitrap, more particularly the engineers of LPC2E. We thank the JAXA team and Roland Thissen for their collaboration on the blind test project. Authors gratefully acknowledge the financial support by the French space national agency, the Centre National des Etudes Spatiales (CNES), the Region Centre/Val de Loire, for the funding of L.S. PhD. N. C acknowledges the financial support of the European Research Council (ERC Starting Grant PRIMCHEM, Grant agreement no. 636829).

References

[1] Waite et al, (2007): "The process of tholins formation in Titan's upper atmosphere". Science, 316, 870-875

[2] Makarov, (2000): "Electrostatic axially harmonic orbital trapping: A high-performance technique of mass analysis". Analytical Chemistry, 72, 1156-1162

[3] Denisov et al, (2012): "Orbitrap mass spectrometry with resolving powers above 1,000,000". International Journal of Mass Spectrometry, 325-327, 80-85

[4] Briois et al, (2016): "Orbitrap mass analyzer for in situ characterization of planetary environments: performance evaluation of a laboratory prototype". Planetary and Space Science, vol. 131, 33-45

EPSC Abstracts
Vol. 11, EPSC2017-295-1, 2017
European Planetary Science Congress 2017

High-resolution Global Climate Modeling of Saturn's and Jupiter's tropospheric and stratospheric circulations

A. Spiga[1], S. Guerlet[1], E. Millour[1], Y. Meurdesoif[2], M. Indurain[1], T. Dubos[1], M. Sylvestre[1,3], S. Cabanes[1], A. Boissinot[1], T. Fouchet[3] [aymeric.spiga@upmc.fr] [1] LMD (UPMC/CNRS/X), Paris, France [2] LSCE (CEA), Saclay, France [3] LESIA (UPMC/CNRS), Meudon, France

Background and motivation The longevity of the richly-instrumented Cassini mission permitted an exceptionally detailed characterization, and monitoring over the changing seasons, of Saturn's a) latest Great White Spot[1] and associated stratospheric warming[2,3]; b) mid-latitude convective storms[4] and vortices[5,6]; c) stable hexagonal polar jet[7] and central turbulent polar vortex[8]; d) equatorial stratospheric oscillation of temperature, with jets stacked along the vertical, in Saturn's stratosphere[9] with semi-annual periodicity[10]; e) possible meridional transport of stratospheric hydrocarbons[11,12]. Cassini mapping of Jupiter's and Saturn's banded tropospheric jets in the cloud layer demonstrated the high rate of conversion of energy from eddies to banded jets[13,14] and detailed the structure of macroturbulence and vorticity[15,16], which strongly suggests that large-scale tropospheric banded jets emerge from forcing by smaller-scale eddies and waves arising from hydrodynamical instabilities. This harvest of Cassini observations has been complemented by Earth-based space telescopes[17], which enabled to monitor e.g. Jupiter's "quasi-quadriennal" equatorial oscillation[18]. Inserted in Jupiter's orbit in July 2016, the Juno spacecraft is currently acquiring, for the first time, microwave radiometry maps of water abundance and convective cloud opacity below Jupiter's visible cloud level (in the deep troposphere, at pressures exceeding 100 bars), high-order gravity measurements to infer the depth at which banded jets extend[19], and high-resolution images of Jupiter's Great Red Spot and polar regions. Cassini's Grand Finale in 2017 will also perform the latter two measurements for Saturn.

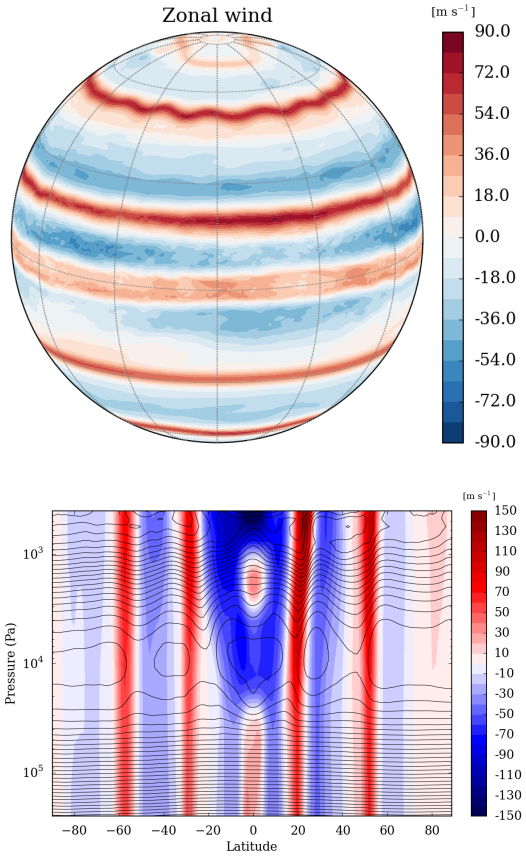

Figure 1: *[Top] Tropospheric 1.5-bar zonal wind obtained in the ninth simulated year ($L_s = 0°$) with our Saturn GCM. [Bottom] Pressure-latitude section of zonal-mean zonal winds for the same season and Saturn GCM simulation, with zonal-mean temperature contours superimposed.*

A new GCM for gas giants To address the new questions raised by those recent measurements, we built a new GCM for gas giants, both versatile and powerful enough to resolve the eddies arising from hydrodynamical instabilities and forcing the planetary-scale jets, to extend from the troposphere to the stratosphere with good enough vertical resolution, and to use optimized radiative transfer to predict seasonal tendencies over decade-long giant planets' years. To that end, we coupled our seasonal radiative model tailored for Saturn[20], and recently adapted to Jupiter as well[21], with DYNAMICO, the next state-of-the-art dynamical core for Earth and planetary climate studies

in our lab, using an original icosahedral mapping of the planetary sphere which ensures excellent conservation and scalability properties in massively parallel resources[22].

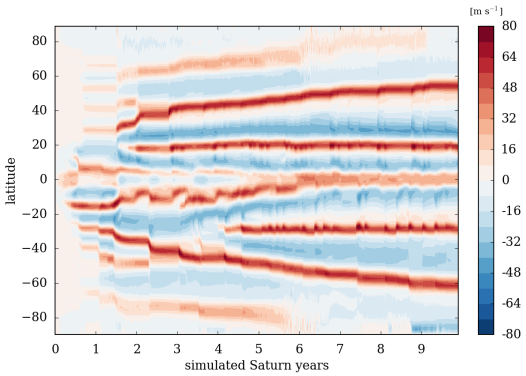

Figure 2: *The evolution of zonal-mean tropospheric zonal jets from our 10-year-long Saturn GCM simulation.*

$1/2°$ Saturn GCM simulations Our GCM simulations for Saturn reproduce tropospheric mid-latitude jets bearing similarities with the observed jet system (numbering, intensity, width, see Figure 1). They also predict eastward-propagating Rossby-gravity (Yanai) waves at the equator, and high-wavenumber waves in mid-latitudes, as well as vortices. In contrast to observations, in our GCM simulations the equatorial jet is only weakly super-rotating and the polar jet is strongly destabilized by meandering. Our model predicts stacked stratospheric eastward and westward jets, but raising the model top is needed to address the equatorial oscillation. We find that jets are eddy-driven with a conversion rate from eddies to mean flow in agreement with Cassini estimates. Before reaching equilibrium, mid-latitude jets experience poleward migration (Figure 2), which can be ascribed to a self-destabilization of the jets by baro-tropic/-clinic instabilities. Our GCM simulations exhibit a stratospheric meridional circulation from one tropic to the other, with seasonal reversal, suggesting dynamical control on the observed variations of hydrocarbons.

Perspectives for Saturn and Jupiter We also carried out 1/4° and 1/8° Saturn GCM simulations with a "test" configuration (sponge layer and high dissipation). The simulated midlatitude jets' strengths are closer to observed values – and a more complete spectrum of eddies, waves, and vortices is resolved. Refining the vertical resolution is also considered as a path forward. Our Saturn GCM is only a first step towards a GCM system able to simulate all giant planet environnements: preliminary Jupiter GCM simulations will be presented to discuss measurements from JUNO and the (future) JUICE missions.

Bibliography

[1] G. Fischer, W. S. Kurth, et al. A giant thunderstorm on Saturn. *Nature*, 475:75–77, 2011.

[2] L. N. Fletcher, B. E. Hesman, et al. The origin and evolution of Saturn's 2011-2012 stratospheric vortex. *Icarus*, 221:560–586, 2012.

[3] T. Fouchet, T. K. Greathouse, et al. Stratospheric aftermath of the 2010 Storm on Saturn as observed by the TEXES instrument. I. Temperature structure. *Icarus*, 277:196–214, 2016.

[4] U. A. Dyudina, A. P. Ingersoll, et al. Lightning storms on Saturn observed by Cassini ISS and RPWS during 2004 2006. *Icarus*, 190:545–555, 2007.

[5] K. M. Sayanagi, U. A. Dyudina, et al. Cassini ISS observation of Saturn's String of Pearls. *Icarus*, 229:170–180, 2014.

[6] Harold Justin Trammell, Liming Li, et al. Vortices in saturn's northern hemisphere (2008–2015) observed by cassini iss. *Journal of Geophysical Research: Planets*, 121(9):1814–1826, 2016. 2016JE005122.

[7] A. Sánchez-Lavega, T. Río-Gaztelurrutia, et al. The long-term steady motion of Saturn's hexagon and the stability of its enclosed jet stream under seasonal changes. *Geophys. Res. Lett.*, 41:1425–1431, 2014.

[8] K. M. Sayanagi, J. J. Blalock, et al. Cassini ISS observation of Saturn's north polar vortex and comparison to the south polar vortex. *Icarus*, 285:68–82, 2017.

[9] T. Fouchet, S. Guerlet, et al. An equatorial oscillation in Saturn's middle atmosphere. *Nature*, 453:200–202, 2008.

[10] S. Guerlet, T. Fouchet, et al. Evolution of the equatorial oscillation in Saturn's stratosphere between 2005 and 2010 from Cassini/CIRS limb data analysis. *Geophys. Res. Lett.*, 38:9201, 2011.

[11] S. Guerlet, T. Fouchet, et al. Vertical and meridional distribution of ethane, acetylene and propane in Saturn's stratosphere from CIRS/Cassini limb observations. *Icarus*, 203:214–232, 2009.

[12] M. Sylvestre, S. Guerlet, et al. Seasonal changes in Saturn's stratosphere inferred from Cassini/CIRS limb observations. *Icarus*, 258:224–238, 2015.

[13] C. Salyk, A. P. Ingersoll, et al. Interaction between eddies and mean flow in Jupiter's atmosphere: Analysis of Cassini imaging data. *Icarus*, 185:430–442, 2006.

[14] A. D. Del Genio, J. M. Barbara, et al. Saturn eddy momentum fluxes and convection: First estimates from Cassini images. *Icarus*, 189:479–492, 2007.

[15] P. L. Read, B. J. Conrath, et al. Mapping potential vorticity dynamics on saturn: Zonal mean circulation from Cassini and Voyager data. *Planetary and Space Science*, 57:1682–1698, 2009.

[16] B. Galperin, R. M. B. Young, et al. Cassini observations reveal a regime of zonostrophic macroturbulence on Jupiter. *Icarus*, 229:295–320, 2014.

[17] L. N. Fletcher, T. K. Greathouse, et al. Mid-infrared mapping of Jupiter's temperatures, aerosol opacity and chemical distributions with IRTF/TEXES. *Icarus*, 278:128–161, November 2016.

[18] T. K. Greathouse, G. S. Orton, et al. Tracking Jupiter's Quasi-Quadrennial Oscillation and Mid-Latitude Zonal Waves with High Spectral Resolution Mid-Infrared Observations. volume 48 of *AAS/Division for Planetary Sciences Meeting Abstracts*, page 501.05, October 2016.

[19] Y. Kaspi. Inferring the depth of the zonal jets on Jupiter and Saturn from odd gravity harmonics. *Geophysical Research Letters*, 40:676–680, 2013.

[20] S. Guerlet, A. Spiga, et al. Global climate modeling of Saturn's atmosphere. Part I: Evaluation of the radiative transfer model. *Icarus*, 238:110–124, 2014.

[21] S. Guerlet and A. Spiga. Radiative and dynamical modeling of Jupiter's atmosphere. volume 18 of *EGU General Assembly Conference Abstracts*, page 9990, April 2016.

[22] T. Dubos, S. Dubey, et al. Dynamico-1.0, an icosahedral hydrostatic dynamical core designed for consistency and versatility. *Geoscientific Model Development*, 8(10):3131–3150, 2015.

EPSC Abstracts
Vol. 11, EPSC2017-352-1, 2017
European Planetary Science Congress 2017

Seasonal Evolution in the Behavior of Titan's Clouds from *Cassini* ISS, 2004–2017

E.P. Turtle (1), J.E. Perry (2), J.M. Barbara (3), R.A. West (4), A.D. Del Genio (3), A.S. McEwen (2)
(1) Johns Hopkins Applied Physics Laboratory, Maryland, USA (Elizabeth.Turtle@jhuapl.edu), (2) University of Arizona, Arizona, USA (3) NASA GISS, New York, New York, USA, (4) JPL, California, USA

Abstract

Cassini's Imaging Science Subsystem (ISS) has documented the changes in cloud distributions, morphologies, and behavior that have accompanied Titan's changing seasons from southern summer at the time of Cassini's arrival in July 2004, through southern-autumnal/northern-vernal equinox in 2009, to early northern summer in 2017 (Fig. 1).

Early on, large convective cloud systems were common over Titan's South Pole (Fig. 1A) [*e.g.*, 1-2], and in the case of a large cloud outburst in October 2004 [1] led to substantial precipitation at Arrakis Planitia [3-4]. Such storms became less common after 2005 [*e.g.*, 5] as southern summer waned. Elongated streaks of clouds (Fig. 1B), sometimes extending over several hundred kilometers and in which convective behavior has been documented [6], were observed consistently at mid-southern latitudes (~40-50° S) from early in the mission until late 2012, well after the southern autumnal equinox. Isolated clouds have also been observed at lower southern latitudes (Fig. 1C).

Starting in 2007 as the sun rose in Titan's north, clouds began to appear at northern latitudes >55◦ N (Fig. 1D). Such clouds were relatively common until the equinox when northern cloud activity dropped off precipitously.

In September 2010, about a year after the equinox, a large outburst was seen, this time at low southern latitudes (Fig. 1E-F). The large arrow-shaped cloud [9] was followed by extensive surface changes due to precipitation across Concordia and Hetpet Regiones, Yalaing Terra, and Adiri [7-8]. After this storm, cloud activity became very rare, with only a few isolated clouds observed at mid-southern and mid-northern latitudes for ~5 years (Fig. 1), suggesting that methane was removed from the atmosphere and the lapse rate stabilized, similar to the drop in activity following the 2004 south-polar storm [5, 10].

As northern summer approaches, the expectation based on atmospheric circulation models [*e.g.*, 11-14] is that storm activity will pick up at Titan's high northern latitudes, as was observed at high southern latitudes upon *Cassini's* arrival. Activity finally began to pick up in 2016, and clouds became common at around 55°N and near Titan's north pole in 2016 (Fig. 1G). However, north-polar storms have yet to appear. Observations of Titan's high northern latitudes by ISS and the Visual and Infrared Mapping Spectrometer (VIMS) during *Cassini's* T120 and T121 flybys in June and July 2016, appeared to show clouds at the longer wavelengths, while surface features were detected at the shorter wavelength (938 nm) of the ISS images. The apparent discrepancy appears to be the result of high-altitude cirrus that is optically thick compared to Titan's atmospheric haze at longer wavelengths but optically thin compared to the haze at shorter wavelengths [15].

We will present observations of Titan's cloud behavior over the course of the *Cassini* mission, documenting changes over the past 13 years, comparisons to other observations [*e.g.*, 16, 17] and models, and implications for Titan's atmospheric circulation. Of particular interest are long-anticipated changes in activity at high northern latitudes and corresponding changes on the surface or in the shorelines of lakes and seas, as the northern solstice approaches.

Acknowledgements

The authors wish to express their gratitude to all who have worked to make the *Cassini-Huygens* mission possible. Research supported by the *Cassini-Huygens* mission, a cooperative endeavor of NASA, ESA, and

ASI managed by JPL/Caltech under contract with NASA.

References

[1] Schaller et al. (2006) *Icarus* **182**, 224-229.

[2] Porco et al. (2005) *Nature* **434**, 159-168.

[3] Turtle *et al.* (2009) *GRL* **36**, L02204.

[4] Turtle *et al.* (2011a) *Icarus* **212**, 957-959.

[5] Schaller et al. (2006b) Icarus 184, 517-523.

[6] Griffith et al. (2007) Science 310, 474-477.

[7] Turtle *et al.* (2011b) *Science* **331**, 1414-1417.

[8] Barnes *et al.* (2013) *Planetary Science* **2**:1.

[9] Mitchell *et al.* (2011) *Nature Geoscience* **4,** 589-592.

[10] Turtle *et al.* (2011c) *GRL* **38**, L03203.

[11] Mitchell (2008) *JGR* **113**, E08015.

[12] Schneider *et al.* (2012) *Nature* **481**, 58-61.

[13] Lora *et al.* (2015) *Icarus* **250**, 516-528.

[14] Newman *et al.* (2016) *Icarus* **267**, 106-134.

[15] Turtle *et al.* (2016) *AGU Fall Mtg.,* Abstract P33F-05.

[16] Rodriguez *et al.* (2011) *Icarus* **216**, 89-110.

[17] Corlies *et al.* (2017) *LPSC* **48**, Abstract #2780.

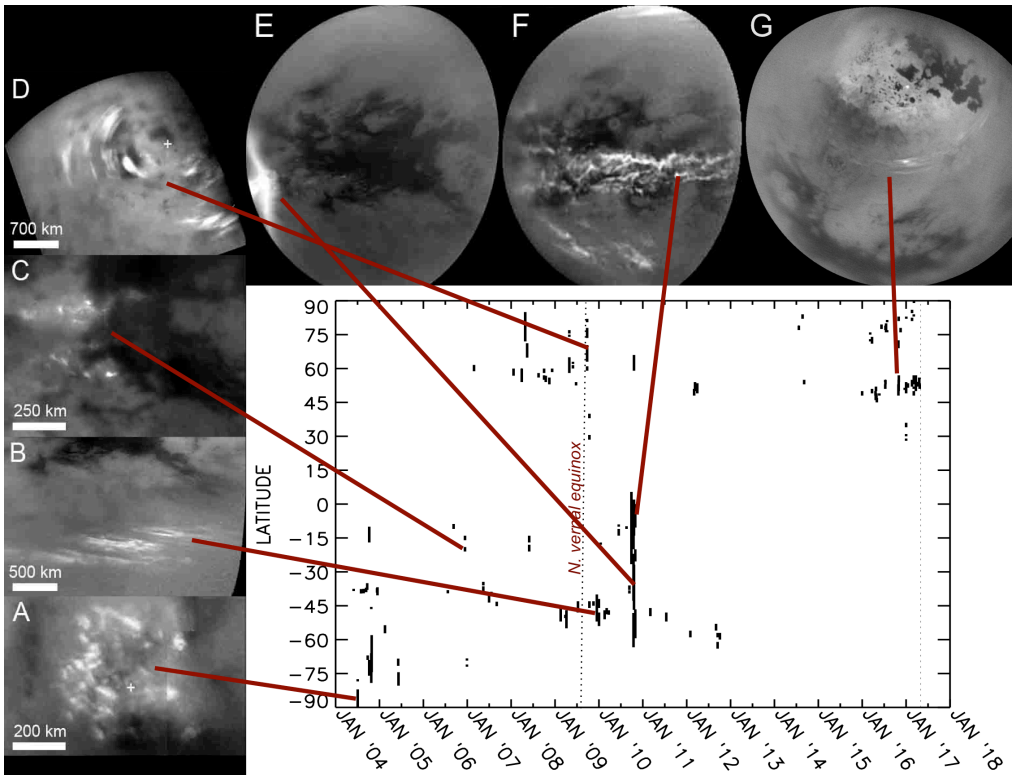

Figure 1: ISS images of different types of clouds (A-G) and graph showing observed cloud latitude over time.

EPSC Abstracts
Vol. 11, EPSC2017-365, 2017
European Planetary Science Congress 2017

Bladed Terrain on Pluto: Possible Origins and Evolution

J.M. Moore (1), A.D. Howard (2), O.M. Umurhan (1), O.L. White (1), P.M. Schenk (3), R.A. Beyer (1, 4), W. M. Grundy (5), L.A. Young (6), S.A. Stern (6), H.A. Weaver (7), C.B. Olkin (6), K. Ennico (1)

(1) National Aeronautics and Space Administration (NASA) Ames Research Center, CA, USA, (2) University of Virginia, VA, USA, (3) Lunar and Planetary Institute, TX, USA, (4) The SETI Institute, CA, USA, (5) Lowell Observatory, AZ, USA, (6) Southwest Research Institute, CO, USA, (7) Johns Hopkins University Applied Physics Laboratory, MD, USA, (jeff.moore@nasa.gov)

Abstract

We conclude that Bladed Terrain on Pluto is a deposit of massive CH_4, which preferentially precipitates at high elevations, and has since its initial formation, undergone episodes of sublimation erosion that has given this deposit its characteristic texture.

1. Introduction & Observations

Bladed terrain on Pluto is observed to occur within latitudes 30° of the equator and found almost exclusively on the highest elevations (>2 km above the mean radius) where observed in the hemisphere best seen by *New Horizons* (Fig. 1). Well-developed blades are typically spaced ~3 - 7 km crest-to-crest, have a typical local relief of ~300 m, and flank slopes of ~20°. Blades dominantly display a N-S orientation, but those near the equator additionally exhibit a more rectilinear pattern. The blades are located on broad ridges averaging ~100 km wide (Tartarus Dorsae), separated by troughs that appear to be of structural origin. Color data of the non-encounter hemisphere hint that Bladed Terrain may extensively occur within the ±30° latitude band. As such, these putative Bladed Terrain regions presumably also occur at high elevations.

2. Analysis

Observations do not readily point to a single simple analogous terrestrial or planetary process or landform. We have separately considered the origin of the Bladed Terrain Deposits (BTD), and the bladed textures on their surface. The latter may have developed at a later time and by a different process. We first considered processes that form both the deposits and the blades themselves (endogenic extrusion and aeolian sand erg development). The principle objection to these hypotheses was that the blades occur on ridges rather than in depressions, as is commonly seen for these processes on other planetary surfaces. Instead, the strong correlation of BTD occurrence with high elevation suggests an atmospheric temperature control and source for their presence and modification. During the time of the encounter, with the exception of the 1 km-thick boundary layer exclusively above Sputnik Planitia, Pluto's lower atmosphere temperature profile displayed an increase with altitude. The consequence of warmer air temperatures at higher altitudes is that the condensation of N_2 ice is suppressed, while the formation of CH_4 ice is currently promoted at high elevation. Changes in atmospheric mass can encourage erosion of CH_4 ice. We conclude that since the time the BTD were emplaced, there have been sufficient excursions in Pluto's climate to partially erode these deposits into the blades we see today. The blades themselves are partially analogous to penitentes on terrestrial, low-latitude, high-elevation ice fields [1], [2]. The processes that contribute to, and control the amplitude and spacing of, the blades are not yet fully understood. For instance, these Plutonian blades are at least two orders of magnitude larger than terrestrial penitentes. Plutonian blades may be entirely erosional, like terrestrial penitentes, or may form by erosion at the base and condensation at the crests, which is marginally permitted in Pluto's current climate at those altitudes.

3. Conclusions & Implications

We suggest that the west to east sequence of landform elements from the lowlands of Sputnik Planitia, through the Bright, Pitted Uplands, to the BTD are genetically related and are driven by ices sublimated from Sputnik Planitia and condensed (and further modified) on the uplands to the east. The Bright, Pitted Uplands and the BTD occupy the same

latitude belt and manifest a surficial compositional sequence from dominance by N_2 ice closest to Sputnik Planitia (including return-flow N_2 glaciation) to increasing dominance of CH_4 ice to the east culminating in the BTD. This compositional sequence corresponds to an altitudinal control on ice stability, with only CH_4 being stable at high relative elevations. Atmospheric modeling to date has not demonstrated an eastward circulation in the equatorial latitude belt [3] under orbital and seasonal conditions during encounter. On the other hand, the high albedo of the Bright, Pitted Uplands suggests N_2 and CH_4 ice deposition has occurred in this latitude belt east of Sputnik Planitia within the recent geologic past. Thus Bladed Terrain, along with other deposits of volatiles in Tombaugh Regio proper (including Sputnik Planitia), represents an active response of the landscape to current and past climates.

Acknowledgements

We wish to thank our colleagues who have worked on this research: T. Bertrand, G. Collins, D. Cruikshank, A. Earle, F. Forget, W. McKinnon, F. Nimmo, S. Protopapa, B. Schmitt, K. Singer, and J. Spencer. This work was supported by the *New Horizons* Project.

References

[1] Moore, J.M., et al., The geology of Pluto and Charon through the eyes of New Horizons, *Science*, 351, aad7055, 1284-1293, 2016.

[2] Moores, J.E., Smith, C.L., Toigo, A.D., and Guzewich, S.D., Penitentes as the origin of the bladed terrain of Tartarus Dorsa on Pluto, *Nature*, 541, 188-190, 2017.

[3] Forget, F., Bertrand, T., Vangvichith, M., Leconte, J., Millour, and E., Lellouch, E., A post-New Horizons global climate model of Pluto including the N_2, CH_4 and CO cycles, *Icarus*, 287, 54-71, 2017.

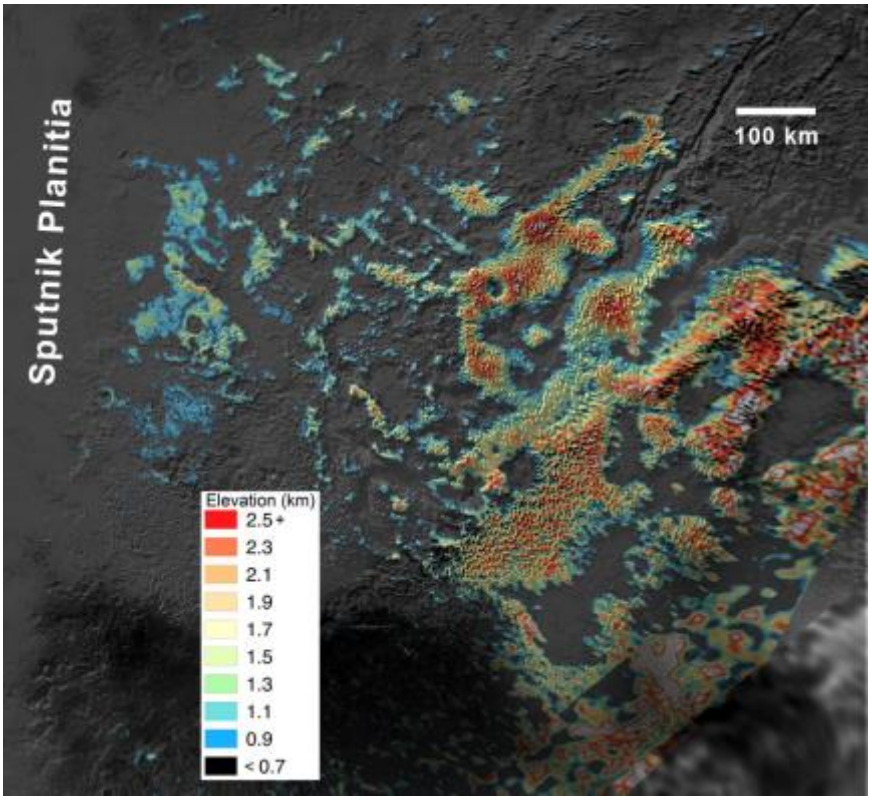

Figure 1. Outcrops of Bladed Terrain are strongly correlated with elevations of around +2 km and above (relative to the mean planetary radius of 1188.3 km).

EPSC Abstracts
Vol. 11, EPSC2017-367, 2017
European Planetary Science Congress 2017

Cassini: Going out in a Science-Rich Blaze of Glory

L.J. Spilker (1), S.G. Edgington (1), and N. Altobelli (2)
(1) Jet Propulsion Laboratory/California Institute of Technology, USA (linda.j.spilker@jpl.nasa.gov), (2) ESA/ESAC, Spain

Abstract

After 13 years in orbit, the Cassini-Huygens Mission to Saturn, a collaboration of NASA, ESA, and ASI, ended in a science-rich blaze of glory. Cassini sent back its final bits of unique science data on September 2017, as it plunged into Saturn's atmosphere, vaporizing and satisfying planetary protection requirements. Before that time Cassini made amazing new science discoveries. The science highlights of the Ring Grazing and Grand Finale orbits will be discussed.

1. Saturn System Exploration

Cassini's exploration of the Saturn System is composed of five broad, overlapping scientific disciplines: Titan, the atmosphere of Saturn, rings, magnetosphere, and icy satellites.

In each area, Cassini made major discoveries, provided answers to old questions, and posed new questions that could only be answered in the mission's final orbits. Among many firsts, Cassini: discovered icy jets of material streaming from tiny Enceladus' south pole, revealed a global ocean underneath its icy crust, found evidence for active hydrothermal vents on its seafloor and revealed an ocean world that was potentially habitable. Enceladus is the source of the E Ring and water from its jets dominates the magnetosphere. Cassini also found hydrocarbon lakes and seas on Titan; detected a sub-surface ocean Titan as well; provided multi-wavelength coverage of a great northern storm, the first of its kind on Saturn since 1990; demonstrated that the Saturn Kilometric Radiation period does not reflect the planet's internal rotation; revealed curtain-like aurorae and their true color flickering over Saturn's poles;; and constrained and complicated our understanding of the 3D structure and dynamics of multi-particle ring systems. In addition, the Huygens probe sent back amazing images of Titan's surface and made detailed measurements of atmospheric composition, structure and winds. Cassini's ocean world discoveries required a mission end that would not allow the spacecraft to impact and potentially contaminate these worlds once Cassini was out of fuel and could no longer navigate the Saturn system.

In its final year, Cassini completed its investigation of the Saturn system throughout half the planet's year. During this time, Cassini's science instruments probed as-yet unsolved mysteries, observed seasonal and temporal changes, and addressed new questions that have arisen during the mission.

2. Ring Grazing and Grand Finale Orbits

The final phase of Cassini's mission covered a period of roughly ten months and ended with the exploration for the first time of the region between the rings and planet, a rich source for discovery.

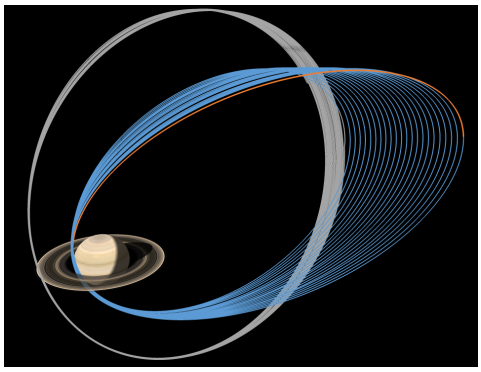

Figure 1: Cassini's 20 Ring Grazing (gray) and Grand Finale (blue) orbits. The last orbit (orange) will take Cassini into Saturn's atmosphere for vaporization.

In November 2016, Cassini transitioned to a series of 20 Ring Grazing orbits with peripases just outside Saturn's F ring (Figure 1, gray orbits). These orbits included close flybys of tiny ring moons, including Pan, Daphnis and Atlas, and excellent views of Saturn's F ring and outer A ring. The 127th and final close flyby of Titan propelled Cassini across Saturn's main rings and into its Grand Finale orbits.

Cassini's Grand Finale, began in late April 2017. It was comprised of 22 orbits at an inclination of 63 degrees (Figure 1, blue orbits). Cassini repeatedly dove between Saturn's innermost rings and upper atmosphere providing insights into fundamental questions unattainable during the rest of the mission. Cassini was the first spacecraft to explore this region. The last orbit took the spacecraft into Saturn on 15 September 2017, where it was vaporized by the planet's atmosphere.

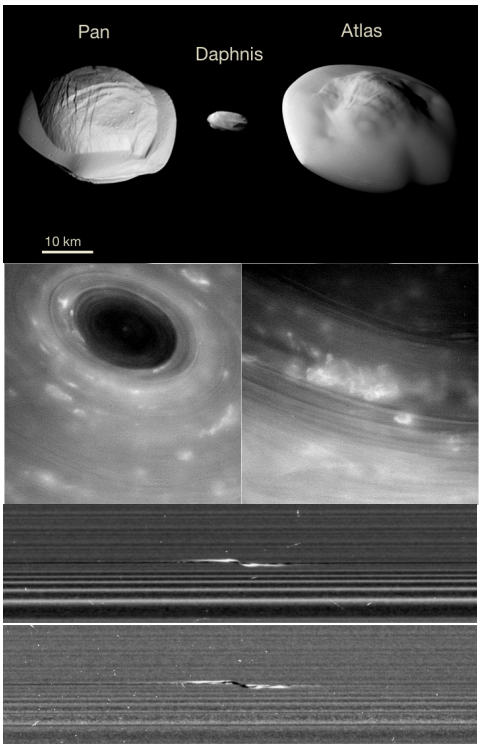

Figure 2: Comparison of the ring moons, Pan, Daphnis, and Atlas (above). Saturn's north polar vortex (middle left) and convective clouds over the hexagon jet stream (middle right). Ring propeller Santos-Dumont on lit (top) and unlit (bottom) sides of the rings.

The Grand Finale orbits provided the highest resolution observations of both the rings and Saturn, and direct in-situ sampling of the ring particle composition, plasma, Saturn's exosphere and the innermost radiation belts. Saturn's gravitational field was measured to unprecedented accuracy, providing information on the interior structure of the planet, winds in the outer layers of Saturn's atmosphere, and the mass distribution in the rings. Probing the magnetic field provided insight into the nature of the magnetic dynamo, and the structure of the internal magnetic field. The ion and neutral mass spectrometer sampled the exosphere and upper atmosphere for molecules that escape the atmosphere itself and water-based molecules originating from the rings. The cosmic dust analyzer directly sampled the composition of main ring particles for the first time from different parts of the main rings. Until the execution of these final orbits, the answers to such new questions remained mysteries.

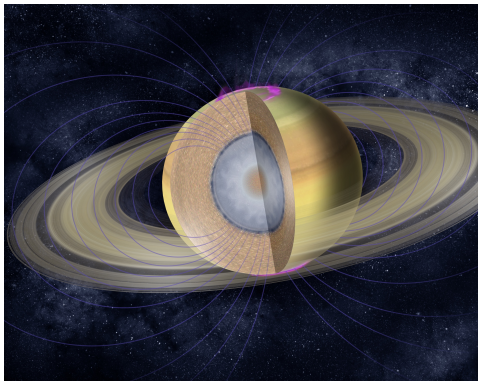

Figure 3: Grand Finale science goals focus on studying ring mass and composition, interior structure, magnetic dynamo, aurora, and atmospheric composition.

3. Summary and Conclusions

Cassini-Huygens exploration of Saturn has yielded 13 years of unprecedented discoveries, and answers to many scientific mysteries. The Ring Grazing and Grand Finale orbits returned unprecedented new science.

Acknowledgements

This work described here was carried out in part at the Jet Propulsion Laboratory, California Institute of Technology, under a contract with the National Aeronautics and Space Administration.

EPSC Abstracts
Vol. 11, EPSC2017-386, 2017
European Planetary Science Congress 2017

Saturn's Atmospheric Photochemistry: Haze Production in Ring-Shadowed Atmosphere and within the Hexagon

S.G. Edgington (1), S.K. Atreya (2), E.H. Wilson (3), K.H. Baines (1,4), R.A. West (1), G.L. Bjoraker (5), L.N. Fletcher (6), T. Momary (1)
(1) Jet Propulsion Laboratory/California Institute of Technology, USA (scott.g.edgington@jpl.nasa.gov), (2) University of Michigan, USA, (3) Space Environment Technologies, USA, (4) University of Wisconsin, USA , (5) NASA Goddard Space Flight Center, USA, (6) University of Oxford, UK

Abstract

Cassini has been orbiting Saturn for nearly thirteen years. During this epoch, the ring shadow has moved from covering a relatively large portion of the northern hemisphere (Figure 1a) to covering a large swath south of the equator as solstice approaches. At Saturn Orbit Insertion on July 1, 2004, the sub-solar point was ~24º South. At this time, the projection of the optically thick B-ring onto Saturn reached as far as 40ºN along the central meridian (~52ºN at the terminator). At its maximum extent, the ring shadow can reach as far as 48ºN/S (~58ºN/S at the terminator). The net result is that the intensity of both ultraviolet and visible sunlight penetrating into any particular latitude will vary greatly depending on both Saturn's axis relative to the Sun and the optical thickness of each ring system. In essence, the rings act like semi-transparent Venetian blinds (Figure 2) over the atmosphere of Saturn.

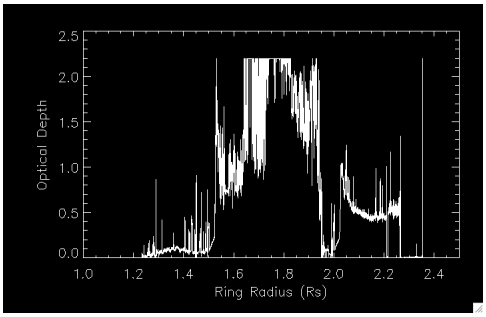

Figure 2. The optical depth of Saturn's rings in the ultraviolet (Josh Colwell, *pers. comm.*) The rings act like a periodic Venetian blind that will shield atmospheric molecules from solar photons.

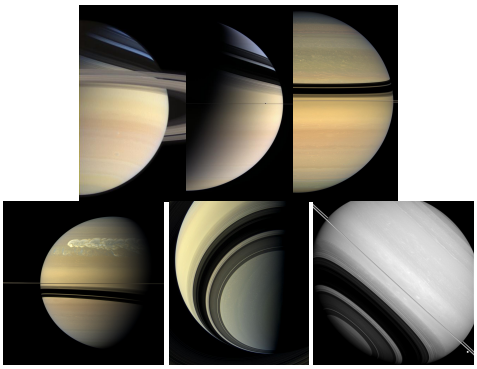

Figure 1. Saturn's atmosphere changes in response to the changing inclination of the ring plane relative to the Sun: (a) December 14, 2004, (b) March 16, 2006, (c) April 23, 2008, (d) July 6, 2011, (e) July 29, 2013, (f) November 24, 2014. Images are courtesy of NASA/JPL/Space Science Institute.

Our previous work [1,2] examined the variation of the solar flux as a function of solar inclination, i.e. ~7.25 year season (Figure 3) at Saturn. Beginning with methane, phosphine and ammonia, we investigate the impact on production and loss rates of the long-lived photochemical products leading to haze formation are examined at several latitudes over a Saturn year. We report on the impact of the oscillating ring shadow on the photolysis and production rates of hydrocarbons in Saturn's stratosphere and upper troposphere, including acetylene, ethane, and propane. Similarly, we assess its impact on phosphine abundance, a disequilibrium species whose presence in the upper troposphere is a tracer of convection processes in the deep atmosphere. Comparison to the corresponding rates for the clear atmosphere and for the case of Jupiter, where the solar insolation is known to be insignificant (~3º inclination), will also be presented. We will present our ongoing analysis of Cassini's CIRS, UVIS, and VIMS datasets that provide abundances of key molecules and an estimate of the

evolving haze content of the northern hemisphere and we will begin to assess the implications for dynamical mixing.

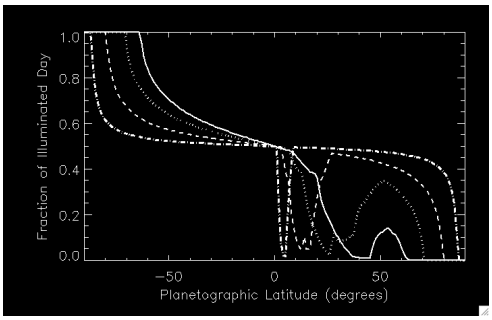

Figure 3. This plot illustrates the fraction of Saturn's day that is illuminated by the Sun as a function of solar declination, i.e. season. The curves correspond to sub-solar points of 26.7ºS (solid), 19.6ºS (dotted), 10.7ºS (dashed), and 3.5ºS (dot-dashed). Ultimately, this will determine the flux of photons allowed to enter the atmosphere relative to those of a clear, un-shaded atmosphere.

In addition, we will examine how the now famous hexagonal jet stream acts like a barrier to transport, isolating Saturn's north polar region from outside transport of photochemically-generated molecules and haze. We explore the role of increasingly intense sunlight in explain the buildup of hydrocarbon hazes in this region, which is relatively unaffected by transport from more southerly latitudes (Figure 4).

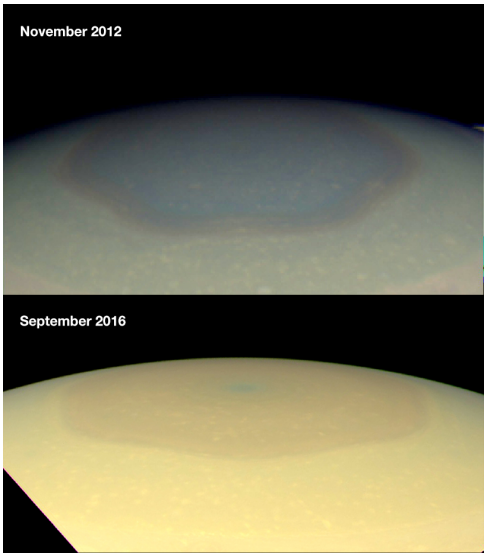

Figure 4. One of the aims of this exercise is to characterize the haze content Saturn's atmosphere. Several Cassini data sets from ISS (above) and VIMS (below) are being used to meet this goal.

Acknowledgements

The research described in this paper was carried out in part at the Jet Propulsion Laboratory, California Institute of Technology, under a contract with the National Aeronautics and Space Administration. Copyright 2017, California Institute of Technology. Government sponsorship is acknowledged.

References

[1] Edgington, S.G., A.A. Simon-Miller, R. Achterberg, G. Bjoraker, P. Romani, F.M. Flasar, J. Colwell, 2006. Adaptation of a 2-D Photochemical Model to Improve Our Understanding of Saturn's Atmosphere. *Bull. American. Astron. Soc.*, **38**, 499 (#11.23).

[2] Edgington, S.G., R.A. West, K.H. Baines, S.K. Atreya, E.H. Wilson, G.L. Bjoraker, L.N. Fletcher, and T. Momary, 2012. Photochemistry in Saturn's Ring Shadowed Atmosphere: Modeling, Observations, and Preliminary Analysis. *Bull. American. Astron. Soc.*, **38**, 499 (#11.23).

EPSC Abstracts
Vol. 11, EPSC2017-407, 2017
European Planetary Science Congress 2017

Lightning activity on Saturn during Cassini's orbital tour and the Grand Finale

G. Fischer (1), W. S. Kurth (2), G. Hospodarsky (2), and P. Zarka (3)
(1) Space Research Institute, Austrian Academy of Sciences, Graz, Austria (georg.fischer@oeaw.ac.at)
(2) Department of Physics and Astronomy, The University of Iowa, Iowa City, USA
(3) LESIA, Observatoire de Paris, Meudon, France

Abstract

Since 2004 the Cassini spacecraft has observed Saturnian lightning storms with durations of a few days up to serveral months [1]. Saturnian thunderstorms raged at certain latitude bands, preferentially at the so-called storm alleys around 35° south and 35° north. The lightning discharges in these thunderstorms are thought to originate from areas of the atmosphere where there are water clouds at similar temperatures to terrestrial clouds, but at a higher pressure level of 8–10 bars. There are two different classes of Saturn lightning storms: The "smaller" storms have a horizontal extent around 2000 km and a flash rate of a few flashes per minute, and there are the rare and giant "Great White Spots" with latitudinal diameters of 10,000 km with a flash rate of a few flashes per second [2]. Cassini was lucky to observe such a Great White Spot in the years 2010 and 2011 [3]. After the Great White Spot the lightning activity on Saturn decreased considerably, and to date the last small thunderstorm was observed in October 2013.

The Cassini RPWS (Radio and Plasma Wave Science) instrument has monitored the flash rates by detecting the radio emissions from Saturn lightning discharges radiated at high frequencies (in the MHz range) above the ionospheric cutoff frequency. However, lightning is known to also emit whistler waves at low frequencies propagating along magnetic field lines from the source to the observer. In the case of Saturn the detection of only one lightning whistler has been reported in the literature [4], albeit there were no corresponding high-frequency radio emissions detected at the same time. The lack of whistler detection can be explained by Cassini's trajectory since the storm alleys at a planetocentric latitude of 35° connect to a magnetic L-shell of $L = 1.44$. With the exception of Saturn Orbit insertion, the Cassini spacecraft was never located at such low L-shells until the beginning of the Grand Finale. The Grand Finale orbits, with Cassini traversing between the innermost ring and Saturn's upper atmosphere, should allow us to observe lightning whistlers and strong high-frequency radio emissions of lightning. We are hoping for more thunderstorm activity on Saturn, and we will report on possible new detections of Saturn lightning during the Grand Finale orbits in this presentation.

References

[1] Fischer, G., Gurnett, D.A., Kurth, W.S., Akalin, F., Zarka, P., Dyudina, U.A., Farrell, W.M., and Kaiser, M.L.: Atmospheric electricity at Saturn, Space Sci. Rev., Vol. 137, 271-285, 2008.

[2] Aplin, K., and Fischer, G.: Lightning detection in planetary atmospheres, Weather, Vol. 72, 2, 46-50, 2017.

[3] Fischer, G., Kurth, W.S., Gurnett, D.A., Zarka, P., Dyudina, U.A., Ingersoll, A.P., Ewald, S.P., Porco, C.C., Wesley, A., Go, C., and Delcroix, M.: A giant thunderstorm on Saturn, Nature, Vol. 475, 75-77, 2011.

[4] Akalin, F., Gurnett, D.A., Averkamp, T.F., Persoon, A.M., Santolik, O., Kurth, W.S., and Hospodarsky, G.B.: First whistler observerd in the magnetosphere of Saturn, Geophys. Res. Lett., Vol. 33, L20107, 2006.

EPSC Abstracts
Vol. 11, EPSC2017-434, 2017
European Planetary Science Congress 2017

A planetary-scale disturbance in a long-living three-vortex coupled system in Saturn's atmosphere

T.del Río-Gaztelurrutia (1), A. Sánchez-Lavega (1), A. Antuñano (1), J. Legarreta (2), E. García Melendo (3), K. Sayanagi (4), R. Hueso (1), M. Wong (5), S. Pérez-Hoyos (1), J.F. Sanz-Requena (6), J.F. Rojas (1), A. Simon (7), I. de Pater (5), T. Barry (8)
(1) Dept. de Física Aplicada I, Escuela de Ingeniería de Bilbao, UPV/EHU, 48013 Bilbao, Spain. (2) Dept. de Ingeniería de Sistemas y Automática, Escuela de Ingeniería de Bilbao, UPV/EHU, 48013 Bilbao, Spain.(3) Fundació Observatori Esteve Duran, Montseny 46, 08553 Seva, Spain (4) Dept of Atmospheric and Planetary Sciences, Hampton University, Hampton, VA 23668, USA (5) Dept of Astronomy, University of California, 501 Campbell Hall, Berkeley, California 94720, USA(6) Universidad Europea Miguel de Cervantes, Dept de Ciencias Experimentales, C/Padre Julio Chevalier, 2, 47012 Valladolid, Spain. (7) NASA Goddard Space Flight Center/690, 8800 Greenbelt Road, Greenbelt, Maryland 20771, USA (8) Broken Hill Observatory, 406 Bromide Street, Broken Hill, New South Wales 2880, Australia

Abstract

The zonal wind profile of Saturn has a singular structure in the latitude range 50ºN-65ºN planetocentric, with a double peak that reaches maximum zonal velocities close to 100ms^{-1}[1]. A survey of Cassini ISS images shows that a system of three vortices formed in this latitudinal region in 2012 and has remained active until present, confirming that vortices in Saturn can be long lived [2]. In May 2015 a disturbance started to develop at the location of the triple vortex. Since at the time Cassini orbits were not favorable to the observation of the region, we were granted Director Discretionary Time of the Hubble Space Telescope to observe the region before the perturbation faded away. Here we report the dynamics and vertical structure of the three-vortex system and of the disturbance that developed at its location, based on HST and Cassini images. We also present results of numerical models to explain the stability of vortices in the region.

1. The three-vortex system: History, evolution and local motions

The appearance of the three vortices in Cassini ISS CB2 and MT3 filters (See figure 1), and their latitude in the zonal wind profile, suggest that the system is formed by one cyclone surrounded by two anticyclones. In the methane deep absorbing filter MT3, the central vortex appears dark relative to its surrounding, while the two other vortices are brighter, indicating that the central vortex is located lower in the atmosphere and the surrounding vortices higher, as expected from their cyclonic / anticyclonic character. The relative altitude of the different structures is confirmed by a radiative-transfer analysis of the system in a variety of filters. The three vortices are almost circular, with diameters ~2,000-3,000km, and their sizes have not changed noticeably in the years 2012-2015. We have tracked the motion of the system since 2012. The central cyclone is located at an average 58.5º±0.8ºN (planetocentric), drifting 11.55º/day, u=69.0±1.6ms^{-1}, essentially following the wind profile, with slight oscillations of amplitude ~10º and a period of ~8 months.

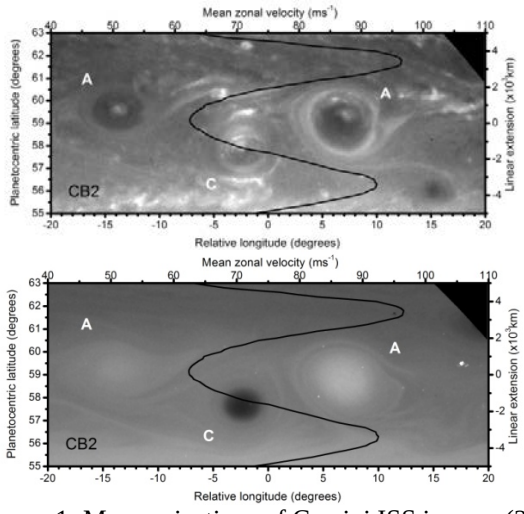

Figure 1: Map projections of Cassini ISS images (27 Feb 2013) showing also the zonal winds.

Using Cassini high resolution images, we have measured local motions within the vortices. They confirm the cyclonic/anticyclonic character of the vortices, and allow us to estimate the eddy vorticity which is (3±2)×10^{-5}s^{-1} in the cyclone, and -(5±2)×10^{-5}s^{-1} and -(3±2)×10^{-5}s^{-1} in the anticyclones.

2. The disturbance

On 13 May 2015, near Saturn opposition, the amateur community was stirred by the presence of a "rift" at the location of the vortices, which appeared in low-resolution observations as a single spot. Soon after, the region surrounding the spot appeared disturbed, and the perturbation extended longitudinally for ~2 months, at the end of which the perturbed region occupied about a third of the latitudinal circle. Using ground-based observations we found that the disturbance expanded eastwards at -1.65º/day. Cassini images at the time of the disturbance showed the presence of a vortex south of the system at 55ºN that was again visible at the expected location of the limit of the disturbance once it had subdued, in Sep 2015, and which could be found in earlier images, approaching the triple vortex at 1.70º/day, suggesting that the origin of the disturbance could have been the interaction of this new vortex with the three vortex system.

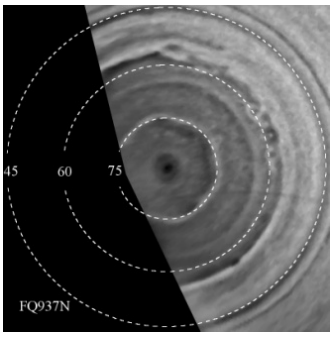

Figure 2: Polar projection of Saturn North hemisphere from a single HST/WFC3 image acquired on 30-06-2015.

HST/WFC3 images (Figure 2) allowed us to retrieve motions of local features in the perturbed region at the time of the disturbance. We find that they follow within error the average zonal wind profile, showing that the dynamics of the region is dominated by the advection by the zonal winds and supporting the hypothesis that the disturbed area is the result of the advection of the clouds created by the interaction of the system of vortices with the vortex at the south.

3. Numerical models

We modeled the triple vortex system by using the EPIC model [3] and a shallow water model (SW) [4] to study the possible mutual interactions among the three vortices. In the EPIC model, the vertical domain spanned between 500 and 200 mbar and was divided in three layers. No vertical shear for the zonal winds was assumed, and simulations had a 0.11 degree pixel^{-1} horizontal resolution. The vertical thermal profile was set to strongly stable with an average Brunt-Väisälä frequency of 7.7×10^{-3} s^{-1}. The SW model was a one-layer with a Rossby radius of deformation of ~300 km and a spatial resolution of 0.1 degree pixel^{-1}. Zonal winds were imposed as described in [4]. Figure 3 shows an outcome of the SW model in the form of potential vorticity field where the three vortices are present.

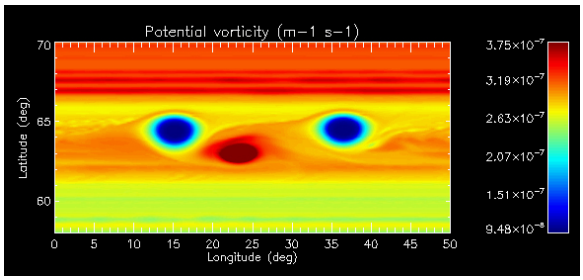

Figure 3: Potential vorticity from a one-layer SW simulation after 25 days. Latitudes are planetographic.

Acknowledgements

Work supported by AYA2015-65041-P (MINECO/FEDER, UE); Grupos Gobierno Vasco IT-765-13; and UFI11/55 (UPV/EHU). We acknowledge the three orbits from HST director assigned for this research (DD Program 14064, IP A. Sánchez-Lavega).

References

[1] Del Genio, et al.: Saturn Atmospheric Structure and Dynamics. Chapter 6 in: Saturn from Cassini-Huygens. M. Dougherty, L. Esposito and T. Krimigis (editors), Springer-Verlag, pp 113-159, 2009.

[2] del Río-Gaztelurrutia et al.: A long-lived cyclone in Saturn's atmosphere: observations and models. Icarus, 209, pp 665-681, 2010.

[3] Dowling, et al.: The explicit planetary isentropic-coordinate (EPIC) atmospheric model. Icarus, 132, pp 221-238, 1998.

[4] García-Melendo, E. and A. Sánchez-Lavega: Shallow water simulations of Saturn's giant storms at different latitudes Icarus, 286, pp 241-260, 2017.

EPSC Abstracts
Vol. 11, EPSC2017-450, 2017
European Planetary Science Congress 2017

Saturn at Northern Summer Solstice: Thermal Structure during the Finale of the Cassini Mission

L.N Fletcher (1), S. Guerlet (2), G.S. Orton (3), J.A. Sinclair (3), T. Fouchet (4), P. Irwin (5), L. Li (6), F.M. Flasar (7)
(1) Department of Physics and Astronomy, University of Leicester, UK (leigh.fletcher@le.ac.uk; Tel: +44 116 252 3585); (2) Laboratoire de Meteorologie Dynamique, Paris, France; (3) Jet Propulsion Laboratory, Pasadena, USA; (4) LESIA, Observatoire de Paris, France; (5) Atmospheric, Oceanic and Planetary Physics, University of Oxford, UK; (6) Department of Physics, University of Houston, USA; (7) NASA Goddard Spaceflight Center, Maryland, USA.

Abstract

Cassini's orbital exploration of Saturn (2004-2017) has almost spanned from solstice to solstice, providing an unprecedented database of seasonal and non-seasonal atmospheric phenomena on the gas giant planet [1]. We report on the completion of our long-term campaign of thermal-infrared (7-1000 μm) observations from the Composite Infrared Spectrometer (CIRS), extending previous investigations of (i) the establishment of a large, warm polar stratospheric hood (75-90°N) in the northern summer hemisphere [2]; (ii) tracking of the equatorial stratospheric quasi-periodic oscillation (QPO) and the disappearance of the strong prograde jet in the equatorial stratosphere [3]; and (iii) the aftermath of the 2010-11 storm system and 'beacon' at mid-latitudes, both in a warm tropospheric band and residual wave activity in the stratosphere [4]. CIRS observations will be compared to ground-based 7-25 μm images from the Very Large Telescope (VLT) in 2015-2017, and to the record of IRTF observations from the previous northern summer solstice in 1987. Nadir CIRS spectra are inverted to determine zonal-mean variability in temperatures, para-hydrogen, ethane and acetylene. The resulting distributions trace large-scale circulation patterns at the equator and poles, and disruptions of these circulations by localised dynamic phenomena.

1. Introduction

With its 29.5-year orbital period and 26.7° axial tilt, Saturn's atmosphere is subjected to extremes of seasonal insolation that drive complex patterns of atmospheric circulation, chemistry, and cloud formation [1] that can be explored via thermal-infrared remote sounding. Cassini arrived at Saturn in July 2004 (Ls=293°), shortly after northern winter solstice (Ls=270° in 2002) when the north pole was shrouded in darkness. The longevity of Cassini has meant that our infrared records now span through spring equinox (Ls=0°, August 2009) and to northern summer solstice (Ls=90° on May 24, 2017), allowing us to explore processes over all four seasons on Saturn. We construct monthly-averaged zonal-mean CIRS spectra for inversion via an optimal-estimation retrieval algorithm, NEMESIS [5], Fig. 1. These are interpolated in time to reconstruct the temperature and composition variability over 13 years, and are used to explore processes in the following regions.

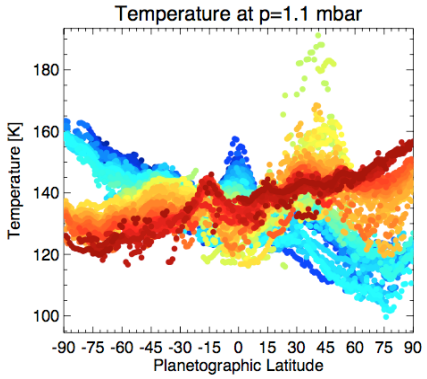

Figure 1 Example of 1-mbar temperatures from inversion of CIRS spectra early (blue) and late (red) in the mission, highlighting the shifting thermal asymmetries and equatorial oscillation.

2. Seasonal Polar Vortices

Saturn exhibits seasonally-independent warm polar cyclones in the troposphere at both poles [6], in addition to seasonally-dependent polar hoods in the stratosphere (within ~15° of the pole). Our previous study [2] tracked the evolution of these polar vortices to early 2014, showing the longevity of the polar cyclones; the disappearance of the southern summer polar hood; and the absence (at that time) of any comparable northern polar hood in spring (Ls=56°). Observations from northern summer in March 1989 (Ls=104°) by Gezari et al. [7] show the existence of the warm northern hood, suggesting that Cassini could see it by the end of the Grand Finale mission. Recent 7.8-μm observations from VLT (2016, Fig. 2)

show that the north pole is certainly warming, but lacks the strong gradient and contrast that the southern summer hood exhibited in 2004, and which was evident in the 1989 images from Gezari et al. The evolution of these thermal gradients, and associated maxima in ethane and acetylene, will be presented using 2017 CIRS and VLT data.

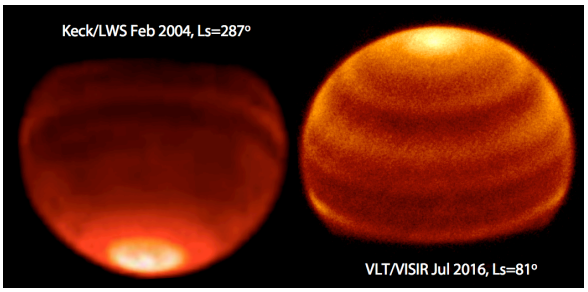

Figure 2 Comparing polar vortices in Saturn's 7.8-μm emission in southern summer (left) and late northern spring (right).

3. Equatorial Oscillations

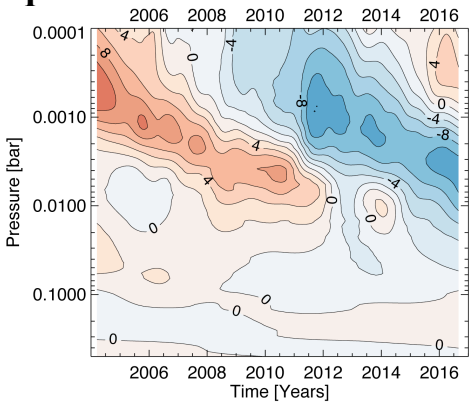

Figure 3 Equatorial temperature anomalies (compared to the mean over the full mission) showing the downward propagation of thermal anomalies.

Shortly after Cassini's arrival, Saturn's equatorial stratosphere was shown to exhibit vertical temperature/wind oscillations driven by wave-mean-flow interactions, analogous to Earth's Quasi-Biennial Oscillation [8]. Alternating regions of eastward/westward flow appear to move downward with a ~15-year period, as shown via temperature anomalies in Fig. 3. This evolution removed the strong prograde stratospheric jet observed early in the mission [9], and replaced the equatorial maximum with a cool airmass near 1-5 mbar in 2017 that can be seen in Fig. 2. There is evidence that the northern springtime storm (see below) disrupted the regular oscillation in 2011-2014 throughout the ±20° latitude region [3], but that it has now re-established itself. Secondary circulation patterns modulate temperatures in the tropics (±15° latitude), making inferences of Hadley-type circulations complicated.

4. Aftermath of the Storm

Saturn's northern mid-latitudes were spectacularly disrupted in 2010/11 by the eruption of a storm near 40°N that encircled the entire latitude circle. The tropospheric storm generated a hot stratospheric vortex (the beacon) that was enhanced in hydrocarbons [10] due to chemistry and atmospheric subsidence. Our previous study [4] tracked the beacon through March 2012 – updated tracking in Fig. 4 shows the demise of the beacon in mid-2013, which will be compared to expectations of a radiative-climate model [11].

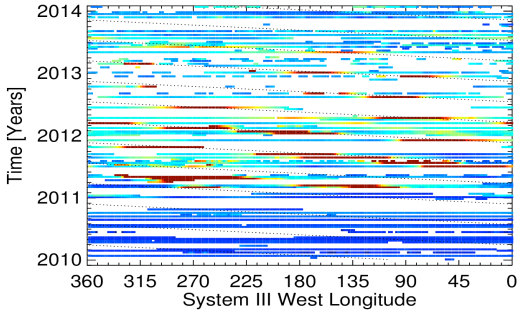

Figure 4 Tracking CH_4 emission from Saturn's beacon, showing the rapid westward motion (dotted lines) and disappearance after mid-2013.

Acknowledgements

LNF is supported by a Royal Society Research Fellowship and a European Research Council Consolidator Grant at the University of Leicester. We are indebted to the extraordinary efforts of the Cassini team in making these studies possible.

References

[1] Fletcher et al., 2015 (http://arxiv.org/abs/1510.05690)
[2] Fletcher et al., 2015 (doi:10.1016/j.icarus.2014.11.022)
[3] Fletcher et al., 2017, submitted.
[4] Fletcher et al., 2012 (doi:10.1016/j.icarus.2012.08.024)
[5] Irwin et al., 2008 (doi:10.1016/j.jqsrt.2007.11.006)
[6] Fletcher et al., 2008 (doi:10.1126/science.1149514)
[7] Gezari et al., 1989, (doi:10.1038/342777a0)
[8] Fouchet et al., 2008 (doi:10.1038/nature06912)
[9] Li et al., 2008 (doi:10.1029/2008GL035515)
[10] Moses et al., 2014 (doi:1 0.1016/j.icarus.2015.08.012)
[11] Guerlet et al., 2014 (doi:10.1016/j.icarus.2014.05.010)

EPSC Abstracts
Vol. 11, EPSC2017-501, 2017
European Planetary Science Congress 2017

Powering prolonged hydrothermal activity inside Enceladus

G. Choblet (1), G. Tobie (1), C. Sotin (2), M. Běhounková (3), O. Čadek (3), F. Postberg (4), O. Souček (5)
(1) Laboratoire de Planétologie et Géodynamique, UMR-CNRS 6112, Université de Nantes, France,
(2) Jet Propulsion Laboratory, Caltech, Pasadena, USA,
(3) Charles University, Department of Geophysics, Prague, Czech Republic,
(4) Institut für Geowissenschaften, Universität Heidelberg, Germany,
(5) Charles University, Mathematical Institute, Prague, Czech Republic.
(gael.choblet@univ-nantes.fr)

Abstract

A series of evidence gathered by the Cassini spacecraft indicates that Saturn's moon Enceladus is even more active than anticipated:
1) the observation of an elevated libration implies the existence of a global subsurface salty reservoir with a thin ice shell (20-25 km in average [1] and < 5 km in the South Polar Terrain, SPT [2, 3, 4]),
2) the intense jets at the South Pole seem associated to ongoing seafloor hydrothermal activity [5, 6].

Both observations require a huge heat power and a mechanism to focus the release of heat in the SPT, unexplained by previous models. Here we investigate heat generation by tidal friction in the porous core for core porosities consistent with Cassini gravity data [7]: tidal power potentially generates more than 20 GW thus explaining the existence of a global ocean.

We also model water transport in the tidally-heated permeable core in 3D geometry; simulated water circulation exhibits hot narrow upwellings with temperatures exceeding 90^{o}C, providing the fundamental mechanism for efficient water-rock-organics interactions. This results in the formation of powerful (1-5 GW) hotspots at the seafloor, explaining heat release in narrow regions, especially at the South Pole and thus, the uneven shell structure [2]. This also favors the transport of hydrothermal products from the core to the plume sources, consistent with the production of silica nano-particles [5] and the level of hydrogen estimated in Enceladus' plumes [6].

We predict that such activities can be sustained for tens of millions to billions of years.

References

[1] Thomas P.C.et al., Enceladus's measured physical libration requires a global subsurface ocean. Icarus, 264, 37-47 (2016).

[2] Čadek O. et al., Enceladus's internal ocean and ice shell constrained from Cassini gravity, shape, and libration data. Geophys. Res. Lett. 43, 5653-5660 (2016).

[3] Beuthe M., Rivoldini A., Trinh A., Enceladus?s and Dione's floating ice shells supported by minimum stress isostasy. Geophys. Res. Lett. 43 (2016).

[4] Le Gall A. et al., Thermally anomalous features in the subsurface of Enceladus's south polar terrain, Nat. Astro. 1 (2017)

[5] Hsu H.-W. et al., Ongoing hydrothermal activities within Enceladus. Nature 519, 207- 210 (2015).

[6] Waite J. H. et al., Cassini finds molecular hydrogen in the Enceladus plume: Evidence for hydrothermal processes. Science 356, 155-159 (2017).

[7] Iess, L. et al. The Gravity Field and Interior Structure of Enceladus. Science, 344, 78-80 (2014).

EPSC Abstracts
Vol. 11, EPSC2017-515-1, 2017
European Planetary Science Congress 2017

Investigating the thermal structure in Titan's atmosphere with a Net Exchange Rate formalism

J. Vatant d'Ollone (1), S. Lebonnois (1), S. Guerlet (1) and V. Eymet (2)
(1) Laboratoire de Météorologie Dynamique / IPSL, CNRS / UPMC, Box 99, Jussieu, 75005 Paris, France, (2) Meso-Star, Longages, France
(jan.vatant-dollone@lmd.jussieu.fr)

Abstract

Recent upgrades of the radiative transfer scheme in the Titan's 3-dimensional Global Climate Model developed at the Institut-Pierre-Simon-Laplace have led to improvements within the modeled circulation in the middle atmosphere compared to the previous works [4]. The simulated temperature profiles now feature a stratopause at an altitude consistent with the observations, and the stratospheric Hadley cell consequently tends to extend vertically. The minimum of zonal wind observed during Huygens descent [1] is also better reproduced in our simulations, as we observe a steep minimum in the vertical profile at all latitudes around 20-30 mbar. We discuss the possible origins of this feature in the model.

In this study the infrared opacities used in the *correlated-k* radiative transfer scheme in our GCM are also analyzed with a Net Exchange Rate Analysis formalism - on the basis of previous works on Venus atmosphere [2] - to analyze the energy exchanges in Titan's atmosphere and identify the dominant controls on the thermal profile. Hence it enables to investigate a possible radiative control of the zonal wind minimum - as it appears at a critical altitude where condensation of hydrocarbons and nitriles induce noticeable variations in gaseous and haze opacities [3] - as well as the sensitivity of the thermal profile control to the seasonal variations of trace compounds. The latter will be confronted to the results of [5] - *e.g.* strong cooling over the South winter pole correlated with global molecular enrichment - as a preliminary approach to the computation of radiative effect of these variations in the GCM radiative transfer scheme.

References

[1] Bird, M. K. et al: The vertical profile of winds on Titan, Nature, 438, pp. 800-802, 2005.

[2] Eymet, V. et al: Net exchange parameterization of thermal infrared radiative transfer in Venus' atmosphere, J. Geophys. Res., 114, E11008, 2009.

[3] Lavvas, P. et al: Titan's vertical aerosol structure at the Huygens landing site: Constraints on particle size, density, charge, and refractive index, Icarus, 210, pp. 832-842, 2010.

[4] Lebonnois, S. et al: Titan Global Climate Model: new 3-dimensional version of the IPSL Titan GCM, Icarus, 218, pp. 707-722, 2012.

[5] Vinatier, S. et al: Seasonal variations in Titan's middle atmosphere during the northern spring derived from Cassini/CIRS observations, Icarus, 250, pp. 95-115, 2015.

EPSC Abstracts
Vol. 11, EPSC2017-533-1, 2017
European Planetary Science Congress 2017

First In-Situ Determination of the Ionospheric Structure of Saturn by Cassini/RPWS

J.-E. Wahlund (1), M. W. Morooka (1), L. Hadid (1), D. J. Andrews (1), W. S. Kurth (2), G. Hospodarsky (2), and A. M. Persoon (2)
(1) Swedish Institute of Space Physics, Uppsala, Sweden (jwe@irfu.se / Tel: +46-18-471 5946 / Fax: +46-18-471 5905), (2) University of Iowa, USA

Abstract

During the first close flyby of the planet Saturn by the Cassini spacecraft in its Grande Finale, the Radio & Plasma Wave Science (RPWS) sensors (including a Langmuir probe) determined the ionospheric structure of Saturn. We present the plasma density and electron temperature data from several Cassini flybys and discuss the results in light of possible theories for the interaction with the Saturn ring system and space environment.

1. Introduction

The Cassini spacecraft project is coming close to its end after many highly fruitful years in the service of planetary science. However, the end-performance will be as spectacular as the beginning with several close flybys of the majestic rings, even crossing the ring-plane inside the innermost visible ring (the D-ring), and a last tour right into the upper atmosphere and ionosphere of Saturn (Figure 1).

The Radio & Plasma Wave Science (RPWS) instrument package on board Cassini includes a Langmuir probe (LP) that is providing the first ever detailed in-situ measurements of the ionosphere of a giant gas planet (Saturn). The Cassini spacecraft will do 22 close flybys of Saturn, and during each of these the intent is to investigate its ionosphere in detail by RPWS.

In particular, the RPWS Langmuir probe will characterize the ionosphere of Saturn and how the rings affect the latitudinal structure of Saturn's upper atmosphere. It will study how the rings interact with the ionosphere close to the equatorial plane. Is there a "water rain" from the rings? RPWS will also investigate if a dense organic rich ionosphere exists at the lowest encountered altitudes.

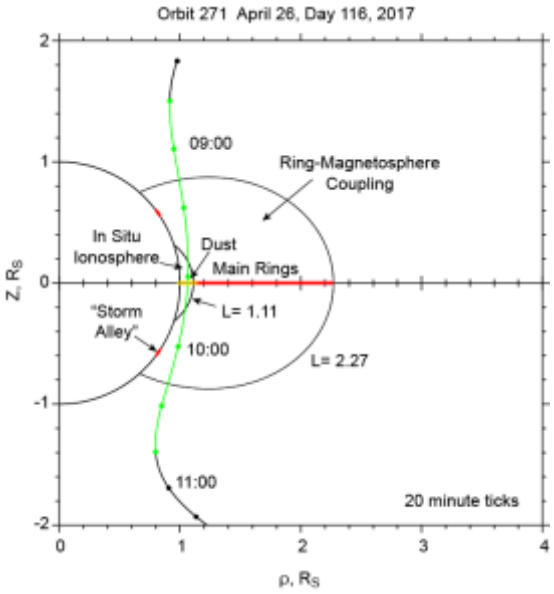

Figure 1: One Proximal orbit example with expected encountered regions (right).

The strong dipole magnetic field of Saturn is believed to facilitate a possible coupling between the rings and the atmosphere/ionosphere of Saturn [*Northrop and Hill*, 1982, 1983], serving as a ring mass pathway. The structure of the rings can therefore, along magnetic flux tubes, be reflected in the latitudinal structure of the ionosphere where the ring material, predominately water (ice), is deposited at particular latitudes and affect the local atmosphere through photochemical reactions. Cassini in the Proximal orbit phase, with its high-inclination polar orbits, will traverse through these magnetic flux tubes, and can investigate these relationships in detail.

2. Initial results

We present in this abstract the results from the first encounter (Figure 2), and when this abstract is written data from the next flyby (out of 22 flybys) is being analysed. We hope to present the full data set

at EPSC, including the last final orbit where we hope to see the ionosphere structure below the ionospheric peak of Saturn.

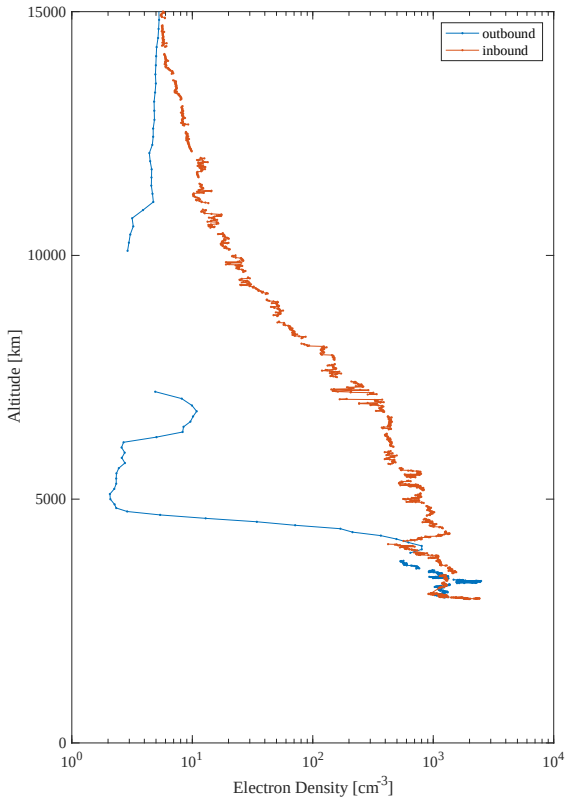

Figure 1: RPWS/Langmuir probe electron density with 20 samples/s resolution from the first flyby of Saturn, April 26, 2017.

EPSC Abstracts
Vol. 11, EPSC2017-542, 2017
European Planetary Science Congress 2017

The Interaction of Titan's Aerosols with Hydrocarbons Seas

D. Cordier (1) and N. Carrasco (2,3)
(1) Groupe de Spectrométrie Moléculaire et Atmosphérique - UMR CNRS 7331 Campus Moulin de la Housse - BP 1039 Université de Reims Champagne-Ardenne 51687 REIMS – France, (2) LATMOS, UMR CNRS 8190, Université Versailles St Quentin, UPMC Univ. Paris 06, 11 blvd d'Alembert, 78280 Guyancourt, France, (3) Institut Universitaire de France, 103, bd Saint-Michel, 75005 Paris, France

Abstract

Titan, the enigmatic large moon of Saturn, is the unique satellite of the solar system surrounded by a dense atmosphere. Thick layers of photochemical organic aerosols shroud the surface, and sediment to the ground. In polar regions, large lakes and seas of liquid hydrocarbons have been discovered by *Cassini/Huygens* mission. Aerosols sedimenting above the lakes run into a liquid surface where new interactions take place. In this wrok, we address the question of the first contact between the aerosols and the lakes: will the aerosols particles float or rapidely sink into lakes? And, we investigate the possibility of the existence of a slick formed by this organic material.

1. Introduction

Titan, the main satellite of Saturn, is the only satellite of the solar system possessing a dense atmosphere, which ground pressure is comparable to that of the Earth. However, the most striking feature of Titan is perhaps the presence, in its atmosphere, of a thick layer of haze. The *Voyager* and *Cassini/Huygens* missions have inspired many works focused on aerosols distribution and properties, and now a vast literature is available on this topic (for a review, see for instance: West et al., 2014).
Beside this, the Cassini orbiter instruments have revealed a collection of dark features dotting the polar regions of Titan (Stofan et al., 2007; Turtle et al., 2009). These geomorphological characteristics are interpreted as lakes or seas (depending on their size) of liquid hydrocarbons. These structures were found at both poles and involve diameters up to more than thousand kilometers. Since organic material produced in the atmosphere should be the subject of sedimentation to surface, and could form large depositions (Lorenz et al., 2008), the question of the interactions between the haze particles, also called "aerosols" in this paper, and the liquid hydrocarbon surface, emerges naturally. To understand the fate of the aerosols at the surface of Titan's lakes, a first parameter to be investigated is their floatability.

2. Presence of Aerosols on Titan's Seas Surface

Observations show the presence of a more or less uniform layer of haze over the entire Titan's globe. This haze has its origin in the photochemistry initiated by solar radiations. The end-products of these processes are recognized to be aggregates of organic material (Lavvas et al., 2010). Each haze particles is built by aggregation of small entities called "monomers", which, if considered to be spherical, have a radius around 50 nm (Rannou et al., 2006; Tomasko et al., 2009). One aggregate, containing several thousand monomers, has a fractal structure (Lavvas et al., 2010). Due to their fluffy structure, haze particles are coupled with the atmospheric gas, but Global Circulation Models (GCM) predict the sedimentation of dry aerosols, corresponding of about 3.3×10^{-7} m per Titan year, uniformly distributed over Titan's surface. In the case of dry aerosols, the sedimentation rate changes with latitude, reaching maxima of $\sim 10^{-5}$ m within a few degrees from poles. In addition to these particles, formed at high altitude, other "exotic snows" may be produced in the troposphere. Indeed, many organic simple species are formed by stratosphere, for instance HCN, C_2H_2, C_4H_{10}, C_6H_6, ... (Krasnopolsky, 2014) and may form crystals that could aggregate in the form of "snow grains" when falling in the troposphere. Of course, the existence of this second class of aerosols is speculated and has never been observed.
All these arguments plead for the possible presence of an aerosols deposit, at least transient, at the surface of Titan's lakes/seas.

3. The Floatability of Titan's Aerosols

Two distinct effects may be invoked when the flotability of an object is questioned: (1) the Archimedes' buoyancy, (2) the effect of surface tension. The first mentioned effect requires estimations for both aerosol monomers and Titan's seas liquid densities. The second one demands some acknowledge about the monomers density and also data concerning the values of surface tension. For a long time, the monomers are recognized to be formed by molecules harboring a large number of carbon atoms (Nna-Mvondo et al., 2013). A few articles report density measurements on Titan's aerosols laboratory analogs, the tholins. produced during laboratory experiments The bulk mass density of these analogues is around $1.3 - 1.4$ g cm^{-3}, so more than thousand kg m^{-3} (Trainer et al., 2006; Imanaka et al., 2012; Hörst & Tolbert, 2013; Brouet et al., 2016). Whatever the scenario considered for Titan's lakes composition, the density of their liquid remains around $0.5 - 0.8$ g cm^{-3}, values that impede Archimedes' buoyancy.

It is well known that small bodies heavier than the supporting liquid, including small objects made of iron, can float under the influence of the so-called capillary force. Even some animals, bugs of the familly of the *Gerridae* (water striders) take advantage of this kind of force to survive at the surface of water (Gao & Jiang, 2004). We now discuss a possible Titan's aerosols flotability driven by cryogenic liquid surface tension. We were able to determine the maximum thickness e of the aerosols layers that can be hold by sea surface

$$e \sim \frac{3\,\gamma}{r\,g_{\rm Tit}\,\rho_{\rm mono}} \qquad (1)$$

where γ is the surface tension of the liquid, r the radius of monomers, $g_{\rm Tit}$ the Titan's ground gravity and $\rho_{\rm mono}$ the density of monomers. Surprinsingly, this result does not depend on the "porosity" of the aerosols. A numerical estimate can be obtained for e, assuming typical values for involved physical quantities. Namely, we fixed the surface tension γ to 2×10^{-2} N m^{-1}, the real value depends on the precise chemical composition of the liquid, but should be around the nitrogen value. For the density of monomer material we choose 800 kg m^{-3}, value between the density of liquid methane and that of liquid water. The Titan's surface gravity is well known and equals 1.352 m s^{-2}. All this yields to $e \sim 10^3$ m, such an extremely large value, compared to the size of a monomer or even of an aerosol particle, means that the physical process, limiting the thickness of a possible aerosols slick, is not included in this crude estimation.

4. Summary

In this presentation, we will discuss the influence of factors that could limit the thickness of the organic slick, which could accumulate at the surface of Titan's sea. Perhaps more importantly, we will also investigate the physical consequences of the presence, of such a floating layer, on the properties of the sea surface.

References

Brouet, Y., Levasseur-Regourd, A. C., Sabouroux, P., et al. 2016, MNRAS, 462, S89

Flasar, F. M. 1983, Science, 221, 55

Gao, X., & Jiang, L. 2004, Nature, 432, 36

Hörst, S. M., & Tolbert, M. A. 2013, ApJL, 770, L10

Imanaka, H., Cruikshank, D. P., Khare, B. N., & McKay, C. P. 2012, Icarus, 218, 247

Krasnopolsky V.A. **2014**. *Chemical composition of Titan's atmosphere and ionosphere: Observations and the photochemical model*. Icarus 236:83–91.

Lavvas, P., Yelle, R. V., & Griffith, C. A. 2010, Icarus, 210, 832

Lorenz, R. D., Mitchell, K. L., Kirk, R. L., et al. 2008, Geophys. Res. Lett., 35, L02406

Nna-Mvondo, D., de la Fuente, J. L., Ruiz-Bermejo, M., Khare, B., & McKay, C. P. 2013, Planet. Space Sci., 85, 279

Rannou, P., Montmessin, F., Hourdin, F., & Lebonnois, S. 2006, Science, 311, 201

Stofan, E. R., Elachi, C., Lunine, J. I., et al. 2007, Nature, 445, 61

Tomasko, M. G., Doose, L. R., Dafoe, L. E., & See, C. 2009, Icarus, 204, 271

Trainer, M. G., Pavlov, A. A., Dewitt, H. L., et al. 2006, PNAS, 103, 18035

Turtle, E. P., Perry, J. E., McEwen, A. S., et al. 2009, Geophys. Res. Lett., 36, 2204

West, R., Lavvas, P., Anderson, C., & Imanaka, H. 2014, in TITAN – Interior, Surface, Atmosphere, and Space Environment, (Cambridge University Press 2014), 285

EPSC Abstracts
Vol. 11, EPSC2017-543, 2017
European Planetary Science Congress 2017

Dissolution on Titan: A Landscape Evolution Model

T. Cornet (1), B. Seignovert (2), C. Fleurant (3), D. Cordier (2), O. Bourgeois (4), S. Le Mouélic (4), S. Rodriguez (5) and A. Lucas (5).
(1) Laboratoire AIM, CEA Saclay, Gif sur Yvette, France, (2) Laboratoire GSMA, Université de Reims, Reims, France, (3) LETG, Université d'Angers, Angers, France, (4) LPG Nantes, Université de Nantes, Nantes, France, (5) IPGP, Paris, France. (thomas.f.cornet@gmail.com)

Abstract

Landforms seen in Cassini/RADAR images of Titan, as well as thermodynamics models of solid-liquid equilibrium between organics and liquid methane, indicate that dissolution can be a very active process at high latitudes. We develop a Landscape Evolution Model incorporating dissolution in the context of Titan to simulate the evolution of the surface over time. We compute synthetic radar SAR images from the synthetic landscapes that we can compare with actual Cassini/RADAR images of Titan.

1. Introduction

Saturn's major moon Titan is an Earth-like world in many aspects. Its photochemically active N_2-CH_4-rich atmosphere allows the existence of liquid hydrocarbon lakes and seas at polar latitudes [1], sometimes connected to fluvial valleys and channels at polar to tropical latitudes [2], and large dune fields close to the equator [3]. Despite many morphological similarities with the Earth landscapes, the chemistry implied in the geological processes, however, is strikingly different. Titan's cold environment (T = 90 - 94 K) only allows water to exist under the form of an icy "bedrock". The presence of methane as the second major atmospheric constituent in these cold conditions allows sustaining a hydrocarbon cycle similar to the terrestrial hydrological cycle. Finally, a plethora of organic solids, more or less soluble in liquid hydrocarbons [4], are produced in the atmosphere and fall down onto the surface over geological timescales.

Based on comparisons with terrestrial analogues, dissolution and crystallization have been suggested in various instances to take part in the landscape development on Titan [5-8]. Dissolution has been invoked, for instance, for the development of the so-called "labyrinth terrain", located at high latitudes and resembling terrestrial cockpit or polygonal karst terrain [7] (Figure 1). Here we aim at testing this hypothesis by comparing the natural landscapes visible in the Cassini/RADAR SAR images, with the results of a 3D Landscape Evolution Model (LEM) that includes dissolution as the major geological process [9].

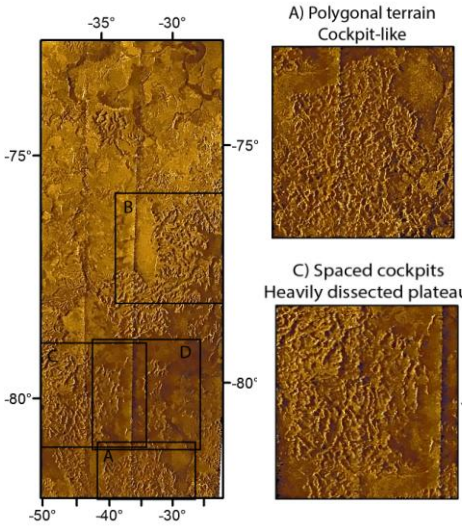

Figure 1: The Sikun Labyrinthus area on Titan seen at T39 by the Cassini/RADAR.

2. Methods

We use of the Channel-Hillslope Integrated Landscape Development (CHILD) model [10] as modified by Fleurant et al. [9] to include dissolution. Here, only dissolution and solute transport along the steepest gradient alter the initial mesh, set as a planar surface covered by a 100.0 ±0.1 m organic layer with a 50 m spatial resolution over a 25×25 km area. Four factors are tested: the dissolution rate, the diffusion rate for solute transport, and an initial "sink spatial density" designed to simulate pre-existing fractures

of the layer. Using this LEM, we are able to follow the terrain elevation over millions of years.

Cassini/RADAR SAR images are the only high resolution imagery data available, where cockpit-like landforms can be distinguished (Figure 1). To compare these SAR images of Titan's surface with the model results, we compute synthetic SAR images from the Digital Elevation Models generated with the LEM. This step is ensured by following the procedure described in Paillou et al. [11], which takes into account surface reflections of microwaves. The method is validated on natural landscapes on Jamaica where cockpits are seen in SRTM elevation data and SAR Sentinel1 data.

3. Preliminary Results

We take into account the dissolution rate of a surface organic layer whose bulk composition is given by the relative abundance of organic solids produced by photochemistry in the atmosphere [12] and accumulated at the surface, as computed in Cornet et al. [4]. These deposits are exposed to methane precipitation rates given by Schneider et al. [13] at high latitudes (P ~ 8 m/Tyr), which leads to a dissolution rate on the order of $DR = 10^{-4}$ m/Tyr [4], converted into a dimensionless dissolution rate $K_X = DR/P \sim 10^{-5}$. The incidence angle for the SAR image simulation is that of the T39 SAR swath, where Sikun Labyrinthus has been observed. The dielectric constant of the ground corresponds to that of tholins [14].

We first studied the influence of the LEM parameters. Dissolution triggers the erosion of the landscape. Hillslope diffusion spreads the deformation and has a strong influence on the shape of the remnant hills. Both terms (especially dissolution), have a strong influence on the total time to erode the landscape. The number of sinks has no influence on the final landscapes. Figure 2 shows an example output after 8 Myr of erosion of a quasi-flat surface and the SAR image derived from the modelled topography. Despite a lack of preferred orientation of radar reflectors in our SAR simulated images, some similarities can be seen between the synthetic and actual SAR images in the areas of the polygonal terrain to residual hills (Figure 1), especially if the landscape has been exposed to several millions of years of chemical erosion (> 5 Myr in our simulations). This allows the facets to be spaced by a few km, such as for the polygonal and isolated ridges on Figure 1.

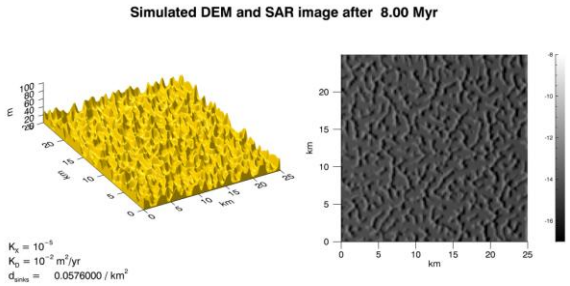

Figure 2: Snapshot of the landscape evolution by dissolution and solute transport taken after 8 Myr with a dissolution rate of 10^{-5} and a diffusion coefficient of 10^{-2} m^2/s. **Left:** Digital Elevation Model from the LEM. **Right:** synthetic SAR images generated from the DEM (illumination from the left).

4. Summary and Conclusions

We are able to produce landscapes formed by dissolution under Titan's surface conditions. These DEMs are used to produce synthetic SAR images of the surface in order to compare the modelled landscapes with the actual Cassini/RADAR SAR images of Titan. Similarities are seen between simulated and actual SAR images, which suggests that the landscapes generated could explain the patterns observed in Cassini data. Further work will include the statistical analysis of the modelled landscapes in order to infer possible quantitative information about Titan's high latitude terrain.

Acknowledgements

TC is funded by the CNES Research Fellowship programme. The authors also acknowledge financial support by the LabEx UnivEarthS.

References

[1] Stofan E. et al (2006), Nature. [2] Langhans M. et al. (2013), Icarus. [3] Lucas A. et al. (2016), GRL. [4] Cornet T. et al. (2015), JGR. [5] Lorenz R. et al. (2009), PSS. [6] Cornet T. et al. (2012), Icarus. [7] Malaska M. et al. (2010), LPSC. [8] Barnes J.W. et al. (2011), Icarus. [9] Fleurant C. et al. (2008), Geomorph., Rel., Proc., Envir. [10] Tucker G. et al. (2001), Computers Geosciences. [11] Paillou Ph. et al. (2016), Icarus. [12] Krasnopolsky V. (2009), Icarus. [13] Schneider T. et al. (2012), Nature. [14] Rodriguez S. et al. (2003), Icarus.

EPSC Abstracts
Vol. 11, EPSC2017-562, 2017
European Planetary Science Congress 2017

Wind measurements in Saturn's atmosphere with UVES/VLT ground-based Doppler velocimetry

M. Silva (1), P. Machado (1), A. Sánchez-Lavega (3), R. Hueso (3), S. Pérez-Hoyos (3), J. Peralta (2) and D. Luz (1)
(1) Institute of Astrophysics and Space Sciences, Observatório Astronómico de Lisboa, Ed. Leste, Tapada da Ajuda 1349-018 Lisboa, Portugal (msilva@oal.ul.pt), (2) Institute of Space and Astronautical Science – Japan Aerospace Exploration Agency (JAXA), Japan, (3) Departamento de Física Aplicada I, E.T.S. de Ingeniería, Universidad del País Vasco, Bilbao, Spain

Abstract

We will present final Doppler wind velocity results of Saturn's zonal flow at cloud level. Our aim is to study the planet's global system of winds at the 70 mbar region, to help constraining the characterization of the equatorial jet and the latitudinal variation of the zonal winds, to measure its spatial and temporal variability and to contribute to monitor the variability in order to achieve a better understanding of the dynamics of Saturn's zonal winds, which Sánchez-Lavega et al. (2003, Nature, 423, 623) have found to have changed strongly in recent years. They have reported a decrease of 200 m/s of the speed of Saturn's equatorial zonal jet from 1996 (450 m/s) to 2002 (250 m/s), as the planet approached southern summer solstice. Finally, the complementarity with Cassini, whose "grand finale" is planned for September this year, will provide an independent set of observations to compare with and help validate the method.

1. Introduction

The UVES/VLT instrument has been used, which simultaneously achieves high spectral resolving power and high spatial resolution. The field has been derrotated in order to have the aperture aligned perpendicularly to Saturn's rotation axis. In this configuration, spatial information in the East-West direction is preserved in a set of spectra in the direction perpendicular to the dispersion.

1.1 Theoretical basis

The technique of Absolute Accelerometry (AA, Connes, 1985, ApSS 110, 211) has been applied to the backscattered solar spectrum in order to determine the Doppler shift associated with the zonal circulation. Our measurements have been made in the wavelength range of 480-680 nm. Previously we successfully adapted this Doppler velocimetry technique for measuring winds at Venus cloud tops (Machado et al. 2012, 2014, 2017). In the present study we will show the adaptation of the method for Saturn's case. Since the AA technique only allows to compare spectra where the line shifts are within the line width, in fast rotating atmospheres (such as Saturn) the spectra must be compared by pairs from adjacent areas of the disk (adjacent pixels in the slit). We will use coordinated observations from the Cassini's Visible and Infrared Mapping Spectrometer (VIMS), in order to compare with the Doppler winds obtained from the UVES/VLT high-resolution spectra.

2. Observation settings

The observations consisted of 4 blocks of 15 exposures of 90 seconds, plus two shorter blocks of 9 exposures, totaling 7.3 hours of telescope time. In order to cover the whole disk, the aperture has been offset by 1 arcsec in the North-South direction between consecutive exposures. Unfortunately, most of the northern hemisphere was covered by the rings. Saturn's diameter was 17.4 arcsec and the slit aperture was 0.3 x 25 arcsec. The two shorter observation blocks of 9 exposures only covered the central part of the disk. The sub-terrestrial point was at -26.1°S. The presence of the rings led to severe order superposition. The dark region between the rings and the disk may not be present, depending on the slit position. On the other hand, defects in the response of the UVES slit in the upper part preclude its use for accurate Doppler measurements such as these. For these reasons only the central part of the aperture has been considered for the measurements.

3. Summary and Conclusions

The Doppler velocimetry is currently the only ground-based technique able to derive instantaneous wind's velocities, allowing cross-comparison with cloud-tracked winds from Cassini VIMS images, and the study of short-term variability.

This is still an ongoing work, on the next steps we will obtain the zonal wind as a function of local time for all slit's offset positions, except for the cases with ring overlapping. For that we will estimate the ring system keplerian velocity at each pixel position, and then, superpose the planet + rings spectra and adjust the most spectral lines possible (the residual components will be due to methane contribution).

We will separate the spectra contribution from methane (and also ammonia) and study the altitude from its contribution. Detection of finer latitudinal variations in zonal winds in the future will require precise modeling (radiative transfer model) of the probed level and an improved treatment of methane lines (and NH_3 as well) and order superposition effects. However, our Doppler velocimetry technique stands out as a promising ground-based method for wind monitoring in the giant planets.

Acknowledgements

This work was supported by FCT (ref. UID/FIS/04434/2013) through national funds and by FEDER through COMPETE2020 (ref. POCI-01-0145-FEDER-007672).

References

[1] Connes, P. 1985, Absolute astronomical accelerometry, Astrop. Sp. Sci., 110, 211-255.

[2] García-Melendo et al., 2012, Non-linear simulations of Saturn's 2010 Great White Spot, European Planetary Science Congress 2012, id. EPSC2012-298.

[3] Luz D. et al., 2006, J. Geophysics. Res. Planets 111, E08S90.

[4] Machado P. et al., 2012, Icarus, 221, 248-261.

[5] Machado P. et al., 2014, Icarus, 243, 249-263.

[6] Machado P. et al., 2017, Icarus, 285, 8-26.

[7] Peralta, J., Sánchez-Lavega, A., Valverde, D., Luz, D., Machado, P., 2015, GRL.

[8] Sánchez-Lavega, A., et al., 2003, A strong decrease in Saturn's equatorial jet at cloud level, Nature, 423, 623-625.

[9] Widemann, T., Lellouch, E., Donati, J.-F., 2008, Planet. Sp. Sci., 56, 1320-1334.

[10] Patrick Irwin (Oxford University) private communication.

EPSC Abstracts
Vol. 11, EPSC2017-585-1, 2017
European Planetary Science Congress 2017

Langmuir waves observed in planetary foreshocks by Cassini: From the beginning to the Grand Finale

D. Píša (1), W. S. Kurth (2), G. B. Hospodarsky (2), D. A. Gurnett (2), O. Santolík (1,3), and J. Souček (1)
(1) Institute of Atmospheric Physics, Czech Academy of Sciences, Prague, Czech Republic (dp@ufa.cas.cz), (2) University of Iowa, Iowa City, Iowa, USA, (3) Charles University, Prague, Czech Republic

Abstract

We present a review of Langmuir wave observations across planetary foreshocks obtained by the Cassini spacecraft. During its seven year journey to Saturn, Cassini made flybys of Venus (April 1988 and June 1999), Earth (August 1999), and Jupiter (December 2000). The spacecraft arrived to Saturn in July 2004. Since then Cassini orbits Saturn with many foreshock visits. Almost 20-year-long mission provides an unique opportunity to study and compare Langmuir wave properties across the solar system. Using the Radio and Plasma Wave Science (RPWS) instrument, we examine measurements from a foreshock of each of four visited planets. The Langmuir wave observations are compared and peak electric field amplitudes are estimated. The Langmuir wave properties as a function of the foreshock position for each of flybys are also discussed.

1 Introduction

Langmuir waves are a typical emission observed in a region ahead of planetary shocks. Solar wind electrons accelerated at the shock front are reflected back into the solar wind forming electron beams, which stream along the solar wind magnetic field lines. In regions with electron beams, usually called the electron foreshock, the electron distribution is unstable and electrostatic Langmuir and beam-mode waves are generated via the beam instability (e.g., [1]). The processes of generation and evolution of electrostatic waves depend strongly on the solar wind plasma conditions and on the position inside the foreshock. In a relatively narrow region behind the sunward foreshock boundary, Langmuir waves are the most intense and they are usually observed as the narrowband emission with single peak spectra at a frequency close to the electron plasma frequency (Fig. 1). More complex waves exhibiting a wide frequency spread are often observed deeper downstream (e.g. [3]).

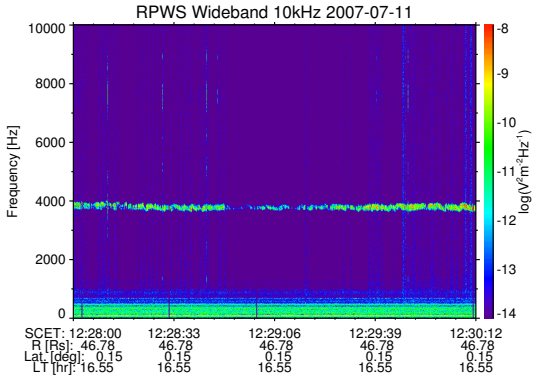

Figure 1: Time-frequency spectrogram for the RPWS/WBR electric component with the Langmuir wave emission observed inside Saturn's foreshock.

2 Instrumentation

For the purpose of this review data from the Radio and Plasma Wave Science (RPWS) and the Magnetometer (MAG) instruments on board the Cassini spacecraft were used. The RPWS instrument consists of three electric antennas, a triaxial search coil magnetometer, and five specialized receivers (for more details see [2]). The receivers cover a range from 1 Hz to 16 MHz for the electric fields and up to 12 kHz for the magnetic fields. Because the Langmuir wave peak frequency is different at each of four planet, the high frequency receiver (HFR) data are used for the Venus and Earth flybys, and the medium frequency receiver (MFR) data are used at Jupiter and Saturn. For a long-term survey inside the Saturnian foreshock, the Wideband receiver (WBR) data are also taken. The HFR A-C subbands cover a frequency range from 3.5 to 319 kHz. MFR provides intensity measurements from a single selected antenna over a frequency range from 24 Hz

to 12 kHz. The WBR lowband covers the same frequency range, but provides irregular waveform snapshots. The strength and direction of the interplanetary magnetic field were obtained from the triaxial fluxgate magnetometer which is a part of the MAG instrument.

3 Observations

Due to instrumental settings there are no Langmuir wave observations during the first Venus flyby (April 1998). During the second Venus flyby (June 1999), the RPWS observed the intense Langmuir wave emission with an estimate amplitude on the order of mVm^{-1}, which is similar to the peak amplitude detected by Pioneer Venus and Galileo.

Cassini performed one gravity assist flyby of Earth in August 1999. During this flyby, RPWS observed the intense Langmuir waves at frequencies below 20 kHz in the vicinity of the bow shock. Further from the bow shock less intense emission at the same frequencies was also detected. The largest Langmuir wave electric field detected by Cassini during this flyby was below mVm^{-1}. This amplitude is smaller as compared to measurements of other spacecraft
(e.g. $> 10^2\,\mathrm{mVm}^{-1}$ as measured by STEREO).

In December 2000, Cassini had a flyby of Jupiter. RPWS measured the narrowband emission at frequency of about 2 kHz. The amplitude of the Langmuir waves at this frequency band was on order of $10^{-1}\,\mathrm{mVm}^{-1}$.

After the Saturn Orbit Insertion in July 2004, Cassini spent more than 500 days in front of Saturn's bow shock. Using the RPWS/Wideband receiver, almost 10^6 waveform snapshots (Fig. 2) with the intense Langmuir wave emission were identified. Typical Langmuir wave amplitudes were observed in the range from 10^{-2} to $1\,\mathrm{mVm}^{-1}$ with the median wave amplitude of $8 \times 10^{-2}\,\mathrm{mVm}^{-1}$ [4]. The most intense waves were observed in the vicinity of the foreshock sunward boundary. The amplitudes then fall off with increasing depth in the downstream region.

4 Summary

Langmuir waves have been detected by the Cassini/RPWS instrument upstream of the bow shock of each planet Cassini visited. The characteristics of the Langmuir waves are similar at each planet, with the main difference being the frequency of the waves due to the decrease in the solar wind density

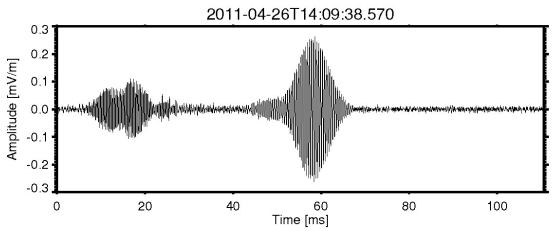

Figure 2: Example of the RPWS/WBR waveform snapshot with typical Langmuir wave packets observed inside Saturn's foreshock.

with distance from the Sun. The Langmuir waves have similar spectral characteristics at each planet. Near the sunward foreshock boundary crossings, the Langmuir waves are found to be intense, narrowband emissions near the electron plasma frequency. The Langmuir waves often show spectra that are up- and/or down-shifted in frequency from the plasma frequency deeper in the foreshock, very similar to previous observations by other spacecraft.

Acknowledgements

The work has been supported by NASA through contract 1415150 with the Jet Propulsion Laboratory, from grant P209/16/16050Y of the Grant Agency of Czech Republic.

References

[1] Scarf, F. L., R. W. Fredricks, L. A. Frank, and M. Neugebauer (1971), Nonthermal electrons and high-frequency waves in the upstream solar wind, 1. Observations, J. Geophys. Res., 76, 5162–5171

[2] Gurnett, D., et al. (2004), The Cassini radio and plasma wave investigation, Space Sci. Rev., 114 (1-4), 395–463

[3] Píša, D., O. Santolík, G. B. Hospodarsky, W. S. Kurth, D. A. Gurnett, and J. Souček (2016), Spatial distribution of Langmuir waves observed upstream of Saturn's bow shock by Cassini, J. Geophys. Res. Space Physics, 121, 7771–7784,

[4] Píša, D., G. B. Hospodarsky, W. S. Kurth, O. Santolík, J. Souček, D. A. Gurnett, A. Masters, and M. E. Hill (2015), Statistics of Langmuir wave amplitudes observed inside Saturn's foreshock by the Cassini spacecraft, J. Geophys. Res. Space Physics, 120

EPSC Abstracts
Vol. 11, EPSC2017-603, 2017
European Planetary Science Congress 2017

Position of planet X obtained from motion of near-parabolic comets

Yu. D. Medvedev (1), D. E. Vavilov (1)
(1) Institute of Applied Astronomy of the Russian Academy of Science, St. Petersburg, Russia (medvedev@iaaras.ru)

Abstract

Batygin and Brown [1] proposed that a planet with 10 earth's mass and an orbit of 700 AU semi major axis and 0.6 eccentricity can explain the observed distribution of Kuiper Belt objects around Sedna.We used near-parabolic comets for determination of the planet's position on the orbit. Assuming that some comets approached the planet in the past, we made a search for the comets with low Minimum Orbit Intersection Distance (MOID) with the planet's orbit. We considered two cases of the planet's motion: the direct and the inverse ones.

1. Introduction

The paper by Batygin and Brown [1] has provided a powerful stimulus for the studies devoted to proving the existence of massive celestial bodies in the Edgeworth–Kuiper belt. The authors of this paper show that the unusual distribution of the orbits of discovered celestial bodies in this belt can be explained by the gravitational influence of a hypothetical planet X with a mass of 10 Earth masses moving in an elliptical orbit with a semimajor axis a = 700 AU, eccentricity e =0.6, and the following angular elements: orbital inclination i =30°, argument of perihelion $\omega = 150°$, and longitude of ascending node $\Omega = 293°$. Below we will refer to this orbit as the reference one. This paper was followed by the paper of Fienga et al. [2], where the most probable ranges of the planet's positions in its reference orbit were determined, and the position was improved in this paper based on Cassini observations. The results of the paper [2] show that the presence of a planet in the reference orbit is possible, but the uncertainty in the planet's ephemeris position still remains fairly large. Therefore, improving the planet's position in its reference orbit remains a topical problem. In this paper we attempt to improve the sixth element of this planet (the planet's position in its orbit) at fixed remaining five elements whose values were given above. We use nearly parabolic orbits as indicators that allow the planet's position to be improved.

2. Method

Our main assumption is that some of the nearly parabolic comets had a close encounter with this hypothetical planet and may have been thrown into the inner Solar system as a result of precisely this encounter. Separating out such comets from the general list of known comets and estimating the times of their encounters with the hypothetical planet enable us to improve its position in the orbit. The encounter must immediately precede the discovery of such comets, i.e., we must be able to identify the comets that made less than one revolution around the Sun from the time of encounter to discovery; otherwise the time of encounter becomes uncertain. Therefore, comets moving in hyperbolic orbits are of special interest to us; the MOID point must occur on the descending branch of the hyperbola of the comet's orbit, because a "proper" sequence of events is possible only in this case: its encounter with the planet, its motion in a hyperbolic orbit into the inner Solar system, and its discovery at perihelion.

3. Calculations

We took all the known nearly parabolic comets (having orbits with eccentricities e < 0.99), a total of 2689 comets. Then, we excluded the comets with a low accuracy of their elements from the list of these comets. These primarily include the sungrazing comets with very short arcs of observations and the comets that were observed before January 1, 1800, and have a low accuracy of observations. There were 768 comets satisfying the accuracy conditions. Table provides data on the three selected comets having hyperbolic orbits and MOIDs with the planet on the

descending branch. It contains “Designation” is a preliminary designation of the comet; e is the orbital eccentricity of the comet and its error (five digit of e and the error of e expressed in the same digits are given in parentheses); MOID is the minimum orbit intersection distance between the comet and the hypothetical planet in AU.

Table: Parameters of three selected comets

Designation	e	MOID
C/1999 N4	1.000(50±1)	0.44
C/2002 Q5	1.000(04±0.2)	7.87
C/2000 K1	1.000(25±2)	7.50

We calculated the heliocentric distance, right ascension, declination, true anomaly, and time of perihelion passage by the planet using the assumption that the selected comets had close encounters.

4. Summary and Conclusions

We considered two cases of the planet’s motion: the direct and the inverse ones. In case of the direct motion the true anomaly of the planet lies in interval [176°, 182°] and, thus, the right ascension, the declination and geocentric distance of the planet are in intervals [83°, 88°], [8°,10°], and [1115, 1120] AU, correspondingly. In case of the inverse motion the true anomaly is in [212°, 223°] and the other values are in intervals [48°, 55°], [-12°,-8°] and [800, 880] AU. For comparison with the direct motion the true anomaly for the inverse motion, υ, should be transformed by 360°-υ. That gives us the interval [137°, 140°] that belongs to the intervals of the true anomaly of possible planet’s position given by Fienga et al. [2] and Holman and Payne [3].

Acknowledgements

This work is supported by the Russian Scientific Foundation (project No 16-12-00071).

References

[1] Batygin K., E. Brown M. E.: Evidence for a distant giant planet in the solar system, Astronomical Journal, Vol. 151, pp. 22–34, 2016.

[2] Fienga A., J. Laskar, H. Manche, and M. Gastineau.: Constraints on the location of a possible 9th planet derived from the Cassini data, Astronomy & Astrophysics, Vol. 587, L8, 2016.

[3] Holman M. J. and Payne M. J.: Observational constraints on planet nine: Cassini range observations, Astronomical Journal, Vol. 152, pp. 94–113, 2016.

EPSC Abstracts
Vol. 11, EPSC2017-636, 2017
European Planetary Science Congress 2017

Cation Chemistry in Titan's Upper Atmosphere and its Influence on Tholin Formation

D. Dubois (1), N. Carrasco (1,2), L. Jovanovic (1,3) and L. Vettier (1)
(1) LATMOS, Université de Versailles St-Quentin, Guyancourt, France (2) Institut Universitaire de France, Paris, France
(3) Spectroscopies et Analyses chimiques dirigées vers le Vivant, Université Paris Descartes, Paris, France

Abstract

Titan is Saturn's largest satellite. This object is unique in the solar system as it hosts a dense atmosphere [1] mainly made of molecular nitrogen N_2 and methane CH_4, with a surface pressure of 1.5 bar. The nitrogen-rich atmosphere and the presence of liquid areas on the surface make it one of the most interesting nearby objects to understand the evolution of the primitive Earth before the emergence of life and to look for habitable environments in the solar system. The Cassini-Huygens Mission has been probing Titan since 2004. It has revealed an intense atmospheric photochemistry initiated by the photo-dissociation and ionization of N_2 and CH_4 [2]. Photochemistry on Titan leads to the formation of solid organic aerosols responsible for a smog permanently surrounding the moon [2,3]. In the upper atmosphere, Cassini detected signatures compatible with the presence of heavily charged molecules which are precursors for the solid core of the aerosols [4,5,6]. These observations indicate that ion chemistry has an important role for organic growth. However, the processes coupling ion chemistry and aerosol production are mostly still unknown. In this study, we investigate the cation chemistry, responsible for the organic growth that we observe in Titan's upper atmosphere, simulated using the PAMPRE plasma reactor [7]. Positive ions are investigated by *in situ* ion mass spectrometry in a dusty cold plasma, alongside neutral products additionally studied through infrared absorption spectroscopy and mass spectrometry.

1. Introduction

In Titan's upper atmosphere (Figure 1), Cassini's Ion and Neutral Mass Spectrometer (INMS) detected neutral and positive ion signatures [2]. Subsequently, the Cassini Plasma Spectrometer electron spectrometer (CAPS-ELS) unveiled the existence of negative ion-molecules well over the detection range of INMS ($> 100\ amu$) consistent with the presence of heavy molecules (over 10,000 Da. in mass) which are precursors for the solid core of the aerosols. This *in situ* observation unveiled for the first time the key role of heavy charged molecules (ions) initiated in the ionosphere. Thus, the ion chemistry in this organic mixture is thought to be anything but negligible. Furthermore, the gas-to-solid conversion at these high altitudes coexists in a fully coupled ionic and neutral chemistry. However, the processes coupling ion chemistry and aerosol production are at the moment mostly unknown. Experimental simulations as well as ground-based observations should help in constraining the wide population of cations.
The complexity of this material is already foreshadowed by the intricacies of the gas phase chemistry, acting as a precursor to the aerosol formation. Hence, the ion chemistry remains an open question for the characterization of the gas phase and chemical pathways leading to the formation of aerosols.

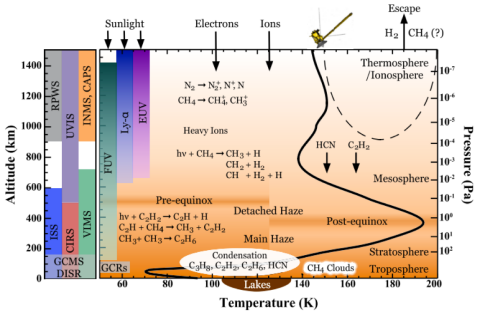

Figure 1: Titan temperature profile, the major chemical processes and approximate altitudinal coverage of the instrument suite onboard the Cassini spacecraft [8]. The coupled neutral-ion chemistry is initiated in the upper atmosphere ($< 1,000$ km).

2. Experimental Setup

We use the cold dusty plasma reactor PAMPRE [7] and Figure 2, in order to simulate Titan ionosphere conditions, at different initial CH_4 conditions.

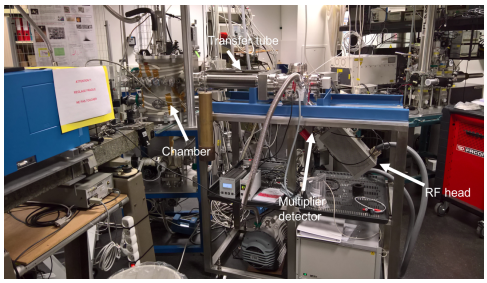

Figure 2: PAMPRE, with its ion mass spectrometer. The entrance aperture to the spectrometer measures ions within the chamber relatively close to the plasma, in order to avoid any contamination from the reactor walls.

We investigate the influence of initial CH_4 concentrations and distance of measurements on the cation population detectable with this setup. Furthermore, we compare our results with Cassini-INMS data to constrain and characterize our cation chemistry. Moreover, we provide analysis for heavy cations ($> 100\ amu$), outside of the INMS range.

3. Summary and Conclusions

With the coming end of the Cassini Mission, laboratory analyses of Titan simulations coupled with ground-based observations will be necessary in order to constrain our understanding of gas phase neutral, ion, and solid-state chemistry relevant to its atmosphere.

Our results show a strong dependency on the initial CH_4 concentration. We also monitor the evolution of key ion-molecules such as $HCNH^+$, $CH_2NH_2^+$, $C_3H_3^+$ and HC_3NH^+ suspected of being significant in Titan's upper atmosphere and thus in aerosol formation.

Acknowledgements

We are grateful to the European Research Council's Starting Grant PRIMCHEM, and the ATMOSIM experimental platform at LATMOS.

References

[1] Kuiper, 1944, Titan: a Satellite with an Atmosphere

[2] Waite et al., 2007, The Process of Tholin Formation in Titan's Upper Atmosphere

[3] Lavvas et al., 2011, Condensation in Titan's atmosphere at the Huygens landing site

[4] Cravens et al., 2006, Composition of Titan's ionosphere

[5] Crary et al., 2009, Heavy ions, temperatures and winds in Titan's ionosphere: Combined Cassini CAPS and INMS observations

[6] Wellbrock et al., 2013, Cassini CAPS-ELS observations of negative ions in Titan's ionosphere: Trends of density with altitude

[7] Szopa et al., 2006, PAMPRE: A dusty plasma experiment for Titan's tholins production and study

[8] Horst et al., 2017, Titan's Atmosphere and Climate

EPSC Abstracts
Vol. 11, EPSC2017-705, 2017
European Planetary Science Congress 2017

Present and future tectonics of Enceladus

Leszek Czechowski
University of Warsaw, Faculty of Physics, Institute of Geophysics, ul. Pasteura 7, 02-093 Poland (lczech@op.pl Fax: +48-22-5546882)

Abstract

Enceladus, a satellite of Saturn, is the smallest celestial body in the Solar System where volcanic activity is observed. It is concentrated in the South Polar Terrain (SPT) where the mass is ejected into space with the rate ~200 kg/s. We follow here our previous suggestions that this mass loss is a main driving mechanism of the Enceladus tectonics.

1. Introduction

Every second, the mass of ~200 kg is ejecting into space from the South Polar Terrain (SPT) of Enceladus [1, 2, 3, 4, 5, 6].

The loss of matter from the body's interior should lead to global compression of the crust. Typical effects of compression are: thrust faults, folding and subduction. However, such forms are not dominant on Enceladus. In previous presentations we propose here special tectonic model that could explain this paradox [6, 7] and Fig. 1.

The volatiles escape from the hot region through the fractures forming plumes in the space. The loss of the volatiles results in a void and motion of matter into the hot region to fill the void *in statu nascendi*. The motion includes – Fig. 1: (i) subsidence of the 'lithosphere' of SPT, (ii) flow of the matter in the mantle, (iii) motion of plates adjacent to SPT towards the active region.

If emerging void is being filled by the subsidence of SPT only, then the velocity of subsidence is ~0.05 $mm \cdot yr^{-1}$ [6, 7].

Note that in this model the reduction of the crust area is not a result of compression but it is a result of the plate sinking. Therefore the compressional surface features do not have to be dominant.

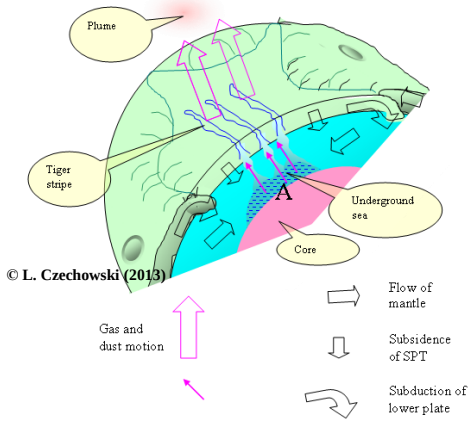

Figure 1: A scheme of suggested processes in the activity center (after [7]).

In 2014 [7] presents results of experimental modelling. Fig. 2 gives the map of the STP (left hand part of the figure). One can see the low polygonal region surrounded by the characteristic 'arcs'. In the laboratory model we observe the results of sinking the regular pentagonal plate (model of STP) in viscoelastic material. Rheology of this material corresponds to assumption that icy plates are warm enough for creeping. The right hand side of the Fig. 2 presents the situation 150 hours after beginning of sinking. The most of the plate is already covered by the material – the size of the plate is given by the yellow double arrow. Note 'kinks', that are formed above vertices of the plate. Contrary to expectations (the viscoelastic material behaves like the fluid for the considered time scale) these 'kinks' appear to be stable features.

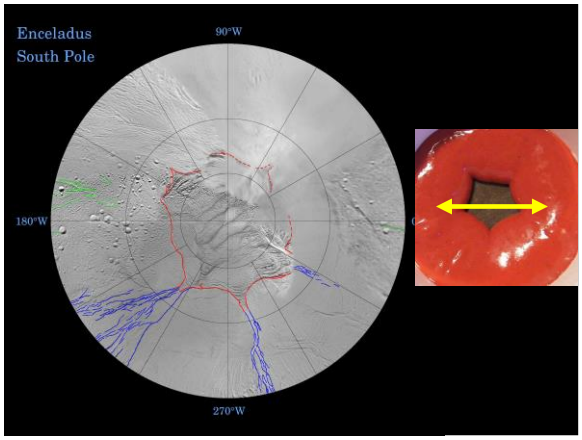

]Figure 2. The image of STP (left hand side, after NASA). Model of subsidence is on the right part of the figure. (after [7]).

3. Numerical model of subsidence

The numerical model of suggested process of subsidence is improved. It is still based on the typical set of equation: Navier-Stokes equation for incompressible viscous liquid, equation of continuity and equation of heat conduction. The Newtonian and non-Newtonian rheology could be used. Thermal convection also could be included. The preliminary results (without thermal convection) indicate that the subsidence rate of ~0.04 $mm \cdot yr^{-1}$ is possible if we assume Newtonian rheology (i.e. for n=1). For ice the non-Newtonian rheology (with n=2.5-4) however is more probable. In this case the subsidence rate is substantially lower ~0.02 $mm \cdot yr^{-1}$ but the velocity of motion of the 'mantle' material is higher.

If thermal convection is included the results could be substantially different. Note that even the direction of the plates' motion could be different. Intensive thermal convection could force adjacent plates to move into or out of the SPT. More numerical simulations are necessary to achieve better understanding of the true processes below SPT..

4. Evolution of tectonics

Our hypothesis is a natural consequence of observed mass loss. This mass loss is a main factor driving tectonic motions. Of course, it does not exclude some form of solid state convection in the icy mantle, but in fact this convection is not needed for the observed activity.

The time of operation of present form of tectonics is not known. We believe that it is a periodic process. There are some traces that could be attributed to past active centers similar to the present STP. Moreover, the ovoid-shaped depression down to 2 km deep, of size 200×140 km with the center at 200E, 15S is a good candidate [6, 7] for the future center of activity. The depression could indicate the partial melting of the mantle. It could lead to an increase of tidal heating and consequently formation of the center of activity.

Acknowledgements

We are grateful to the ICM.

References

[1] Spencer, J. R., *et al*. Enceladus: An Active Cryovolcanic Satellite, in: M.K. Dougherty et al. (eds.), *Saturn from Cassini-Huygens*, Springer Science, (2009), p. 683.

[2] Kargel, J.S. Enceladus: Cosmic gymnast, volatile miniworld. *Science* 311, 1389–1391 (2006).

[3] Langenberg, H., Planetary science: Jets of mystery *Nature Geoscience* 1, 816 (2008) doi:10.1038/ngeo373.

[4] Giese, B., and the Cassini Imaging Team. The topography of Enceladus. *EPSC Abstracts* Vol. 5, EPSC2010-675 (2010).

[5] Kargel, J.S. Enceladus: Cosmic gymnast, volatile miniworld. *Science* 311, 1389–1391 (2006).

[6] Czechowski, L. (2014) Planet. Sp. Sc. 104, 185-199

[7] Czechowski, L., Enceladus - the vanishing satellite presenting in EGU 2014, Vienna.

EPSC Abstracts
Vol. 11, EPSC2017-736, 2017
European Planetary Science Congress 2017

Cassini INMS Measurements of Saturn's Atmosphere

J. Hunter Waite (1) and the INMS Science Team
(1) Southwest research Institute, San Antonio, Texas, USA, 78015 (hwaite@swri.edu)

Abstract

The first flyby of the Cassini Proximal orbit phase has just completed at the time of this abstract submission. Although, the Ion Neutral Mass Spectrometer (INMS) was largely shielded behind the high gain antenna of the spacecraft during this flyby it could peak around the edge just enough to see a healthy and robust atmosphere from Saturn. Therefore, the prediction is that the INMS team will have a great atmospheric data set that can be compared to models at the time of the meeting.

Acknowledgements

The team Acknowledges support from a NASA JPL subcontract for support of the Cassini Ion Neutral Mass Spectrometer Investigation.

EPSC Abstracts
Vol. 11, EPSC2017-762, 2017
European Planetary Science Congress 2017

Seasonal radiative modeling of Titan's stratospheric temperatures at low latitudes

B. Bézard (1), S. Vinatier (1) and R. K. Achterberg (2)
(1) LESIA, Observatoire de Paris, France (bruno.bezard@obspm.fr), (2) University of Maryland, USA

Abstract

We have developed a seasonal radiative model of Titan's stratosphere to investigate the time variation of temperatures in the 0.2-4 mbar range as observed by the Cassini/CIRS spectrometer. The model incorporates gas and aerosol vertical profiles derived from Cassini/CIRS and Huygens/DISR data to calculate the heating and cooling rate profiles as a function of time and latitude. At 6°N around Spring equinox, the radiative equilibrium profile is warmer than the observed one at all altitudes. Adding adiabatic cooling in the energy equation, with a vertical upward velocity profile quasi-constant in pressure coordinates below the 0.03-mbar level (corresponding to ~0.3 mm s^{-1} at 1 mbar) allows us to reproduce the observed profile. The model shows that the change in insolation due to the orbit eccentricity can explain the observed 4-K decrease in equatorial temperatures around 1 mbar since 2009. At 30°N and S, the radiative model predicts seasonal variations of temperature larger than observed, pointing to latitudinal redistribution of heat by dynamics. We show that a seasonal modulation of adiabatic cooling/heating is needed to reproduce the temperature variations observed from 2004 to 2016 between 0.2 and 4 mbar.

1. Introduction

Due to Saturn's obliquity of 26.7°, Titan experiences large seasonal variations of insolation. The 0.056 eccentricity of Saturn's orbit adds a significant modulation to this insolation. The Cassini Composite Infrared Spectrometer (CIRS) aboard Cassini allows us to monitor the thermal structure of Titan's stratosphere since July 2004. The goal of this work is to investigate the heat balance of Titan's stratosphere at mid-latitudes (30°S-30°N) using a seasonal radiative model based on measurements by Cassini/CIRS and Huygens/DISR of the distributions of the radiative agents.

2. Observations

Titan's temperature field is retrieved using nadir and limb observations of the ν_4 band of methane through Focal Plane FP4 of Cassini/CIRS covering the interval 1050-1495 cm^{-1}. (e.g. [1]). In our analysis, we used temperatures retrieved at 0.2, 0.5, 1, 2 and 4 mbar, which cover the range of maximum temperature information and we restrained our analysis to equatorial and mid-latitudes between 2004 and 2016. We also compared our model to a "reference" profile retrieved from Cassini/CIRS at 6°N around equinox [6] above the ~5-mbar region and based on Huygens/HASI measurements [4] below that level.

3. Seasonal radiative model

We solve for the energy equation:

$$\frac{\partial T(z)}{\partial t} = h(z) - c(z) - w(z)\left(\frac{g(z)}{c_p} + \frac{\partial T(z)}{\partial t}\right) \qquad (1)$$

$h(z)$ is the solar heating rate equal to $-\frac{g}{c_p}\frac{dF_*(p)}{dp}$, where F_* is the downward solar flux, $c(z)$ is the cooling rate equal to $-\frac{g}{c_p}\frac{dF_{IR}(p)}{dp}$ with F_{IR} being the upward thermal emission flux, w the downward vertical velocity, C_p the specific heat capacity, and g the acceleration of gravity.

To model the radiative cooling and heating rates, we used vertical profiles of haze extinction from Huygens/ DISR in situ measurements [3] for the visible and near-IR regions, and Cassini/CIRS limb spectra near 20°S in 2007 [6] in the thermal infrared range. The methane profile is that derived from Huygens/GCMS data [5] and vertical profiles of hydrocarbon and nitriles were taken from the above-mentioned analysis of Cassini/CIRS measurements [6].

4. Results

Figure 1 shows our model prediction for 6°N in mid 2009, assuming no adiabatic heating/cooling (i.e. w = 0 in Eq. 1), compared with the observed "reference" profile. This purely radiative solution is warmer than observed at all levels, pointing to the presence of adiabatic cooling. Adding a vertical velocity profile roughly constant in pressure coordinates below the ~0.03-mbar level allows us to reproduce fairly well the observed profile below 0.1 mbar. The corresponding upward velocity at 1 mbar is ~0.3 mm s^{-1}.

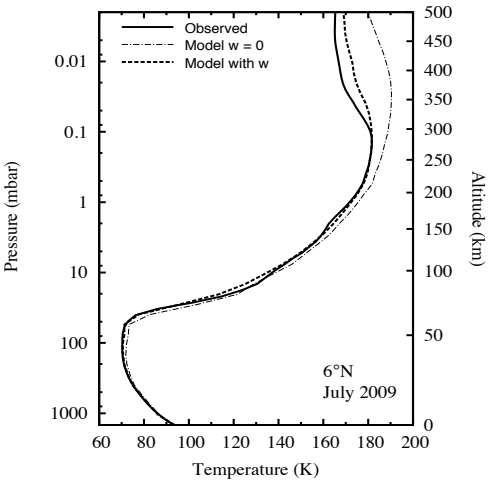

Figure 1: A temperature profile retrieved from Cassini/CIRS measurements near 6°N complemented by Huygens/HASI data (solid line) is compared with our model predictions with no adiabatic cooling (dash-dotted line) and with adiabatic cooling (dashed line).

This adiabatic cooling at low latitudes is associated with the general circulation that allows redistribution of heat to higher latitudes.

Running our model at 0°, 30°N and 30°S with this vertical velocity profile, constant with time, produces seasonal variations of temperatures much larger than observed between 0.2 and 4 mbar. At the equator, the predicted drop in temperature at 1 mbar, 7 K between 2007 and 2016, is due to the eccentricity of the orbit. The model outputs can be brought in agreement with the 4-K observed decrease, by adding a season-modulated term in the vertical velocity profile, such as a sinusoidal function of solar longitude with an amplitude of 1/3 of the constant term [2].

Similarly, at 30°N and 30°S, a good agreement with the observed time variation of temperatures since 2004, can be obtained by adding a sinusoidal modulation of the vertical velocity profile. Their amplitudes are larger than that at the equator, implying subsidence in winter and uplift in summer [2].

In the future, the model will be extended to high latitudes and will include the observed variations of gases and aerosols, to investigate the complex changes in the temperature field around equinox.

References

[1] Achterberg, R. K., Gierasch, P. J., Conrath, B. J., Flasar, F. M., and Nixon, C. A.: Temporal variations of Titan's middle-atmospheric temperatures from 2004 to 2009 observed by Cassini/CIRS, Icarus, Vol. 211, pp. 686-698, 2011.

[2] Bézard, B., Vinatier, S., and Achterberg, R. K.: Seasonal radiative modeling of Titan's stratosphere, American Astronomical Society, DPS meeting #48, id.509.06, 2016.

[3] Doose, L. R., Karkoschka, E., Tomasko, M. G., and Anderson, C. M.: Vertical structure and optical properties of Titan's aerosols from radiance measurements made inside and outside the atmosphere, Icarus, Vol. 270, pp. 355-375, 2016.

[4] Fulchignoni, M., et al.: In situ measurements of the physical characteristics of Titan's environment, Nature, Vol. 438, pp. 785-791, 2005.

[5] Niemann, H. B., et al.: Composition of Titan's lower atmosphere and simple surface volatiles as measured by the Cassini-Huygens probe gas chromatograph mass spectrometer experiment, J. Geophys. Res., Vol. 115, E12006, 2010.

[6] Vinatier, S., et al.: Seasonal variations in Titan's middle atmosphere during the northern spring derived from Cassini/CIRS observations, Icarus, Vol. 250, pp. 95-115, 2015.

EPSC Abstracts
Vol. 11, EPSC2017-765, 2017
European Planetary Science Congress 2017

Tidal dissipation in the ice-ocean system on Enceladus

H. Hellard (1,2), **F. Sohl** (1), W. Van der Wal (2), T. Steinke (2), and H. Hussmann (1)
(1) DLR, Berlin, Germany, (2) Delft University of Technology, Delft, The Netherlands (frank.sohl@dlr.de / Fax: +49-30-67055-303)

Abstract

We investigate how the interior structure and dissipation of tidal energy on Enceladus affect the lateral layering of its outer ice shell. Structural models are created that satisfy the satellite's mean density and polar moment-of-inertia factor as derived from Cassini gravity field data. We particularly consider variations in core density, ice shell thickness and ocean composition. A partly dehydrated core is found to be consistent with current ice shell thickness estimates and power output measurements for Enceladus.

1. Introduction

The Saturnian moon Enceladus is one of the most geologically active bodies in the solar system [1]. Ridged terrains dominated by intense tectonism are observed on both hemispheres while plume jets emanating from geological surface cracks are confined to the South Polar Terrain, thereby suggesting lateral heterogeneity of the satellite's internal structure [2]. The rotational state of Enceladus indicates that a global subsurface ocean mechanically decouples the outer ice shell from the satellite's deep interior [3]. While the latter is not directly accessible, thermodynamic modelling provides important insights and constraints on its composition and physical properties. This study aims at investigating the constraints imposed by the temperature distribution within the ice-ocean system on the rheological structure of the outer ice shell and its lateral variations, as well as on the density of the core.

2. Model

We subdivide Enceladus' interior into four chemically homogeneous layers and construct spherically symmetric structural models that are compliant with the satellite's mean density and polar moment-of-inertia factor derived from Cassini gravity field data [4]. The structural models consist of a core, a salty liquid water layer, a lower warm ductile ice layer and an upper cold brittle ice layer. The brittle-ductile boundary is related to a change in viscosity associated with a critical transition temperature. We first calculate the degree-2 body tide Love numbers for our structural models and obtain diurnal tidal stresses at the satellite's surface from combinations of those numbers [5]. We consider eccentricity tides and assume that the dissipation of tidal energy is restricted to the ductile sublayer of the outer ice shell. Since the total ice shell thickness is small compared to the satellite's mean radius (less than 10%), we apply a thin shell approximation to compute localized tide-induced dissipation and surface heat flow patterns [6].

3. Results and Discussion

The calculated interior structure model of Enceladus shown in Fig. 1 satisfies the mean density and moment-of-inertia factor. A model with a rocky core with radius of 152 km and an average density of 3000 kg m^{-3} satisfies observed total heat flux constraints. This core density suggests partial hydration of the core, which is consistent with the presence of substantial amounts of hydrogen in Enceladus' plumes as recently detected by the Cassini spacecraft [7]. The core is overlain by a substantial subsurface water ocean and a floating ice shell up to a few tens of kilometers thick. The change in viscosity at the brittle-ductile boundary reaches roughly 10^7 Pa s, and corresponds to a critical brittle-to-ductile transition temperature of about 84 K for a predominant ice creep mechanism involving grain boundary sliding [8]. The dissipation of tidal energy induced by eccentricity tides results in a polar surface heat flow roughly five times higher than the equatorial one. This may have an effect particularly on the polar surface temperature that is governed by the mean daily insolation. By computing radial temperature profiles, we emphasize that the temperature barely increases within the brittle ice layer in the absence of internal heating. On the other hand, large temperature increase takes place within

the ductile ice layer in response to tidal energy dissipation.

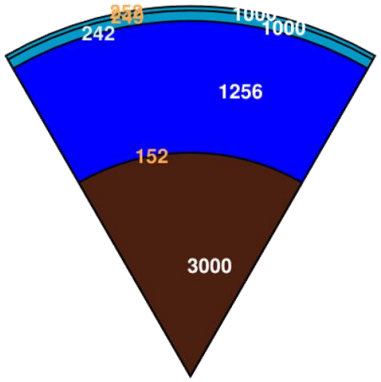

Figure 1: Interior structure model of Enceladus. Radial distance is given in units of kilometers; density is indicated in units of kg m^{-3} [8].

Fig. 2 presents the heterogeneous lateral temperature distribution at the brittle-ductile boundary. The highest temperatures are derived at the poles, while lowest values are calculated for sub-Saturnian longitudes, extending from the equator to mid-latitudes. This results in lateral depth variations of the brittle-ductile rheological boundary, which can be derived by extracting the critical brittle-to-ductile transition temperature from the computed three-dimensional temperature distribution.

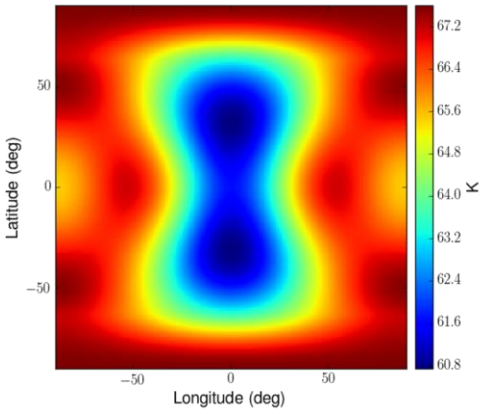

Figure 2: Heterogeneous temperature distribution at the brittle-ductile transition of the outer ice shell [8].

We show that the brittle layer becomes thicker at sub-Saturnian longitudes from the equator to mid-latitudes, and thinner towards the poles at all longitudes [8]. These results are consistent with the observed plume jets around the South Pole, since a thin brittle layer allows easy transport of material towards the surface. The global tidal dissipation that can be achieved within the ductile ice layer may even supersede the upper limit of the global output measurements [9]. Our structural model corresponding to a partly dehydrated core thus complies with current ice shell thickness estimations and tidal power output measurements.

4. Summary and Conclusions

Structural and tidal models of Enceladus are calculated. We propose a method to derive lateral variations of the rheological boundary between the brittle and ductile ice layers. This allows the construction of a consistent three-dimensional thermodynamic model of the ice-ocean system, accounting for the dissipation of tidal energy as induced by diurnal tides. The total ice shell thickness is found to decrease with higher core density in order to keep the ocean density within a realistic range for saltwater below 1250 kg m^{-3}. A partly hydrated core is compliant with current ice shell thickness estimates, dissipation of tidal energy, and hydrogen abundances in the plumes. A possible hydration of the core implies hydrothermal exchange processes between the latter and the ocean, which may result in density and composition variations of the salty water. This result is critical for the habitable potential of Enceladus.

References

[1] Spencer, J. and Nimmo, F.: Enceladus: an active ice world in the Saturn system, Ann. Rev. Earth Planet. Sci. 41, 693-717, 2013. [2] Hsu, H.-W. et al.: Ongoing hydrothermal activities within Enceladus, Nature 519, 207-220, 2015. [3] Thomas, P. et al.: Enceladus's measured physical libration requires a global subsurface ocean, Icarus 264, 37-47, 2015. [4] Iess, L., et al.: The gravity field and interior structure of Enceladus, Science 334, 78-80, 2014. [5] Wahr, J. et al.: Modeling stresses on satellites due to nonsynchronous rotation and orbital eccentricity using gravitational theory, Icarus 200, 188-206, 2009. [6] Beuthe, M.: Tides on Europa: the membrane paradigm, Icarus 248, 109-134, 2014. [7] Waite, J.H. et al.: Cassini finds molecular hydrogen in the Enceladus plume: Evidence for hydrothermal processes, Science 356, 155-157, 2017. [8] Hellard, H.: Geodynamic modeling of the ice-ocean system on Enceladus, Master thesis, Delft University of Technology, 2017. [9] Kamata, S. and Nimmo, F.: Interior thermal state of Enceladus inferred from viscoelastic state of the ice shell, Icarus 284, 387-393, 2017.

EPSC Abstracts
Vol. 11, EPSC2017-818, 2017
European Planetary Science Congress 2017

Resolving the Mass Production and Surface Structure of the Enceladus Dust Plume

S. Kempf (1), B. Southworth (1), J. Schmidt (3), F. Postberg (4), and R. Srama (4)
(1) LASP, University of Colorado at Boulder, Boulder, United States (sascha.kempf@lasp.colorado.edu), (2) University of Oulu, Finland, (3) University of Heidelberg, Germany, (4) University of Stuttgart, Germany

Abstract

There are ongoing arguments with regards to the Enceldaus plume, both on the total mass of ice particles produced by the plume in kg/s, as well as the structure of plume ejection along the tiger stripes. Herein, results from Cassini?s Cosmic Dust Analyzer (CDA) and Imaging Science Subsystem (ISS) are used in conjunction with large-scale plume simulations to resolve each of these issues. Additional results are provided on the short-term variability of the plume, and the relation of specific surface deposition features to emissions along given areas of the tiger stripes.

By adjusting their plume model to the dust flux measured by the Cassini dust detector during the close Enceladus flyby in 2005, Schmidt et al. (2008) obtained a total dust production rate in the plumes of about ∼5 kg/s. On the other hand, Ingersoll and Ewald (2011) derived a dust production rate of 51 kg/s from the total plume brightness. More recently, plasma models and data from the Cassini Plasma Spectrometer suggest a more modest 12 kg/s; however, this result is based solely on nanograins, which make up a small percentage of plume mass. Knowledge of the production rate is essential for estimating the dust to gas mass ratio, which in turn is an important constraint for finding the plume source mechanism.

Here we report on measurements of the plume dust density during the last close Cassini flyby at Enceladus in October 2015. The data match our numerical model for the Enceladus plume. The model is based on a large number of dynamical simulations including gravity and Lorentz force to investigate the earliest phase of the ring particle life span. The evolution of the electrostatic charge carried by the initially uncharged grains is treated self-consistently. Our numerical simulations reproduce all Enceladus data sets obtained by Cassini's Cosmic Dust Analyzer (CDA). Our model calculations together with the new density data constrain the Enceladus dust source rate to < 5 kg/s. Based on our simulation results we are able to draw conclusions about the emission of plume particles along the fractures in the south polar terrain.

In 2014, Porco et al. produced a set of ~ 100 jet locations for the Enceladus plume based on the triangulation of several years worth of images. Spitale et al. (2015) instead suggested a continuous emission along the tiger stripes, demonstrating that some of the jets published in Porco et al. could in fact result from viewing multiple continuous emissions in an overlapping manner. Simulations run herein demonstrate that it is likely both emissions exist and are active, with surface deposition dominated by the continuous, "curtain" emissions, while temporally variable jetting activity likely contributes primarily to the E-ring. Surface deposition patterns from a curtain-style emission are shown to agree well with recent, global color maps of Enceladus, further confirming the accuracy of the underlying model. Surface deposition structure is shown to be robust under changes in model parameters, and certain prominent areas seen in color maps are associated with emission areas of the plume.

EPSC Abstracts
Vol. 11, EPSC2017-826, 2017
European Planetary Science Congress 2017

Titan's Stratospheric Water Vapor profile from Cassini CIRS far-infrared Spectra

V. Cottini[1,2], C.A. Nixon[2], R.K. Achterberg[1,2], N. Gorius[3,2], A. Coustenis[4], P.G.J. Irwin[5], C.M. Anderson[2],, G.L. Bjoraker[2], D.E. Jennings[2], F. M., Flasar[2], T. M., Ansty[6]

(1) University of Maryland, College Park, USA (valeria.cottini@nasa.gov Fax: +1-301-286-1683), (2) NASA Goddard Space Flight Center, Greenbelt, USA, (3) Catholic University of America, USA, (4) Laboratoire d'Etudes Spatiales et d'Instrumentation en Astrophysique (LESIA), Observatoire de Paris, CNRS, UPMC Univ. Paris 06, Univ. Paris-Diderot, 5, place Jules Janssen, F-92195 Meudon Cedex, France (5) Atmospheric, Oceanic and Planetary Physics, University of Oxford, Parks Rd., Oxford OX1 3PU, UK (6) Department of Space Science, Cornell University, Ithaca, NY 14853, USA

Abstract

In this work we present an update of water vapor abundance in Titan's stratosphere through modeling of its emission lines present in the spectral range (100 – 300 cm^{-1}) observed by the Cassini Composite Infrared Spectrometer (CIRS) far-IR Focal Plane 1 (FP1) detector. We model and analyze high spectral resolution (0.5 cm^{-1}) disk and limb observations acquired from December 2004 to December 2016 to determine the water mixing ratio profile. Nadir data and limb data acquired up to 2011 and pointing at two altitudes in Titan's stratosphere (125 and 225 km) have been previously used in [1] to detect water vapor and retrieve its abundance at two limb altitudes. Few years of more data and improved calibrations are now available to further investigate water vapor. In particular, three far-infrared limb integrations were planned and acquired in 2014 and 2016 with CIRS staring at a single altitude (175 km) for longer time. These new data provided us with one more altitude point to derive the water vapor abundance and improve its retrieved vertical profile, increasing significantly the science results. These results will also be compared to previous results and to the latest photochemical models of Titan's oxygen species.

1. Introduction

Oxygen compounds observed in Titan's atmosphere are CO, CO_2 and H_2O, with a volume mixing ratio of ~50 ppm, ~15 ppb and ~1 ppb, respectively. The abundances of these species are determined by the physical and chemical processes occurring in Titan's atmosphere. These processes place fundamental constraints on the origin and evolution of Titan's atmosphere, thus bringing oxygen chemistry and its impact on the chemical composition at the center of a long-standing debate. Determine the abundance distribution and profile of these molecules is therefore a very important step for understanding Titan's history. Information on water vapor profile is needed in photochemical models to constraint the origin on water and the other oxygen compounds on Titan. Water vapor on Titan was first detected using whole-disk observations from the Infrared Space Observatory ([2]). An early attempt to measure H_2O with Cassini CIRS was unsuccessful due to poor signal-to-noise (S/N) ratios in early versions of the calibration pipeline spectra and a limited number of available spectra. Therefore, only an upper limit could be retrieved ([3]). Since then, water emission in the CIRS data has been only qualitatively observed ([4]). The Cassini Ion and Neutral Mass Spectrometer (INMS) detected H_2O in the upper atmosphere ([5]). After that water stratospheric profile was finally inferred by CIRS [1] and HERSHEL [6]. New CIRS data analyzed in this work provided us with one more altitude point to derive water vapor abundance and improve its retrieved vertical profile and few more years of observations allow us better signal to noise averages and also variations of water with time.

2. Data and Method

CIRS has obtained spectra of Titan during most of the 127 flybys that have taken place since Saturn Orbit Insertion in 2004. Water vapor abundance in Titan's stratosphere is retrieved through modeling of its emission lines observed by CIRS far-IR Focal Plane 1 detector. About 30 lines are present in the spectral range 100 – 300 cm^{-1}. Averages of multiple spectra are necessary to improve the signal to noise and observe water. We retrieve the water abundance from zonal averages of high spectral resolution (0.5 cm^{-1}) far infrared on-disk observations (FIRNADCMP) of equatorial latitudes (Fig. 1). We

also retrieve the water stratospheric profile analyzing limb far infrared integrations (FIRLMBINT), which are CIRS observations acquired from 75 to 135 minutes from closest approach (25,000 to 45,000 km range) and pointing at two altitudes in Titan's stratosphere (125 and 225 km) for about 30 min for each altitude. In order to obtain an average of homogenous data we include observations of Titan's with stratospheric temperatures at 1 mbar between 165 and 170 K. We also planned a new observational type design, essentially a FIRLMBINT (same distance/time from closest approach), but staring at a single altitude only (175 km) for 1 hr. This new observational mode (FIRLMBWTR) was designed to add a third data point to the water vertical profile and was performed three times, in April 2014 and May and November 2016. The average of these observations at an intermediate altitude, although more noisy than at other levels, allowed us to retrieve water at one more point. Stratospheric temperatures in the 0.5 - 4.0 mbar range were obtained by inverting spectra of CH_4 in the ν_4 band centered at 1304 cm^{-1} and measured by CIRS in the focal plane 4 (FP4) detector.

3. Figures

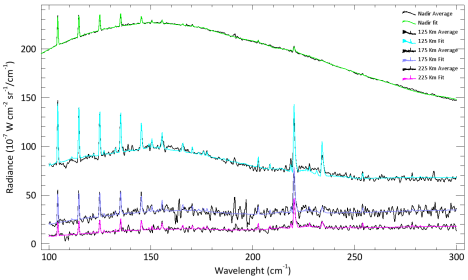

Figure 1: CIRS far-IR observations used to retrieve water from four different averages. From the top are plotted: on-disk observations (21100 spectra acquired from December 2004 to December 2016 in the latitudinal range of 30°S –30°N), limb observations centered around 5590, 175 and 225 km (respectively 693, 175, 687 and 280 spectra acquired from December 2004 to December 2016 for regions with atmospheric temperature at 1 mbar >165K) and their fit (in green, blue, purple and cyan respectively) assuming a constant water mole fraction above the condensation altitude.

4. Summary and Conclusions

Nadir and limb spectra at 125 and 225 km have been used in the past to retrieve water vapor [1]. More data are now available to retrieve the water vapor stratospheric profile. Three far infrared integrations have been replaced in 2014 and 2016 with observations at 175 km only. These new data provided us with one more altitude point to derive water vapor abundance and improve its retrieved vertical profile, increasing the information provided to photochemical models to derive Titan's atmospheric processes. The 175 km observations provide ~175 spectra and despite the average being lower signal-to-noise than at other altitudes, making water retrieval more challenging, the water abundance was retrieved with significance > 3-σ. The retrieved water abundances are consistent within errors to results in [1]. The results are compared to previous work and to the latest photochemical models of Titan's oxygen species.

References

[1] Cottini V., Nixon, C. A., Jennings, D. E., Anderson, C. M., Gorius, N., Bjoraker, G. L., Coustenis A., Teanby, N. A., Achterberg, R. K., Bézard, B., de Kok, R., Lellouch, E., Irwin, P. G. J., Flasar, F. M., Bampasidis, G.: Water vapor in Titan's stratosphere from Cassini CIRS far-infrared spectra. Icarus, Volume 220, Issue 2, Pages 855–862, 2012.

[2] Coustenis, A. *et al.*: Evidence for water vapor in Titan's atmosphere from ISO/SWS data. Astron. Astrophys. 336, L85–L89, 1998.

[3] de Kok, R. *et al.*: Oxygen compounds in Titan's stratosphere as observed by Cassini CIRS. Icarus 186, 354–363, 2007.

[4] Bjoraker, G., *et al.*: American Astronomical Society. DPS Meeting #40, #31.12, Bulletin of the AAS, 40, 448, 2008.

[5] Cui, J., *et al.*: Analysis of Titan's neutral upper atmosphere from Cassini ion neutral mass spectrometer measurements. Icarus 200, 581–615, 2009.

[6] Moreno, R.; Lellouch, E.; Lara, L. M.; Feuchtgruber, H.: The abundance, vertical distribution and origin of H_2O in Titan's atmosphere: Herschel observations and photochemical modeling. Icarus, Volume 221, Issue 2, p. 753-767, 2012.

EPSC Abstracts
Vol. 11, EPSC2017-890, 2017
European Planetary Science Congress 2017

Characterization of the vertical profile of C_2N_2 profile in Titan's atmosphere

M. Sylvestre, and N. A. Teanby
School of Earth Sciences, University of Bristol, Wills Memorial Building, Queen's Road, Bristol BS8 1 RJ, UK (melody.sylvestre@bristol.ac.uk)

Abstract

Titan's atmosphere hosts a large variety of trace species. Some of them, such as hydrocarbons and nitriles ($C_xH_yN_z$) are produced by a complex photochemistry, initiated by the dissociation of N_2 and CH_4 by solar UV and EUV photons, high energy electrons from Saturn's magnetosphere, and cosmic rays (Wilson & Atreya 2004; Vuitton et al. 2012). The meridional and vertical distributions of each photochemical product are shaped in a specific way by atmospheric dynamics and chemistry, depending on its production and loss chemical reactions, and on its photochemical lifetime. Thus, these species can be used as tracers of the chemical and dynamical processes in Titan's atmosphere.

In this study, we present the first measurements of the vertical profile of C_2N_2 (cyanogen). We analyse Cassini/CIRS (Flasar et al. 2004) limb spectra in the far-infrared to probe the volume mixing ratio of C_2N_2, using its ν_5 band at 234 cm^{-1}. These observations allow us to measure C_2N_2 in the the stratosphere, between 5 and 0.5 mbar. C_2N_2 profiles are obtained using the constrained non-linear inversion code NEMESIS (Irwin et al. 2008).

In this work, we focus on two regions undergoing very different atmospheric conditions. First, we retrieve C_2N_2 profiles in the equatorial latitudes (25°N - 25°S) between 2006 and 2014, where insolation and stratospheric temperature vary weakly during a Titan's year (Vinatier et al. 2015; Bampasidis et al. 2012). Then, we measure C_2N_2 profiles at high southern latitudes during autumn (after 2009), where strong dynamical effects have been inferred from previous Cassini/CIRS measurements (Coustenis et al. 2016; Vinatier et al. 2015; Teanby et al. 2012), and where the chemistry is different compared to other latitudes, due to the lack of insolation. These results are compared to photochemical models such as Dobrijevic et al. (2016); Krasnopolsky (2014) in order to bring constraints on the chemistry of C_2N_2. Vertical profiles of many other photochemical species have been measured at these latitudes and at similar pressure levels during the Cassini mission (e.g Vinatier et al. (2015)). We compare the C_2N_2 profiles to the profiles of other nitriles such as HCN, and photochemical species with longer and shorter chemical lifetime like H_3CN (2.5×10^7 s for H_3CN and 8.0×10^6 s for C_2N_2 at 300 km according to Wilson & Atreya (2004)) and C_4H_2 (1.4×10^6 s, Wilson & Atreya (2004)), in order to better understand chemical and dynamical processes at play in Titan's stratosphere.

References

Bampasidis, G., Coustenis, A., Achterberg, R. K., et al. 2012, ApJ, 760, 144

Coustenis, A., Jennings, D. E., Achterberg, R. K., et al. 2016, Icarus, 270, 409

Dobrijevic, M., Loison, J. C., Hickson, K. M., & Gronoff, G. 2016, Icarus, 268, 313

Flasar, F. M., Kunde, V. G., Abbas, M. M., et al. 2004, Space Sci. Rev., 115, 169

Irwin, P. G. J., Teanby, N. A., de Kok, R., et al. 2008, J. Quant. Spec. Radiat. Transf., 109, 1136

Krasnopolsky, V. A. 2014, Icarus, 236, 83

Teanby, N. A., Irwin, P. G. J., Nixon, C. A., et al. 2012, Nature, 491, 732

Vinatier, S., Bézard, B., Lebonnois, S., et al. 2015, Icarus, 250, 95

Vuitton, V., Dutuit, O., Smith, M. A., & Balucani, N. 2012, in Titan: Interior, Surface, Atmosphere, and Space Environment, ed. I. Müller-Wodarg, C. A.

Griffith, E. Lellouch, & T. E. Cravens (Cambridge: Cambridge University Press), 224–284

Wilson, E. H. & Atreya, S. K. 2004, Journal of Geophysical Research (Planets), 109, E06002

EPSC Abstracts
Vol. 11, EPSC2017-921, 2017
European Planetary Science Congress 2017

Modeling of methane absorption in Titan's atmosphere using ab initio TheoReTS database spectra predictions

B. Bézard (1), P. Rannou (2), A. Coustenis (1), M. Rey (2), A. Nikitin (3), and V. Tyuterev (2)
(1) LESIA, Observatoire de Paris, CNRS, UPMC, Univ. Paris Diderot, F-92195 Meudon, France, (2) GSMA, UMR 7331 CNRS-Université de Reims Champagne-Ardenne, Reims, France, (3) QUAMER laboratory, Tomask State University, 36 Lenin Avenue, 634050 Tomsk, Russia. (bruno.bezard@obspm.fr)

Abstract

Knowledge of intensities of spectral transitions in various temperature is essential for the modeling of optical properties of planetary atmospheres and for other astrophysical applications. The temperature dependence of spectral features is crucial, but quantified experimental laboratory information in a wide spectral range is often missing. A significant progress has been recently achieved in first principles quantum mechanical predictions (ab initio electronic structure + variational nuclear motion calculations) of rotationally resolved spectra for hydrocarbon molecules. In this work, we use "TheoReTS" information system (http://theorets.univ-reims.fr, http://theorets.tsu.ru) for ab initio spectra predictions of methane isotopologues in a large infrared range at low-T conditions for the modeling of the transmittance in the atmosphere of Titan explored by the Cassini-Huygens space mission. A very good agreement over the whole infrared range from 6000 to 11000 cm^{-1} compared with observations obtained by the Descent Imager / Spectral Radiometer (DISR) on the Huygens probe at various altitudes will be reported.

1. Introduction

With the advent of the highly-successful Cassini-Huygens mission, in the Saturnian system since July 2004, a large amount of Titan data has been acquired. However, in the absence of reliable absorption coefficients of methane for Titan conditions in the near infrared (especially between 0.8 and 1.25 microns), the scientific community is faced with the difficulty of analysing the high-quality spectra and images that have been collected at these wavelengths. After the landing of the Huygens probe on Titan (14 Jan. 2005), the Cassini spacecraft has been pursuing its trek in the Saturnian system and it will continue to do so at least until 2017, continuously providing new discoveries while, at the same time, raising new questions. But even though the Cassini-Huygens mission has been operating for more than 12 years now, Titan is far from having revealed all its secrets. Among other, we still lack a precise description of the lower atmosphere and surface of the satellite. That is where the methane coefficients play a very important role: the modeling of the troposphere and surface requires a precise understanding of the methane influence, CH_4 being the main atmospheric absorbing constituent in the near-infrared.

2. Present status

In the past years many studies have been carried out to tackle this problem using several experimental data or extrapolations. The opacity from methane and from its isotopologues has thus been retrieved in some near-IR regions from laboratory measurements [1], and from empirical line lists available in spectroscopic databases like HITRAN and GEISA. Simulations based on these parameters have produced fits to Titan data from the ground and from space, allowing the extraction of important new information on Titan's atmosphere and surface [2-4]. However, laboratory measurements of low-T methane spectra were missing for wavenumber ranges above 8000 cm^{-1}. Recently very accurate ab initio predictions of methane line parameters in a large frequency and temperature ranges became accessible via "TheoReTS" information system (http://theorets.univ-reims.fr; http://theorets.tsu.ru): Rey et al [5].

3. Results and Conclusions

We have compared atmospheric transmittance ratios at different altitudes of Titan's stratosphere as derived from Huygens/DISR measurements with radiative transfer calculations using TheoReTS. Transmittance spectra were calculated using a line-by-line radiative transfer program with a step of

about half the CH_4 Doppler width and then convolved with a Gaussian function having a FWHM corresponding to the DISR/ULIS resolution. The transmittance to the Sun was calculated as a function of altitude, using the corresponding solar zenith angle and the atmospheric model is the same as in [6]. Molecular gases and isotopologues included are $^{12}CH_4$, $^{13}CH_4$, $^{12}CH_3D$ from the TheoReTS methane database. The methane abundance profile is that derived from Huygens /GCMS measurements by [7]. Preliminary results suggest that this profile yields a somewhat too large absorption above 80 km (Fig. 1).

In the 1.4-micron band, we also intercompared calculations using TheoReTS with two Campargue et al.'s linelists that differ on energy levels of lines observed in the laboratory [1, 8]. Our calculations are in excellent agreement with those based on the linelist in [8].

Overall, the TheoReTS database allows us to reproduce very well Titan's methane transmittance at the surface as derived from ULIS data after landing, with a methane column density from the probe to the Sun as high as 3.5 km-amagat. The agreement is excellent after scaling of the transmittance derived from Tomasko et al.'s (2008) absorption coefficients by a constant factor of 0.85 [rather than the previously suggested factor of 0.92]. We conclude that the TheoReTS database appears suitable to undertake a full retrieval of the methane vertical profile in Titan's atmosphere from the DISR data set, at least beyond 930 nm, with a proper estimate of the associated error bars.

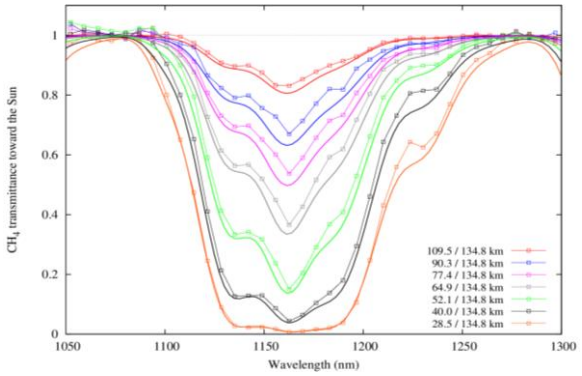

Figure 1. Ratios of DISR/ULIS methane transmittance spectra at different altitudes (squares) compared with calculations for a stratospheric CH_4 mole fraction of 1.48 % and TheoReTS line lists [5]. Observed and synthetic spectra are both ratioed to a reference spectrum at z_1=134.8 km.

Acknowledgements

The support from "Programme national de Planétologie" (PNP), France, from LIA SAMIA, from ANR e-PYTHEAS and from Acad. Mendeleev funding Program of TSU, Russia, is acknowledged.

References

[1] A.Campargue et al.: Icarus, Vol. 219, 110, 2012
[2] C. De Bergh et al.: PSS , Vol. 61, 85, 2012
[3] M. Hirtzig et al.: Icarus Vol. 226, 470 ,2013
[4] A. Solomonidou et al.: Icarus, Vol. 270, 85, 2016
[5] M. Rey et al.: J. Mol.. Spectrosc., Vol. 327, 138, 2016
[6] B. Bézard: Icarus, Vol. 242, 64, 2014
[7] H. Niemann et al.: J. Geophys. Res., Vol. 115, E12006, 2010
[8] A. Campargue et al.: J. Mol. Spectrosc., Vol. 291, 16, 2013

EPSC Abstracts
Vol. 11, EPSC2017-923, 2017
European Planetary Science Congress 2017

Thermal Structure of Pluto's Lower Atmosphere

R. V. Yelle (1), T. Koskinen (1) and P. Lavvas (2)
(1) Department of Planetary Sciences, University of Arizona, Tucson, Arizona (2) University of Reims, Champagen-Arden, Reims, France (rogeryelle@gmail.com)

Abstract

Prior to the New Horizons (NH) encounter with Pluto it was expected that the atmosphere was composed primarily of N2 with a significant abundance of CH4, that the atmospheric temperature rose rapidly from a surface temperature of ~36 K to ~105 K near ~0.1 Pa and that this high temperature powered an escape rate of 10^{27} s^{-1}. The composition and rapid temperature rise were confirmed but it was also discovered, through NH and Alma observations, that the atmospheric temperature dropped from its maximum of 105 K to a 70-80 K in the upper atmosphere and that, as a consequence, the atmospheric escape rate was orders of magnitude smaller than predicted. We investigate this problem by constructing non-LTE radiative-conduction models for the thermal structure of Pluto's atmosphere based on the observed CH4 abundance as well as species produced by photolysis of CH4 and N2, including C2H2, C2H4, C2H6, and HCN. We find that that temperature drop from 105 K to 70-80 K can be explained by radiative cooling by C2H2, C2H6, and HCN. Cooling by undetected species, such as H2O, is not required. We will also discuss the uncertainties in calculations of the radiative cooling rate and the implications for the escape rate at other phases of Pluto's eccentric orbit.

EPSC Abstracts
Vol. 11, EPSC2017-950, 2017
European Planetary Science Congress 2017

Titan's Icy Scar

C.A. Griffith (1), P. F. Penteado (2), J.D.Turner (3), C.D. Neish (4), G. Mitri (5), M. J. Montiel (1), A. Schoenfeld(6), R.M.C. Lopes (2)
(1) Department of Planetary Sciences, LPL, University of Arizona, Tucson, AZ, 85721; grifith@lpl.arizona.edu (2) JPL, California Institute of Technology, Pasadena, CA 91109, USA (3) Department of Astronomy, University of Virginia, Charlottesville, VA 22904, USA (4) Dept. Physics & Space Sciences, Florida Inst. of Tech., Melbourne, Florida, USA (5) Universite de Nantes, Nantes, 44322 NANTES Cedex 3 - FRANCE (6) Department of Earth & Planetary Sciences, UCLA, Los Angeles, CA, 90095

Abstract

Here we conduct a Principal Components Analysis (PCA) of Cassini/VIMS [1] infrared spectral windows to identify and quantify weak surface features, with no assumptions on the haze and surface characteristics. This study maps the organic sediments, supplied by past atmospheres, as well as ice-rich regions that constitute Titan's bedrock.

1. Introduction

Titan's surface is composed of two compositionally distinct components, the icy bedrock and the atmosphere-derived organic sediments, which can be studied in the 8 wavelengths (0.93, 1.1, 1.3, 1.6, 2.0, 2.7, 2.8, and 5.0 μm) between optically thick CH_4 and CO bands in Titan's atmosphere. Within these "windows" candidate surface components exhibit different absorption features; e.g., NH_3 ice and C_2H_6 liquid absorb at 2.0 μm, while the complex organic material may absorb at 0.93 and 1.08 μm, e.g., However, water ice is the most straightforward constituent to identify, because 3 of its strong bands lie within the 1.6, 2.0 and 2.8 μm windows [2].

Recent advances in our understanding of Titan's surface composition at near-IR wavelengths stem from the analyses of Cassini's Visual and Infrared Mapping Spectrometer (VIMS). Detailed radiative transfer (RT) studies of Titan's surface that treat the effects of overlying atmosphere [3-9] target local regions of interest. Global studies of Titan's surface have either not treated the effects of the haze or used heuristic approaches to constrain the haze. While prior studies identified some major compositional tendencies, and revealed the compositional information of morphologically unique terrain, the question arises as to how to treat the effects of Titan's variable haze, how to extract weakest spectral features, and how to determine the spectral information content of the VIMS data.

1.1. The PCA analysis

Here we present an investigation of Titan's surface spectra order to determine the composition of Titan's surface on a global scale and to identify and map the surfaces where water ice "bedrock" is exposed, despite the ongoing sedimentation of organic material from the atmosphere. This work is accomplished by a Principal Components Analysis (PCA) of the 4 wavelengths that most clearly view Titan's surface (1.1, 1.3, 1.6, and 2.0 μm). In contrast to previous analyses, this study identifies and deconstructs the major spectral components of the surface on a global scale, without prior assumptions regarding the surface composition and atmospheric scattering and absorption, as assumed from radiative transfer analyses. In addition, this approach by virtue of sampling the correlations among the 4096 spectra that make up a cube can identify subtle spectral features that would not be apparent in a single spectrum.

The PCA analysis is conducted on over 130,000 spectra contained in 37 VIMS data cubes to determine the spectral trends that define the greatest spectral variance (the principal component) as well as successively lesser orthogonal correlations between the I/F values at each wavelength. Each VIMS cube, which contains M$\sim$4096 spectra, is analyzed separately to account for the different viewing conditions and signal-to-noise ratio. The orthogonal spectral trends are derived by calculating the eigenvalues and eigenvectors of the covariance matrix, defined by the I/F values at the 4 window wavelengths of each cube and their deviations from their mean values.. The eigenvector associated with the highest eigenvalue defines the principal component, with successively smaller eigenval-

ues defining lesser correlations between the variables. Spectroscopically distinct terrains are identified by determining which spectra fit the principal component to within 1-σ, and which of the remaining spectra require the $2^{\rm nd}$, and then $3^{\rm rd}$ components to fit the data to within 1-σ.

For all cubes, we find that the principal component consists of the average spectral features modulated by the surface brightness, the main source of variance. This component contains 87%–99% of the variance, depending on the cube. It captures the effects of Titan's atmosphere, principally CH_4 absorption and haze scattering, which establishes the average spectrum. The primary component also carries the average surface spectrum, which based on Titan's dielectric constant measured by Cassini/Radar [10] and prior near-IR studies, e.g. [11-14] is dominated by organic sediments. In contrast, absorption features at 1.6 and 2.0 μm, characteristic of water ice, dominate the $2^{\rm nd}$ component and explain 0.4%–13%. Ice features observed at zenith viewing indicate have the 2.8 μm water absorption. Thus the main spectral signatures of Titan's tropical surface are established by the presence or lack of water features.

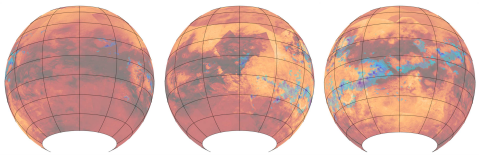

Figure 1: Titan's ice-rich terrain wraps around 40% of Titan's surface as a great circle.

The spectral trends of ice-rich and ice-poor terrains determined from the PCA analysis agree with microwave emissivity measurements [10]. The PCA-derived terrains agree in detail with prior RT analyses of local regions, e.g. [5,9,15]. The PCA analysis is consistent with much of the the composite maps. The detailed match of the RT and PCA techniques both justify RT analyses despite the required assumptions, and substantiate this PCA study of the surface composition on a large scale.

2. Summary and Conclusions

We find that the predominant spectral features of Titan's surface match 3 water ice bands of half of Titan's surface. The indicated strongest water ice absorptions concentrate in a linear feature, which extends, in a great circle, across 40% of Titan's globe. Otherwise ice is exposed only in local regions excavated by craters, particularly Titan's largest crater, Menrva, or exposed by erosion, thereby suggesting that cryovolcanism, if active, is currently not widespread. Titan's linear ice-rich feature appears to follow ridges, and based on its global nature is likely tectonic, although its origin and evolution remain obscure. In contrast, Titan's organic sediments indicate significant spectral diversity, correlated with large scale terrains. Whether this diversity is a result of a vibrant but slow organic chemistry on Titan's surface, or the interaction of sediment with the subsurface methane, or simply physical changes in the sediments, can be explored with a more extensive spectral studies of Titan's surface.

Acknowledgements

This work was funded by the University of Arizona.

References

[1] R. Brown et al. Space Science Reviews, 115, 111, 2004

[2] R. Clark et al JGR (Planets), 115, 10005, 2010

[3] C. Griffith et al. Science, 300, 628, 2003

[4] A. Coustenis et al. Icarus 177, 89, 2005

[5] L. Soderblom et al. Icarus, 208, 905, 2010

[6] C. Griffith et al. Icarus, 218, 975, 2012

[7] S. Le Mouélic et al. Planet. Space Sci, 73, 178, 2012

[8] M. Hirtzig et al. Icarus, 226, 470, 2013

[9] A. Solomonidou et al. JGR (Planets), 119, 1729 2014

[10] Janssen et al. Icarus, 270, 443, 2016

[11] J. Barnes et al. Icarus, 186, 242, 2007

[12] L. Soderblom et al. Planet. Space Sci, 55, 2025, 2007

[13] J. Radebaugh et al. Icarus, 213, 608, 2011

[14] Le Gall et al. Icarus, 213, 608, 2011

[15] Soderblom et al. Icarus, 204, 610, 2009